Analysis and design of higher-symmetric metasurfaces

Mohammad Bagheriasl

SORBONNE UNIVERSITÉ

DOCTORAL THESIS

Analysis and Design of Higher-Symmetric Metasurfaces

Author:
Mohammad
BAGHERIASL

Supervisor:
Dr. Guido VALERIO

A thesis submitted in fulfillment of the requirements for the degree of Doctor of Philosophy

in the

Génie électrique et électronique de Paris
Faculty of Science and Engineering

Jury members:

M. Philippe POULIGUEN, Responsable du domaine scientifique Ondes Acoustiques et Radioélectriques, DGA	Rapporteur
M. Paolo BURGHIGNOLI, Associate Professor, Université Sapienza de Rome	Rapporteur
Mme. Claire MIGILIACCIO, Professeure des Universités, Université Cote d'Azur	Examinateur
M. Julien De ROSNY, Directeur de Recherches, CNRS	Examinateur
M. Marc Hélier, Professeur des Universités , Sorbonne Université	Examinateur
M. Guido VALERIO, Maitre de Conférences (HDR), Sorbonne Université	Directeur de thése
M. Romain CONTRERES, Ingénieur de Recherche, CNES CST	Membre invité
Mme. Erika VANDELLE, Ingénieur de Recherche, Thales R&D	Membre invité
M. Julien SARRAZIN, Maitre de Conférences (HDR), Sorbonne Université	Membre invité

Declaration of Authorship

I, Mohammad BAGHERIASL, declare that this thesis titled, "Analysis and Design of Higher-Symmetric Metasurfaces" and the work presented in it are my own. I confirm that:

- This work was done wholly or mainly while in candidature for a research degree at this University.
- Where any part of this thesis has previously been submitted for a degree or any other qualification at this University or any other institution, this has been clearly stated.
- Where I have consulted the published work of others, this is always clearly attributed.
- Where I have quoted from the work of others, the source is always given. With the exception of such quotations, this thesis is entirely my own work.
- I have acknowledged all main sources of help.
- Where the thesis is based on work done by myself jointly with others, I have made clear exactly what was done by others and what I have contributed myself.

Signed: _____

Date: _____

SORBONNE UNIVERSITÉ

Abstract

Faculty of Science and Engineering

Doctor of Philosophy

Analysis and Design of Higher-Symmetric Metasurfaces

by Mohammad BAGHERIASL

Higher symmetries in periodic structures are internal symmetries in each unit cell that are additional to the periodic symmetry. The use of higher symmetries in the unit cell of periodic structures provides interesting electromagnetic characteristics. The higher symmetries used in a unit cell can be of the two types: glide symmetry or twist symmetry. Glide symmetry is encountered when each cell is invariant after a translation of half a period and a mirror reflection of the structure, and twist symmetry is the invariability of each unit cell after a translation and a rotation (twist) around the translation direction. Recent research on structures with these higher symmetries has shown that the addition of higher symmetries in periodic structures can increase the bandwidth of their stopband. It has also shown that these structures achieve a nearly constant refractive index over an ultra wide band which supports a dispersion-less propagation of the wave. These two characteristics along with the absence of dielectric losses of holey metasurfaces make higher symmetric holey metasurfaces a good candidate for design of reconfigurable waveguide technology. In addition, to utilize higher symmetric structures more efficiently in the design process of the new waveguide technology, a reliable modeling of these structures is of great importance.

Contents

List of Figures

List of Tables

Chapter 1

Introduction

Higher symmetric periodic structures have recently drawn huge attention in the electromagnetics research due to their unique characteristics. Elimination of the stopband between the first and the second Bloch mode, exhibiting a strong and wide stopband region between the second and the third Bloch mode and demonstrating a linear dispersion diagram in their first passband are three of the main characteristics of higher symmetric periodic structures. This different electromagnetic behavior between such periodic structures and those with no higher symmetry provides myriads of opportunities in design of electromagnetic components. Higher symmetries can be realized in three dimensional configurations of metallic structures with no dielectric material. The absence of the dielectric losses in these all-metallic structures makes them appropriate for usage in higher frequencies. An all-metallic structure with glide symmetry which is a type of higher symmetry could be realized in two separate parts which could then be positioned with no contact between them. Their respective position can be adjusted accordingly to allow for reconfigurability in the structure. Our goal in this work is to first come up with an analysis method that can obtain the dispersive behavior of periodic structures with higher symmetries very efficiently, one which can provide a framework for understanding the reason behind the different behavior of the structures with and without higher symmetry. Study of higher-symmetric and non-higher-symmetric unit cells using our analysis approach leads to some interesting conclusions on the effect of higher order modes in constituting the different electromagnetic characteristics between the two. As a second goal of this work, we investigate the possibility of reconfigurability of higher symmetric structures to come up with a reconfigurable waveguide technology that leads to design of an on/off waveguide switch.

1.1 Organization of the Document

In Chapter 2 we introduce periodic structures and discuss wave propagation in these structures. We also introduce higher symmetries in periodic structures and discuss previous studies on this topic. We furthermore review their applications and end the chapter with a motivation of our work presented in the following chapters of the thesis.

In Chapter 3, we introduce a multimodal analysis method based on the transmission matrix of periodic unit cells. We then extend this method to

specific formulations for different higher symmetries which reduces the complexity of their analyses and also their computation time. Next, we apply our analysis method to higher symmetric structures to observe the impact of higher order modes on the dispersive properties of these structures.

In Chapter 4, we provide at first an introduction on millimeter-wave switch technologies. We then discuss the design of two reconfigurable waveguides that can act as an on/off waveguide switch giving a step by step design procedure with achieved results and their explanations. We finally discuss why the second design outperforms the first and complete a set of performance tests on this final design.

Chapter 2

Periodic and Higher Symmetric Structures

This chapter introduces periodic structures and focuses on periodic structures with higher symmetries. First in Sec. 2.1, periodic structures are defined and fundamental properties of wave propagation in periodic structures are recalled. Sec. 2.2 introduces higher symmetries in periodic structures and defines two possible spatial higher symmetries called "glide symmetry" and "twist symmetry". Sec. 2.3 discusses characteristics and applications of higher symmetric structures. The existing models for higher symmetry are discussed in Sec. 2.4. Sec. 2.5 expresses the content of the thesis.

2.1 Wave Propagation in Periodic Structures

2.1.1 Periodic Structures

A structure is periodic along a direction with period p if it is invariant under a translation of length p along that direction. For instance, the structure in Fig. 2.1 (a) is periodic along the x direction, meaning that it is invariant under the translation operator $T_{p\hat{\boldsymbol{x}}}$:

$$T_{p\hat{\boldsymbol{x}}} : (x, z) \rightarrow (x + p, z) \tag{2.1}$$

Similarly, a 2-D periodic structure with periods p_x and p_y along x and y directions respectively would be invariant under the 2-D translation operator $T_{p_x\hat{\boldsymbol{x}}}T_{p_y\hat{\boldsymbol{y}}}$:

$$T_{p_x\hat{\boldsymbol{x}}}T_{p_y\hat{\boldsymbol{y}}} : (x, y, z) \rightarrow (x + p_x, y + p_y, z) \tag{2.2}$$

An example of a 2-D periodic structure is shown in Fig. 2.1 (b).

2.1.2 Floquet Theorem

Assuming time dependency of $e^{j\omega t}$, one can use Maxwell equations to show that in a linear, isotropic and loss-less material the electromagnetic fields satisfy the following equations [1]:

$$\nabla \times [\nabla \times \boldsymbol{E}(\boldsymbol{r})] = \left(\frac{\omega}{c}\right)^2 \epsilon_r(\boldsymbol{r})\, \boldsymbol{E}(\boldsymbol{r}) \tag{2.3}$$

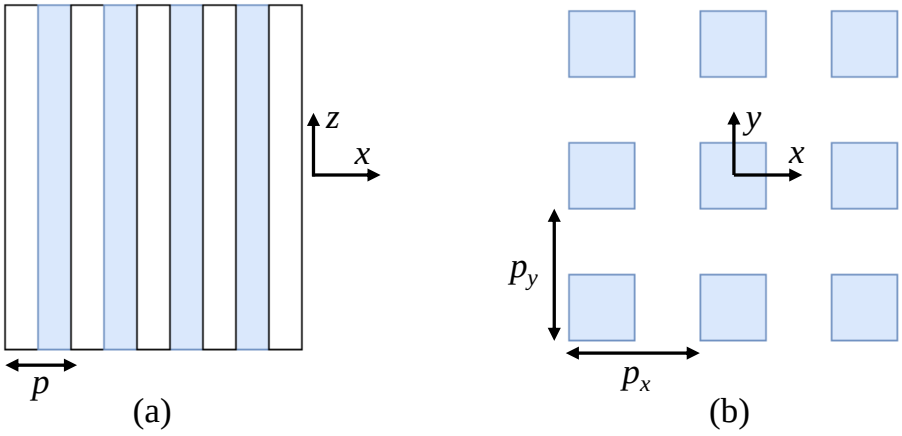

FIGURE 2.1: (a) part of 1-D periodic layers in x direction (b) part of a 2-D periodic pattern of squares in x and y directions.

$$\nabla \times \left[\frac{1}{\epsilon_r(\boldsymbol{r})}\nabla \times \boldsymbol{H}(\boldsymbol{r})\right] = \left(\frac{\omega}{c}\right)^2 \boldsymbol{H}(\boldsymbol{r}) \tag{2.4}$$

where $\boldsymbol{E}(\boldsymbol{r})$ and $\boldsymbol{H}(\boldsymbol{r})$ are the electric and magnetic fields respectively. $\epsilon_r(\boldsymbol{r})$ is the relative permittivity of the material and its relative permeability is $\mu_r = 1$, under the hypothesis of a non-magnetic medium. Solving one of these equations provides $\boldsymbol{E}(\boldsymbol{r})$ or $\boldsymbol{H}(\boldsymbol{r})$. Then the other field can be found using the Maxwell's curl equations:

$$\boldsymbol{H}(\boldsymbol{r}) = \frac{j}{\omega\mu_0}\nabla \times \boldsymbol{E}(\boldsymbol{r}) \tag{2.5}$$

$$\boldsymbol{E}(\boldsymbol{r}) = \frac{1}{j\omega\epsilon_0\epsilon_r(\boldsymbol{r})}\nabla \times \boldsymbol{H}(\boldsymbol{r}) \tag{2.6}$$

For mathematical convenience, it is preferred to solve (2.4) and (2.6) to obtain the electromagnetic fields instead of (2.3) and (2.5) [1]. Therefore, the rest of the discussion uses (2.4) as the initial equation.

The Floquet theorem provides the general form of the solution of the electromagnetic modes for periodic structures. Let the 1-D periodic structure along the x direction of Fig. 2.1 (a) be invariant along the y direction. The unit cell is defined as the smallest section of the structure that can be repeated indefinitely to recreate the periodic structure. The unit cell in Fig. 2.1 (a) has a length of p which is called the period or the lattice constant. The structure is invariant under translation operators with the lattice vectors $\boldsymbol{R} = lp\hat{\boldsymbol{x}}$ where l is an integer. For $l = 1$, the lattice vector becomes $\boldsymbol{R} = \boldsymbol{p} = p\hat{\boldsymbol{x}}$, which is called the primitive lattice vector. The corresponding translation operator in this case is $T_{p\hat{\boldsymbol{x}}}$ given in (2.1).

The solutions of (2.4) are separable in x and y. As stated earlier, the structure is invariant along y direction. This symmetry is a continuous translational symmetry [1] and leads to a y dependence of the solutions of the following form:

$$\boldsymbol{H}(\boldsymbol{r}) \propto \mathrm{e}^{-jk_y y} \tag{2.7}$$

where k_y is the wavevector along the y direction. The solutions of (2.4) are the eigenfunctions of the translation operator $T_{\boldsymbol{R}}$. The eigenfuntions of translation operators are the modes with an exponential form:

$$T_{\boldsymbol{R}}\left[\mathrm{e}^{-jk_x x}\right] = \mathrm{e}^{-jk_x(x-lp)} = \left(\mathrm{e}^{jk_x lp}\right)\mathrm{e}^{-jk_x x} \tag{2.8}$$

where similarly, k_x is called the wavevector along x direction. It is important to note that any eigenfunction in (2.8) with $k_x = k_{x0}$ has the same eigenvalue as all the eigenfunctions with $k_x = k_{x0} + mq$ where $q = 2\pi/p$ and m is an integer. q is called the primitive reciprocal lattice constant and $\boldsymbol{q} = q\hat{\boldsymbol{x}}$ is the primitive reciprocal lattice vector. The fields with $k_x = k_{x0} + mq$ form a degenerate set of solutions, called harmonics. Any linear combination of these fields gives an eigenfunction with the same eigenvalue. Therefore, using (2.7) and (2.8), the solution of (2.4) for the wave vector $\boldsymbol{k} = k_x\hat{\boldsymbol{x}} + k_y\hat{\boldsymbol{y}}$ can be generally expressed as:

$$\boldsymbol{H}_{k_x,k_y}(\boldsymbol{r}) = \mathrm{e}^{-jk_y y}\sum_m c_{k_x,m}(z)\,\mathrm{e}^{-j(k_x+mq)x} \tag{2.9}$$

$$= \mathrm{e}^{-jk_y y}\mathrm{e}^{-jk_x x}\sum_m c_{k_x,m}(z)\,\mathrm{e}^{-jmqx} \tag{2.10}$$

$$= \mathrm{e}^{-jk_y y}\mathrm{e}^{-jk_x x}\boldsymbol{u}_{k_x}(x,z) \tag{2.11}$$

where $c_{k_x,m}(z)$ are the expansion coefficients and $\boldsymbol{u}_{k_x}(x,z)$ is a periodic function with a period p along the x direction. This means that the electromagnetic field modes in a periodic structure with a period p along the x direction are plane waves multiplied by a periodic function with the same period p along the x direction. Hence, the electromagnetic fields are of the following form:

$$\boldsymbol{E}(x,y,z) \propto \mathrm{e}^{-jk_x x}\boldsymbol{u}_{k_x}(x,y,z) \tag{2.12}$$

$$\boldsymbol{H}(x,y,z) \propto \mathrm{e}^{-jk_x x}\boldsymbol{u}_{k_x}(x,y,z) \tag{2.13}$$

These modes are called the Bloch modes (or Floquet modes) of the structure. Applying the translation operator $T_{p\hat{\boldsymbol{x}}}$ to these modes leads to:

$$T_{p\hat{\boldsymbol{x}}}\left[\boldsymbol{E}(x,y,z)\right] = \boldsymbol{E}(x+p,y,z) = \mathrm{e}^{-jk_x p}\boldsymbol{E}(x,y,z) \tag{2.14}$$

$$T_{p\hat{\boldsymbol{x}}}\left[\boldsymbol{H}(x,y,z)\right] = \boldsymbol{H}(x+p,y,z) = \mathrm{e}^{-jk_x p}\boldsymbol{H}(x,y,z) \tag{2.15}$$

These equations are known as the Bloch theorem (or Floquet theorem).

In general, k_x is a complex quantity and can be written as $k_x = \beta_x - j\alpha_x$. Its real part ($\beta_x$) is called the phase constant and it represents the change in phase of the electromagnetic fields per unit length along the x direction at any instant. The opposite of its imaginary part (α_x) is the attenuation constant of the corresponding Bloch modes. This quantity is of importance in stopbands where attenuation of the fields occurs to estimate the attenuation strength and in passbands where propagation exists to estimate losses including material and radiation losses.

2.1.3 Dispersion Relation and Brillouin Zone

Propagation properties of a structure are obtained by studying its dispersion relation. The dispersion relation is a relation between the frequency and propagation constants of an electromagnetic mode. It is commonly visualized in a plot showing the frequency vs. the phase constant of the Floquet mode: the dispersion diagram. Substitution of (2.13) in (2.4) provides the dispersion relation for the 1-D periodic structure along the x direction. As it was mentioned before, changing k_x by integral multiples of $q = 2\pi/p$ does not change the corresponding frequency. This means that the dispersion relation $\omega(k_x)$ is periodic with period q which means that it is enough to find the dispersion relation for $-\pi/p < k_x < \pi/p$ and the rest of the dispersion diagram is known from the periodicity of the result. This region of k_x values is called the Brillouin zone.

When a periodic structure has a rotation, mirror reflection or inversion symmetry, its dispersion diagram ($\omega(\boldsymbol{k})$ where $\boldsymbol{k}$ is the wave vector) is also symmetric with the same symmetry [1]. In these cases, there are further redundancies within the Brillouin zone and the smallest region for which the frequency band is not repeating itself is called the irreducible Brillouin zone [1].

The Brillouin zone for a periodic structure is defined by its lattice vectors. For instance, a periodic structure with a rectangular lattice is shown in Fig. 2.2 (a). The lattice vectors are $\boldsymbol{p_x} = p_x\hat{\boldsymbol{x}}$ and $\boldsymbol{p_y} = p_y\hat{\boldsymbol{y}}$. The reciprocal lattice vectors in k_xk_y plane are $\boldsymbol{q_x} = (2\pi/p_x)\,\hat{\boldsymbol{x}}$ and $\boldsymbol{q_y} = (2\pi/p_y)\,\hat{\boldsymbol{y}}$ which are depicted in Fig. 2.2 (b). The Brillouin zone is shown in Fig. 2.2 (c) with orange rectangular area around the center which is bounded by red lines $k_x = \pm\pi/p_x$ and $k_y = \pm\pi/p_y$.

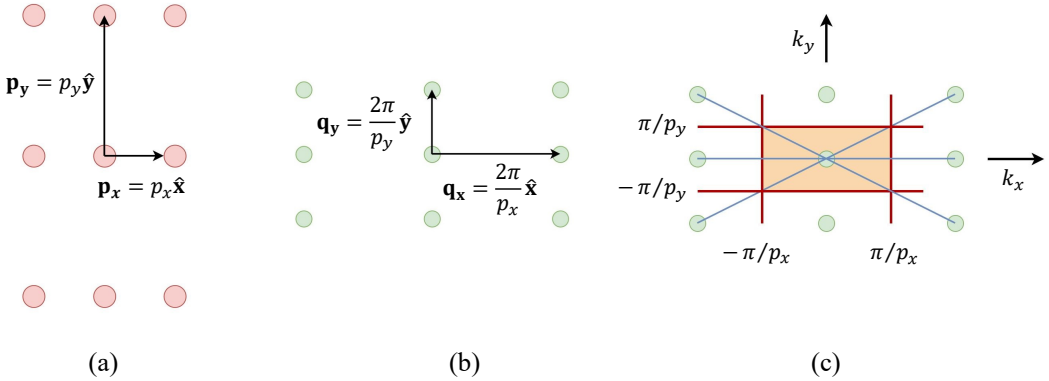

FIGURE 2.2: (a) Lattice vectors of a 2-D periodic structure with period p_x along x direction and period p_y along y direction. (b) The reciprocal lattice vectors in k_xk_y plane (c) Brillouin zone (orange rectangle).

For a periodic structure with a square lattice ($p_x = p_y = p$), a 90° rotation symmetry exists in addition to the translation symmetry imposed by the periodicity. A square lattice with its corresponding lattice vectors are shown in

Fig. 2.3 (a). In this case, the Brillouin zone is defined as a square limited by the lines $k_x = \pm\pi/p$ and $k_y = \pm\pi/p$. This area is shown in Fig. 2.3 (b). The irreducible Brillouin zone is a triangle wedge that is also shown in Fig. 2.3 (b) (the red triangle) and its area is $1/8$ of the Brillouin zone area. It is common to obtain the dispersion diagrams of these periodic structures over the edges of the irreducible Brillouin zone. These edges connect the points Γ, X and M shown in Fig. 2.3 (c).

In addition to the dispersion diagram which plots the frequency vs. the phase constant of a Floquet mode, an attenuation diagram is sometimes plotted. This diagram plots the frequency vs. the attenuation constant of a mode. It provides the extra information missed by the phase diagram on the complex nature of a mode or on the evanescent nature of a mode in its stopbands.

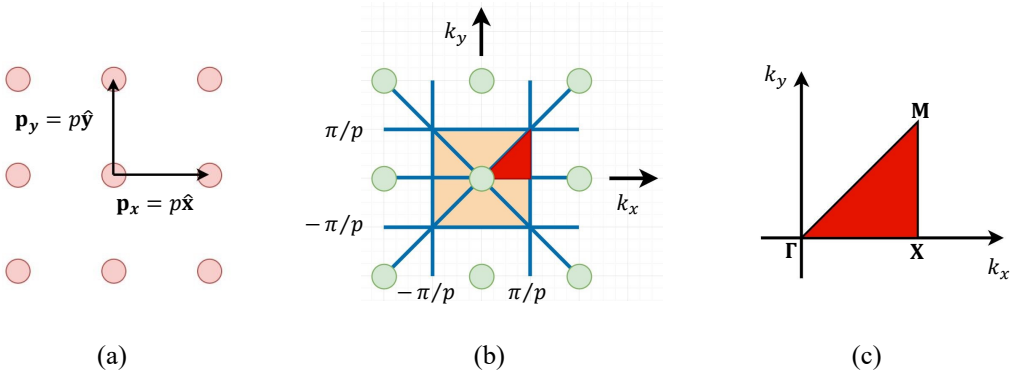

FIGURE 2.3: (a) Lattice vectors of a 2-D periodic structure with the same period p along x and y directions. (b) The Brillouin zone (orange square) and the irreducible Brillouin zone (red triangle) (c) Irreducible Brillouin zone and the conventional name of its 3 corners.

2.2 Higher Symmetries in Periodic Structures

Periodic structures with higher symmetries are structures that can be described by additional geometrical operations beyond the usual periodic condition. Periodic structures are invariant under translations of period length. In periodic structures with higher symmetries, in addition to the periodic condition, the unit cell is invariant under a composite transformation consisting of either translation and rotation or translation and mirroring. The higher symmetry that is constructed by translation and rotation is called twist symmetry (also called screw symmetry) and the one constructed by translation and mirroring is called glide symmetry.

Fig. 2.4 shows two structures with glide symmetry. A translation of half a period and a mirroring operation with respect to the mirroring plane (also called the glide plane) ensures a periodic structure with a glide symmetry. Fig. 2.4 (a) shows a 1-D glide symmetry which is achieved by translation

and mirroring of the PEC slabs in the line. Fig. 2.4 (b) shows glide symmetry in a 2-D periodic structure. To better understand the glide symmetry in periodic structures, we define the glide symmetry operator in one and two dimensions. The 1-D glide symmetry operator $G_{p\hat{\boldsymbol{x}}}$ can be considered as a composition of an x-translation of length $p/2$ and a z-reflection around the glide plane (here we choose $z = 0$ as the glide plane) [2]:

$$G_{p\hat{\boldsymbol{x}}} : (x, z) \rightarrow (x + p/2, -z) \tag{2.16}$$

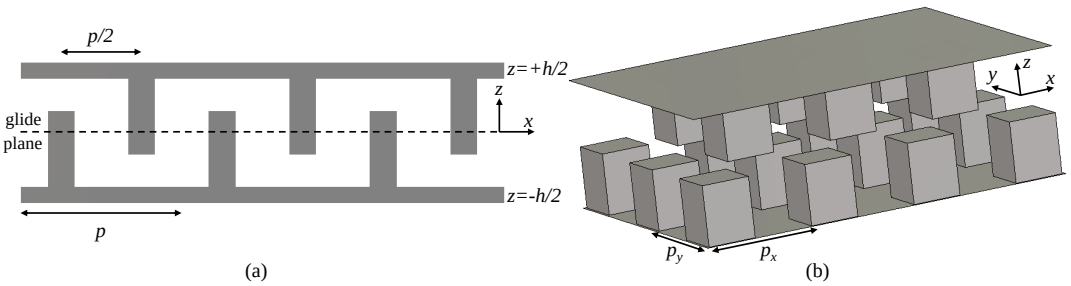

FIGURE 2.4: Geometry of glide-symmetric structures: (a) 1-D glide symmetry in a line loaded with PEC slabs (b) 2-D glide symmetry in a parallel plate waveguide loaded with rectangular pins

A 1-D glide-symmetric periodic structure is invariant under this glide symmetry operator. A comparison of (2.16) and (2.1) shows that composition of two glide symmetry operators is the translation operator ($G^2_{p\hat{\boldsymbol{x}}} = T_{p\hat{\boldsymbol{x}}}$). This was of course expected as a glide-symmetric structure is periodic in its nature.

Similar to a 1-D glide-symmetric structure, the 2-D version is invariant with respect to the glide symmetry operator. The 2-D glide symmetry operator $G_{p_x\hat{\boldsymbol{x}},p_y\hat{\boldsymbol{y}}}$ for a periodic structure with periods p_x in x and p_y in y direction, is defined as:

$$G_{p_x\hat{\boldsymbol{x}},p_y\hat{\boldsymbol{y}}} : (x, y, z) \rightarrow \left(x + p_x/2, y + p_y/2, -z\right) \tag{2.17}$$

Just as in the 1-D case, the defined glide symmetry operator provides periodicity, since two consecutive applications $G^2_{p_x\hat{\boldsymbol{x}},p_y\hat{\boldsymbol{y}}} = T_{p_x\hat{\boldsymbol{x}}}T_{p_y\hat{\boldsymbol{y}}}$ give the 2-D translation operator defined in (2.2). This assures the periodicity of the structure.

Fig. 2.5 shows an example of a periodic structure with twist symmetry. The structure is a coaxial cable in which half-rings are attached to its outer conductor. These half-rings are rotated and translated along the coaxial cable's length to create twist symmetry. A twist-symmetric object is obtained if the object replicates itself indefinitely when translated p/N along a line and rotated an angle $2\pi/N$ around the same line (where N is an integer). After N such transformations, the object has experienced a net translation of p, thus defining a period composed of N adjacent parts, each of them identical apart from a rotation. This symmetry is called an N-fold twist symmetry. This

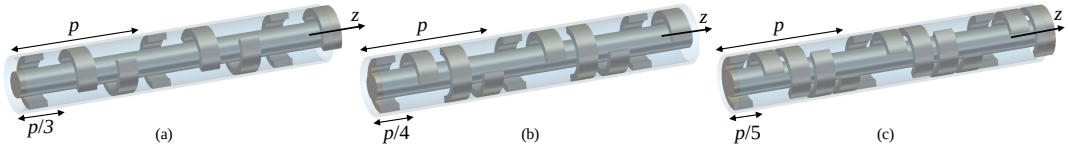

FIGURE 2.5: Geometry of a twist-symmetric structure (a coaxial cable with metallic half-rings attached to the outer conductor: (a) 3-fold twist-symmetric (b) 4-fold twist-symmetric (c) 5-fold twist-symmetric.

naming is due to the fact that the unit cell of such structure has N sub-unit cells that are rotated and translated with respect to each other. We can define the N-fold twist symmetry operator as [2]:

$$S_{N,p\hat{z}} : (\rho, \phi, z) \rightarrow \left(\rho, \phi + \frac{2\pi}{N}, z + \frac{p}{N}\right) \tag{2.18}$$

N consecutive applications of the N-fold twist operator result in the 1-D translation operator $S^N_{N,p\hat{z}} = T_{p\hat{z}}$ of a period length, which confirms that a twist-symmetric line is also periodic.

The two higher symmetries described here are of interest in electromagnetics research. In fact, these symmetries provide periodic structures with new interesting characteristics that can be used to enhance different features of many microwave components. They have recently found applications in numerous areas, such as wideband artificial lenses, leaky-wave antennas and electromagnetic bandgap materials. This motivates a need for proper modeling of higher symmetric structures, which can help the design of new devices and which can give physical insight into their physical properties. The applications of higher symmetric structures will be covered in more depth in the next section.

2.3 Applications of Higher Symmetries

2.3.1 Early studies

Introducing a spatial higher symmetry within a unit cell of a periodic structure provides interesting dispersive properties that make these structures proper candidates for numerous electromagnetic applications. In the 1960's and 70's, one dimensional periodic structures with twist and glide symmetries were studied using a generalized Floquet theorem to provide initial insights on the characteristics of these symmetries [2, 3, 4, 5]. In these works, the influence of higher symmetries on the propagation characteristics of the guided and radiating fields were studied. [2] introduces a generalized Floquet theorem for periodically loaded closed waveguides possessing twist and glide symmetries. The theorem states that the Bloch modes are eigenvectors of the glide or twist symmetry operator characterizing the structure. Based upon this theorem, it also presents a method to construct the Brillouin

diagrams of higher symmetric structures qualitatively. This method predicts which stop bands will be present or absent in the dispersion diagram by considering the mode couplings between modes of the unloaded structure and their space harmonics. [3] discusses the higher symmetry operators as well. By means of mode-coupling theory it discusses how higher symmetries can uncouple some space harmonics of the unloaded guide and then suppress some stopbands. The results of these classical theoretical studies, such as the lack of a stopband and a larger passband will be discussed in the next paragraphs.

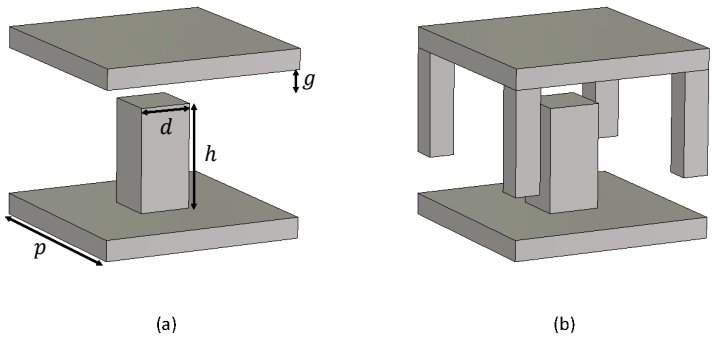

FIGURE 2.6: Unit cell structure of periodic bed of nails: (a) non-glide symmetric (b) glide-symmetric.

2.3.2 Reduced frequency dispersion and lens antennas

Recently, a surge of interest in studying 2-D periodic structures with glide symmetry has started in the framework of metamaterial research [6, 7, 8, 9, 10]. It was demonstrated in [11] that application of higher symmetries to two dimensional periodic structures reduces their frequency dispersion. To understand this phenomenon, let's consider the periodic bed of nails structure with a top plate whose unit cell is shown in Fig. 2.6 (a). Fig. 2.6 (b) shows the glide-symmetric version of this structure which is achieved by mirroring the central pin to the top plate and moving half a period $P/2$ in both the lateral directions. Fig. 2.7 depicts the normalized phase constant versus the frequency for the two aforementioned unit cells. The parameters were chosen as $p = 4$ mm, $d = 0.5$ mm, $h = 1$ mm and $g = 0.1$ mm. Firstly, the stopband has moved to higher frequencies for the glide-symmetric structure. Secondly, the curve of the first Bloch mode has become almost straight for the glide-symmetric cell. This linear dependency over a wide range of frequency means that this mode is essentially *nondispersive*.

[11] also investigates a glide-symmetric holey structure rather than the bed of nails configuration. Glide-symmetric holey metasurfaces show similar characteristics to their bed of nails counterparts. Fig. 2.8 (a) shows the unit cell of a holey periodic structure with a top plate cover. Fig. 2.8 (b) shows the glide-symmetric counterpart where the glide symmetry was achieved by moving the mirrored holes half a unit cell $P/2$ in both lateral directions. The

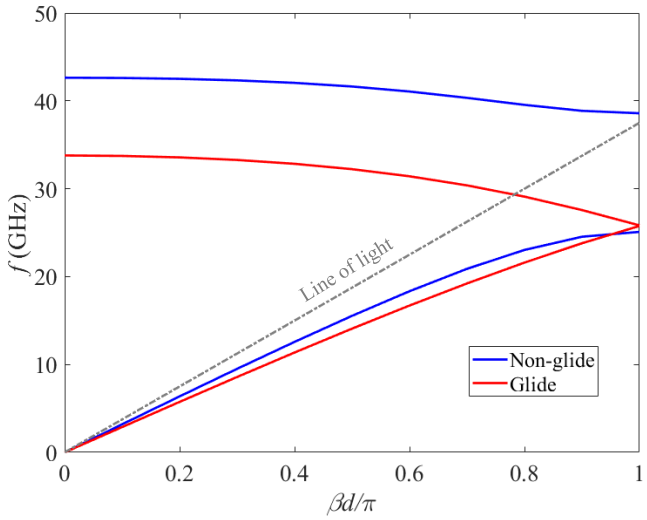

FIGURE 2.7: Dispersion diagram of glide-symmetric versus non-glide symmetric bed of nails shown in Fig. 2.6.

dispersion diagram of these two unit cells are compared in Fig. 2.9. This figure shows that the glide-symmetric unit cell has a higher refractive index compared to the non-glide symmetric cell, realizing a denser material. This is very useful for lens design. We also notice that similar to the bed of nails configuration, the glide-symmetric holey structure is again nondispersive. This can be observed by the linear dependence of the phase constant on the frequency for the first Bloch mode.

This is very important for the design of planar lens antennas since the bandwidth can be noticeably increased. [11] discusses this characteristic and suggests that the less dispersive behavior of metasurfaces with higher symmetries can be utilized in the design of ultrawideband lenses. The paper furthermore discusses how the glide-symmetric holey surfaces can be used to achieve the refractive index profile of a two-dimensional Luneburg lens. Different hole depths h could be used to achieve different refractive indices required to realize a Luneburg lens.

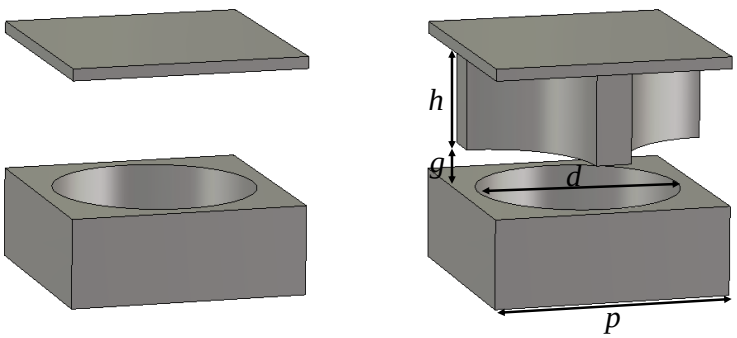

(a) (b)

FIGURE 2.8: Holey unit cells with top cover: (a) non-glide symmetric (b) glide-symmetric.

[12] [13] designed and fabricated a fully metallic Luneburg lens for 5G communications at Ka-band. The fully metallic structure ensures lower losses at millimeter waves due to the absence of the dielectric material. These concepts were later reviewed in [14] with a focus on the prospect of the benefits of metasurfaces with higher symmetries in 5G technology. Fully metallic glide-symmetric metasurfaces were proposed as a low-cost, low-loss and wideband solution to 5G communications in millimeter wave regimes.

Based on these results, [15] proposes a transformation-optics rule to convert the circular focal curve of a conventional Luneburg lens realized with a bed-of-nails to a flattened focal line. This simplifies the feeding network and reduces the lens size. The refractive index distribution of the transformed lens is realized by choosing the height of the pins in a glide-symmetric bed of nails configuration. Results are given using electromagnetic simulations.

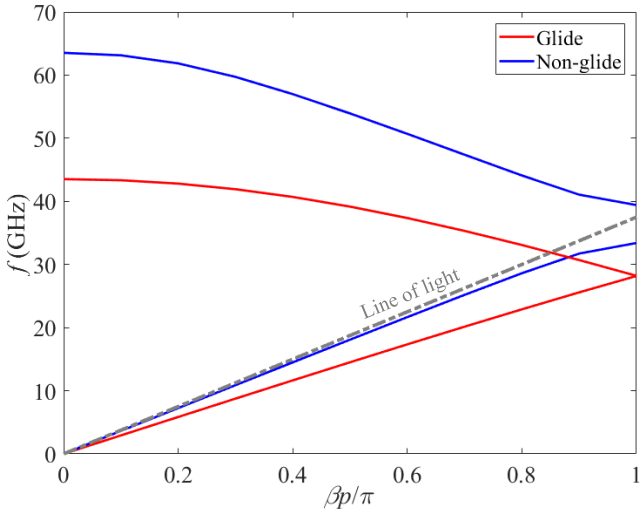

FIGURE 2.9: Dispersion diagram of glide-symmetric versus non-glide symmetric holey structure shown in Fig. 2.8

2.3.3 Backward radiation and leaky-wave antennas

Glide-symmetric open waveguides have also been studied in order to implement leaky-wave antennas [7]. The structures discussed in [7] are shown in Fig. 2.10. The structure is a U-shaped metallic groove with periodic metallic slices. These metallic slices could be aligned in a non-glide symmetric periodic pattern as shown in Fig. 2.10 (a) or in a glide-symmetric pattern as shown in Fig. 2.10 (b). The dispersion diagrams of these two structures are shown in Fig. 2.11. The geometrical parameters were chosen as $h = 23$ mm, $h_1 = 5$ mm $w = 10$ mm $w_1 = 5$ mm, $w_2 = 2.5$ mm, $d = 9$ mm and $a = 2.25$ mm. Fig. 2.11 (a) depicts the normalized phase constant versus the frequency for the non-glide symmetric structure. We know that for open structures, if the dispersion curve of a Bloch mode in the first Brillouin diagram lies below the line of light, it means that the mode is bound to the structure and is not radiating. On the other hand, if part of the curve lies above

the line of light (the radiation region), that part of the curve corresponds to a radiating wave. The propagation constant will be complex to take into account of radiation losses, and the wave will radiate as it propagates along the line. A quick look at the figure suggests that in the non-glide symmetric case, dispersion curves of the first two modes are below the line of light. Therefore, there is no radiation. The cut-off frequencies of the first two modes are 6.19 GHz and 14.05 GHz respectively while the asymptotic frequencies of these modes are 10.65 GHz for the first mode and 14.512 GHz. Therefore, the first mode has a bandwidth of 4.46 GHz while a stopband separates the passbands of the first and second mode.

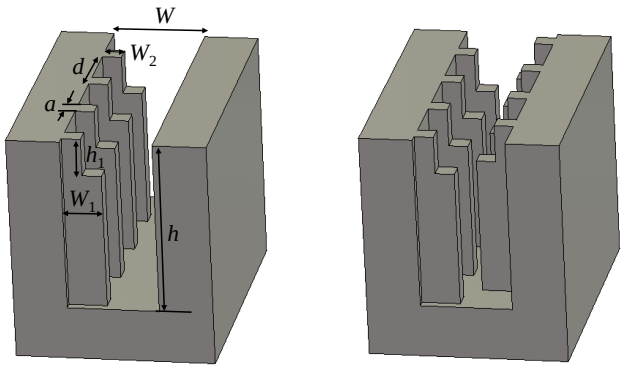

(a) (b)

FIGURE 2.10: Geometry of the structures discussed in [7]: (a) non-glide symmetric structure (b) glide-symmetric structure.

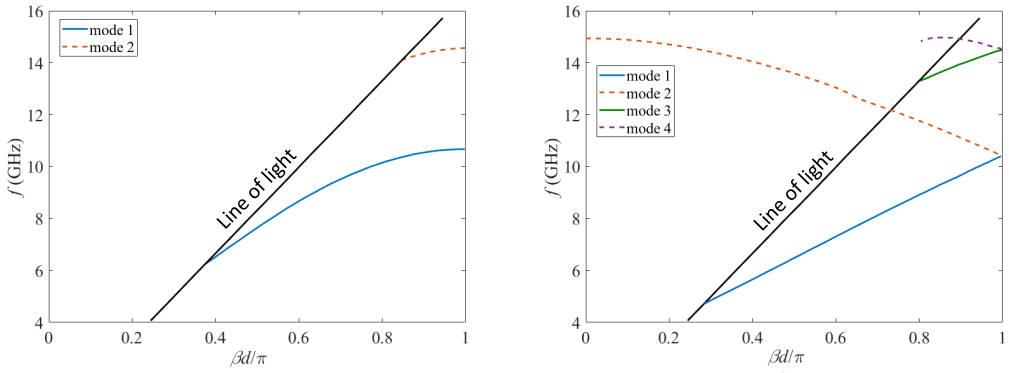

(a) (b)

FIGURE 2.11: Dispersion diagram of the structures in Fig. 2.10 repeated from [7]: (a) non-glide symmetric structure (b) glide-symmetric structure.

Fig. 2.11 (b) depicts the dispersion diagram for the glide-symmetric version of the structure. We observe that in this case, the first and the third mode have a positive group velocity while the second and the fourth mode show negative group velocities. Similar to the closed structures discussed before, we notice that the dispersion curve of the first mode has become linear. Since

part of the second mode's curve (including the cut-off frequency) are below the line of light, these frequencies can also act as a passband for transmission of the wave. Therefore, the lowest passband here corresponds to both first and second mode. The structure shows a bandwidth of 7.467 GHz (from the cut-off frequency of the first mode at 4.696 GHz to the frequency in which the second mode's curve passes the line of light at 12.163 GHz) which shows a 67% increase compared to non-glide symmetric structure. Furthermore, we see that the second mode passes the line of light at 12.163 GHz. This means that this mode is radiating at frequencies higher than 12.163 GHz. Therefore, this structure can be used to design leaky-wave antennas with beam scanning capabilities in this frequency range. A very recent design of leaky-wave antenna using glide-symmetric structures can be found in [16]. The authors of that paper use the novel multi-modal analysis method that we have previously introduced (and that is described in the next chapter as part of this thesis) as a tool for design of the antenna.

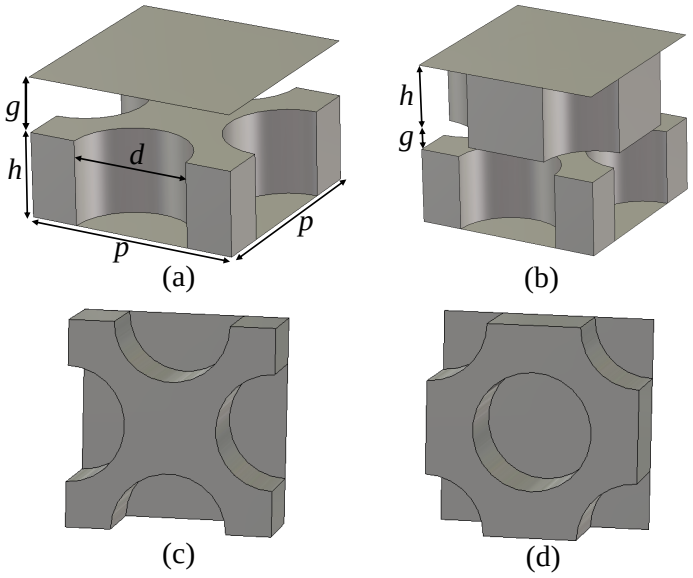

FIGURE 2.12: (a) Holey non-glide symmetric unit cell (b) Holey glide-symmetric unit cell (c) Bottom plate of the glide-symmetric cell (d) Top plate of the glide-symmetric cell.

2.3.4 Enhanced stopband and microwave components

Higher symmetries have also recently been used in design of low-loss waveguide structures. This is due to improvement of both the frequency width and the attenuation of stop-bands offered by 2-D glide-symmetric metasurfaces with respect to simple periodic structures. These configurations offer new solutions for field confinement and gap-waveguide technology [17, 18, 19]. [17] studies the basic glide-symmetric holey metasurface as an electromagnetic bandgap structure. The metasurface is shown in Fig. 2.12 (b) while its corresponding non-glide symmetric unit cell is given in Fig. 2.12 (a). To better visualize the unit cell, the bottom and top sections of the glide symmetric

unit cell are given in Fig. 2.12 (c) and (d) respectively. Considering the parameters $p = 5$ mm, $d = 2.8$ mm, $h = 2$ mm and $g = 0.05$ mm, complete dispersion diagrams for the non-glide symmetric and glide symmetric structures are shown in Fig. 2.13 and Fig. 2.14 respectively. A quick comparison of the two figures show that the stopband in the non-glide symmetric case has a wide bandwidth only in the X-M direction while the stopband has a low bandwidth in the Γ-X and M-Γ directions. On the other hand, the introduction of the glide symmetry provides a wide bandwidth for the stopband in all directions. This is very useful in gap-waveguide technology to confine the fields in the waveguiding areas and prevent the leakage of power. [17] executes a parameter analysis on the aforementioned glide-symmetric holey metasurface and demonstrates that the periodicity of holes determines the center frequency of the stopband while the gap can be adjusted to achieve the required stopband range. This provides the designer with an effective way of modifying the stopband range according to the requirements. [18] uses these observations and proposes a cost-effective gap waveguide technology based on the glide-symmetric holey metasurfaces. Three cases of straight waveguide, double 90° bent waveguide and coupled waveguides were simulated, fabricated and measured to demonstrate the feasibility of the waveguiding structure.

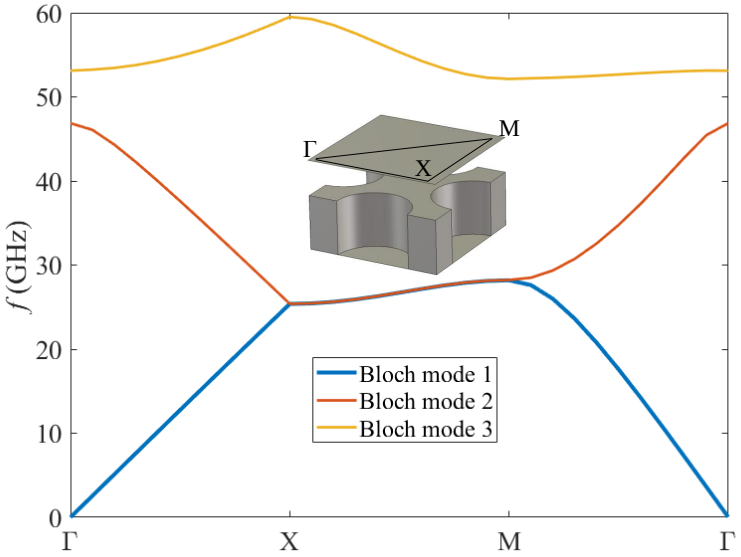

FIGURE 2.13: Complete dispersion diagram of the non-glide symmetric unit cell in Fig. 2.12 (a)

The implementation of glide symmetric structures as efficient EBG materials in gap waveguide technology opens up a wide variety of opportunities for design of different components aimed at various applications. For instance, [19] uses the holey metasurface with glide symmetry for designing a phase shifter in the U-band by using a thin dielectric slab inserted in the waveguide to control the phase shift of the signal. Another more recent implementation of the holey glide-symmetric structures in gap waveguide

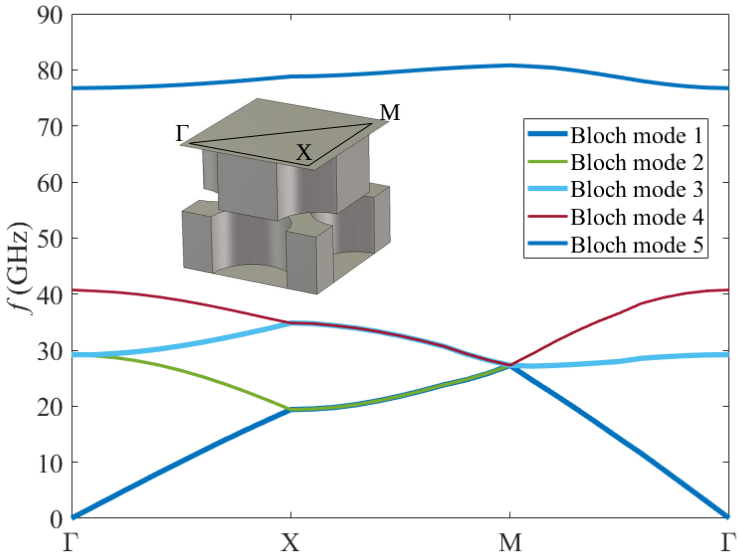

FIGURE 2.14: Complete dispersion diagram of the glide symmetric unit cell in Fig. 2.12 (b)

technology is given in [20] which designs a 4×4 slot array antenna. This design uses a higher order mode excitation TE_{40} based on a TE_{10} to TE_{20} mode converter. Two converters are used to produce the TE_{40} mode from two in-phase adjacent TE_{20} modes. This feeding network eases the manufacturing process by avoiding drilling of thin and vertical metallic walls as a separation between waveguides. Finally, since dielectric loss are absent in gap waveguide technology and the leakage can be properly limited through efficient glide-symmetric EBG, the designed antenna proved to have low loss.

2.3.5 Breaking glide symmetry

Another interesting recent application of glide symmetry is the breaking of the glide symmetry in holey metasurfaces as in Fig. 2.15 (a) [21]. It is shown that by breaking the glide symmetry, the bandgap can be split into two separated ones. In fact, the second mode shifts toward higher frequencies thus introducing a passband within the original bandgap. Different transformations can break the glide symmetry. The aforementioned work proposes the combination of two transformations: varying independently the radii of glide symmetric holes in the top and bottom surfaces, as in Fig. 2.15 (b), and introducing an additional misalignment between the top and bottom surfaces, as in Fig. 2.15 (c). The first transformation creates a new passband, absent in glide-symmetric structures, and controls its bandwidth. The second transformation moves the central frequency of the new passband. Therefore, proper combination of these two methods leads to bandwidth splitting in gap waveguide technology. Fig. 2.15 shows the unit cell of a holey periodic structure and the two methods to break its glide symmetry.

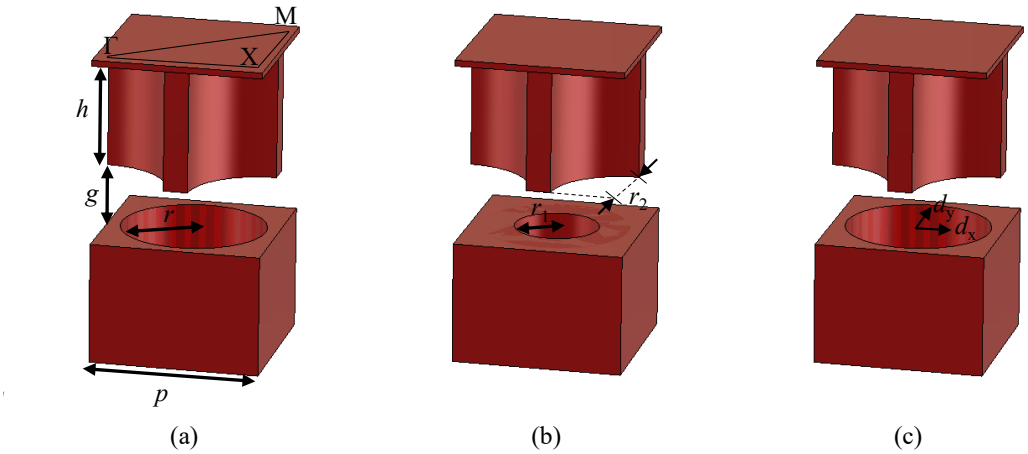

FIGURE 2.15: Holey unit cell (a) with glide symmetry (b) with broken glide symmetry achieved by using different radii for the holes on the top and bottom plates (c) with broken glide symmetry achieved by offsetting one of the two plates of a distance d_x and d_y in x and y directions respectively.

Fig. 2.16 shows the effect of breaking the glide symmetry. Fig. 2.16 (a) displays the full dispersion diagram of the glide-symmetric structure depicted in Fig. 2.15 (a). As expected, the diagram shows a stopband only between the second and third Bloch mode. By breaking the symmetry using an additional offset shift between the plates , the dispersion diagram achieved is shown in Fig. 2.16 (b). The second Bloch mode has been shifted to higher frequencies thus splitting the wide stopband into two smaller ones. Finally, Fig. 2.16 (c) displays the full dispersion diagram of the holey structure when the symmetry is broken by varying the size of hole radii in the two plates in addition to offsetting the two. Similar to the previous case, the broken glide symmetry results in splitting the stopband in two. Therefore, controlling hole radii variation and the offset between the plates provides proper means of tuning the two stopbands and hence the passband between them.

The extra tunable passband between two bandgaps in structures with broken glide symmetry opens new possibilities in electromagnetic applications. For instance, this passband can be used for filtering purposes of a desired frequency band in gap waveguide technology by suppressing the lateral confinement of the fields in the guide in that band. This means that at the suppressed frequency the signal would leak transversely through the gap and would be prevented to reach the output port of the waveguide. A sheet of an absorbing material can rapidly dissipate the leaked fields and avoid undesired coupling in other parts of the structure. Even though this proposed filtering technique does not allow to accurately define a filter in terms of band rejection, it can still be useful when integration of a filtering cavity into the available space is not possible or an extra filtering is needed in a certain frequency band.

In the previous application, a filtering effect was integrated into the gap waveguide structure through breaking the glide symmetry of the lateral EBG.

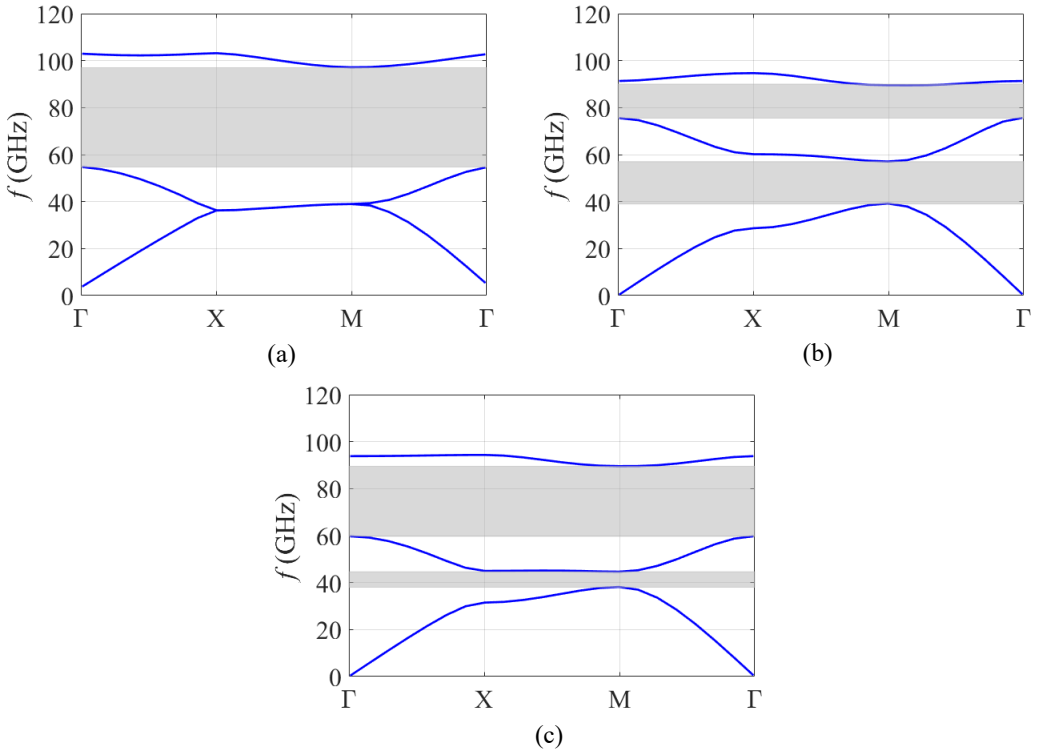

FIGURE 2.16: Full dispersion diagram of the holey structure in Fig. 2.15 with $p = 2.8$ mm, $g = 0.05$ mm, $h = 2$ mm, (a) $r_1 = r_2 = r = 1.1$ mm and $d_x = d_y = 0$ mm (glide symmetry) (b) $r_1 = r_2 = r = 1.1$ mm and $d_x = d_y = 0.5$ mm (broken glide symmetry due to offsetting the two plates) (c) $r_1 = 1.1$ mm, $r_2 = r = 1.2$ mm and $d_x = d_y = 0.2$ mm (broken glide symmetry due to both offsetting the two plates and varying the hole radius in the two plates).

However, it is also possible to use similar ideas to design filters based on broken glide symmetric periodic structures in the guiding medium. This has been done in [22] using braided glide symmetry. This symmetry is the result of combination of two 1-D glide symmetries: one along the longitudinal direction and the other along the transverse direction. Fig. 2.17 shows the braided glide-symmetric unit cell composed of holes in metallic plates. The braided glide symmetry increases the attenuation per unit cell in the stopband. This minimizes the required space for a given level of attenuation. The broken glide symmetry is used in [22] to create multiple passband and stopbands and suppress higher-order harmonics (in this case, the second-order harmonic). The main difference with the previous example is that here the stopband is used to filter the wave propagation in the guiding region whereas in the previous example, the periodic structure was used as an EBG and the passband was used to deactivate the EBG and to suppress the field by making it laterally leaking. The advantage of this technology compared to other similar filtering periodic structures such as waffle iron [23] is due to its cost-efficiency and robustness. The designed filter can be integrated into an antenna to reduce the overall loss. As a disadvantage, it needs a very narrow

air gap to achieve high attenuation in small distances.

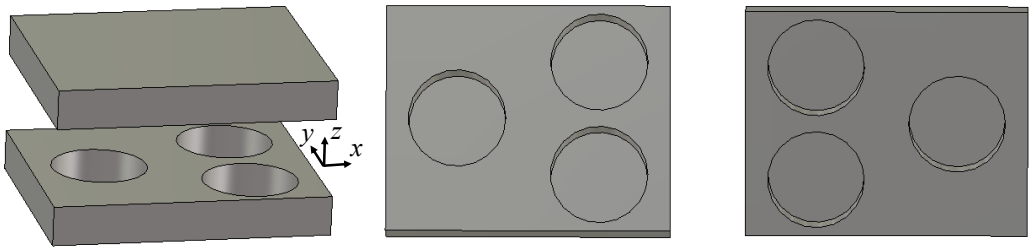

(a) (b) (c)

FIGURE 2.17: (a) Unit cell of a braided glide symmetric structure. (b) Bottom layer of the unit cell (c) Top layer of the unit cell.

2.3.6 Glide-symmetric flanges

Glide symmetry has also found application in waveguide flanges. Leakage at microwave joints can be caused by undesired gaps between flanges of the two mating waveguides due to misalignment, surface curvature, dirt or human mistakes. At higher frequencies this leakage is more significant since the small air gaps are comparable to the wavelength. Due to the air gap between the two waveguides, the transition between them behaves as a cavity, exciting multiple resonances. In addition, the extra pin and screw set up that are used for alignment of the waveguides may also excite new resonances. If any of these resonances are inside the operational frequency, the transmission may get affected significantly. [24] proposes a glide-symmetric holey structure on the flanges which minimizes the effect on the transmission in the presence of an air gap. The proposed method has multiple advantages over the previous pin-type EBGs used on flanges [25]. The first advantage is an easier manufacturing since drilling holes is simpler than milling corrugations. Another advantage is in the larger period required in the glide-symmetric holey structure compared to pin-type structures. This larger period provides less sensitivity to manufacturing tolerances. Finally, the depth of these holes does not significantly affect the resulting stopband. This provides a small sensitivity to manufacturing tolerances.

2.3.7 Matching improvement of dielectric discontinuities and printed circuits

Recently, glide symmetry has also been used to match discontinuities due to highly dense dielectric profiles illuminated under a wide angle and in a broad bandwidth [26]. Fig. 2.18 (a) shows a parallel plate waveguide filled with a medium with $\epsilon_{r1} = \mu_{r1} = 1$ that faces a denser dielectric slab with

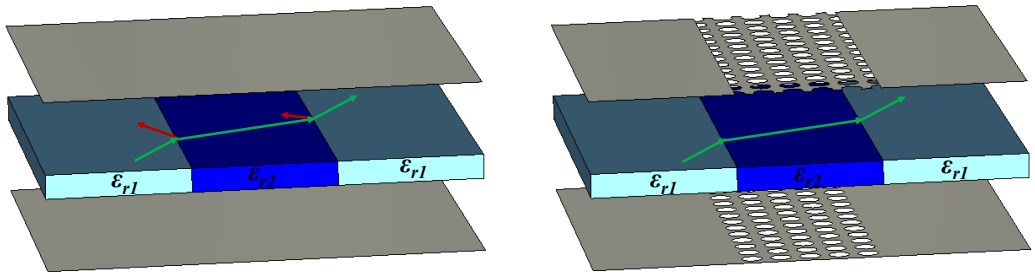

(a) (b)

FIGURE 2.18: A parallel plate waveguide with two different media with permittivities ϵ_{r1} and ϵ_{r2} inside with: (a) Unmatched impedances that cause reflections between the two media (shown with red arrows) (b) matched impedances by using subwavelength glide-symmetric structures over the middle media.

$\epsilon_{r2} > 1$ and $\mu_{r2} = 1$ which presents a classical problem of electromagnetic reflection at the interface between two media. If the value of permeability of the denser media is somehow changed to $\mu_{r2} = \epsilon_{r2}/\epsilon_{r1}$, the two media will have the same impedance and the reflections will vanish. To do so, sub-wavelength scatterers are able to mimick a certain permeability. For instance, sub-wavelength periodic holes on metallic plates can increase the effective permeability. This is shown in Fig. 2.18 (b) where the second media in the parallel plate waveguide is covered with glide-symmetric holey metallic plates. [26] has successfully used this method to match the impedance for normal incidence in a parallel plate configuration and has validated it through experiments. It also considers the case of oblique incidence for which it uses full wave simulations to show how using this method, it is possible to match the profile of a dielectric hyperbolic lens to free space.

In addition to the applications in gap waveguide technology, configurations exhibiting glide-symmetry can also improve devices realized in planar technologies such as printed circuit boards. For instance, [27] has demonstrated that introduction of glide symmetry in a double-sided array of parallel strips using printed corrugations can suppress a stopband between the first and the second mode while keeping a high linearity of the propagation constant. Furthermore, it shows how breaking this symmetry can cause filtering effects which can be used in this technology. Other results [28] shows how to improve the stopband of a conventional mushroom-like EBG structure in microstrip technology by simply introducing a glide symmetry in its structure. The conventional mushroom-type EBG has all its vias on one side with no glide symmetry. By placing the vias in a glide-symmetric fashion, it is possible to achieve a 80 % higher stopband bandwidth.

2.3.8 Properties of twist symmetric lines

Despite less research has been performed on twist-symmetric lines, many of the characteristics of the glide symmetry are also relevant in twist symmetry. For instance, [29, 30, 31, 32] show that similar to the glide symmetry, twist symmetry can be used to reduce the frequency dispersion of a periodic structure in addition to controlling the location and width of the stopbands. Moreover, by changing the number of folds in a twist symmetry the equivalent refractive index of the media can be controlled [29]. Due to the similarity of their behavior to glide-symmetric structures, twist-symmetric structures may also find potential applications in leaky-wave antennas and fully metallic filters and phase shifters.

2.4 Existing models for higher symmetries

As it was described in Sec. 2.3, the interesting dispersive effects of higher symmetries and their applications in microwave technology have recently stimulated research in numerical and analytical methods in order to explain the effect of these symmetries in periodic structures. On one hand, the proximity required between glide-symmetric surfaces to obtain these interesting effects can lead to time-consuming simulations when commercial software is used due to the need of meshing small geometrical details. On the other hand, such a difference between glide and non-glide surfaces is not yet fully explained, and physical insight would allow for a better comprehension of these structures.

Recently, mode-matching has been proposed for glide-symmetric holey metasurfaces and corrugations. [33] proposes a mode matching technique capable of deriving efficiently the dispersive characteristics of glide-symmetric metallic plates with periodic rectangular holes. It exploits the higher symmetry of each cell and uses the generalized Floquet theorem to enforce boundary conditions only on one of the two surfaces. This leads to a discussion of the symmetric properties of the Floquet harmonics, whose parity depends on the parity of the order of the harmonic. It also studies and confirms the potential of tuning the refractive index of the structure by changing different geometrical parameters which makes them suitable for design of ultra-wideband lenses. [34] analyzes the glide-symmetric 2-D doubled corrugated metasurface using the mode-matching technique. The result is accurate and the method is computationally faster than commercial software.

Despite its advantages, mode matching does not provide a physical interpretation of the impact of the higher symmetries in a periodic structure. Instead, the simplicity of circuit-based modeling methods can lead to a better physical explanation of glide-symmetry effects. For this reason, this approach was chosen in [35] and [30] for simpler 1-D glide and twist configurations, respectively. Specifically, the structure analyzed in [35] consists of two glide-symmetric corrugated structures. Under the assumption that each corrugation can be replaced by Marcuvitz's closed form equivalent circuit [36], it

was easily shown that the glide symmetry effect is equivalent to simply halving the spatial period of the waveguide and removing the glide symmetry. [37] discusses reduced representations of several kinds of higher-symmetric periodic lines proposed in [38]. It demonstrates that a more correct condition for this equivalence would be neglecting the interactions due to localized excitation of higher-order waveguide modes.

2.5 Content of the thesis

In summary, the interesting characteristics of higher symmetries in periodic structures have led to a large number of recent applications in microwave and millimeter-wave devices. This recent interest together with the large impact of symmetric configurations on different propagation features, is motivating research devoted to understand the fundamental differences between a glide-symmetric structure and its simpler periodic counterpart, obtained by suitably removing the glide symmetry. This can be done by removing the off-shift between the metasurfaces, or by moving the scatterers originally placed on the top surface on the bottom one. It is clear from the results shown in this chapter that these simple operations strongly affect the electromagnetic properties of the resulting structures. This is not a trivial observation: if the two metasurfaces in a glide-symmetric configurations are each one replaced with a homogenized model, the off-shift between them should not have any impact on their behavior. The glide-symmetry effects are clearly not described by usual homogenized models even in well-known metasurfaces (e.g., metallic corrugations).

Furthermore, in order to clearly observe the higher-symmetry properties, the two metasurfaces must be in close proximity so that the interaction among the top and bottom components is enhanced. This strong interaction prevents the use of simple homogenized models available for a single metasurface, as expected. As explained in Sec. 2.4, this close proximity may also be a problem for the efficiency of numerical simulations of these kinds of structures: a very fine meshing is required to correctly describe the field behavior, and different geometrical scales can be involved in the definition of the complete structure. This motivates the development of ad-hoc techniques, particularly adapted to higher-symmetric structures.

Based on these considerations, in Chapter 3 special analysis methods are presented for these structures which can shed light into the reasons behind the specific behaviour of higher symmetries. Such methods could possibly lead to further knowledge about the potentials of such symmetries which in turn may lead to better utilisation of them in novel applications such as in reconfigurable waveguide components. A novel analysis method is discussed, based on the generalization of a Bloch-analysis technique to a multimodal description of the unit cells. A specific formulation is given for periodic structures with higher symmetries. Both the glide- and twist-symmetric cases are analyzed in detail. Despite being recently proposed in this thesis, the method has already been used by several research groups for the study and design of different prototypes.

In the following Chapter 4, this method is used to design a millimeter-wave reconfigurable glide-symmetric waveguide capable to enable or prevent propagation. This is achieved by means of a simple reconfiguration of one geometrical parameter only, controlled by a low-consumption piezoelectric actuator. This technology has potential applications for millimeter-wave switches for the feeding networks of multibeam antennas for 5G communications.

Conclusions and future research works are presented in Chapter 5.

Chapter 3

Multimodal T Matrix Analyses for Cells with Higher Symmetries

In this chapter, we generalize a method to calculate the dispersive properties of periodic structures, the transmission-matrix method. It enforces the Floquet theorem by means of the transmission matrix of a unit cell of the periodic structure. First in Sec. 3.1, we introduce the conventional transmission-matrix method. In Sec. 3.2, we extend this method to a formulation with multiple background modes. This enables us to achieve a higher accuracy when periodic scatterers interact strongly among them. This extended method is also suitable to describe the difference between glide and simple periodic structures. This is shown in Sec. 3.3, where we apply the extended method to glide symmetric structures (along one and two directions) and reformulate this method for such structures. In Sec. 3.4, we reformulate the extended method for twist-symmetric structures.

3.1 Transmission-Matrix Analysis

As explained in Section 2.1, the unit cell of a periodic structure is usually the minimal unity that can be used by means of repeated translations to create the full structure. Different methods can be used to study these unit cells, such as methods of moments, finite-difference time-domain, finite-element methods, mode matching [39, 40, 41, 42, 43, 44]. All of them require enforcing the periodic condition on the electromagnetic fields at the boundary of a cell. The method discussed here is based on a description of the unit cell as a two-port linear network, characterized by a 2×2 matrix (the presentation follows Ch. 8 in [45]).

Fig. 3.1 shows an example of a periodic structure which is a microstrip line that is periodically loaded with stubs. To study periodic structures, one can define a multi-port network for their unit cell and uses its transmission matrix ($\boldsymbol{T}$ matrix) to define the governing dispersion relation. For instance, for a one-dimensional (1-D) periodic structure, we can associate a two-port network to its unit cell as shown in Fig. 3.2. The transmission matrix $\boldsymbol{T}$ of this two-port network is defined as:

$$\begin{bmatrix} V_1 \\ I_1 \end{bmatrix} = \boldsymbol{T} \cdot \begin{bmatrix} V_2 \\ I_2 \end{bmatrix} \tag{3.1}$$

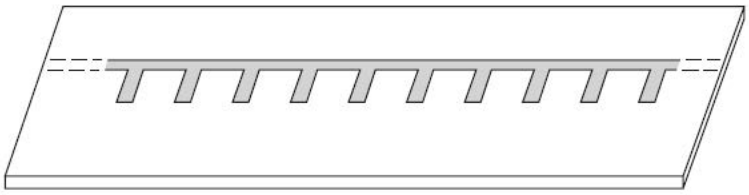

FIGURE 3.1: A portion of an infinite periodic structure: microstrip with periodic stubs [45].

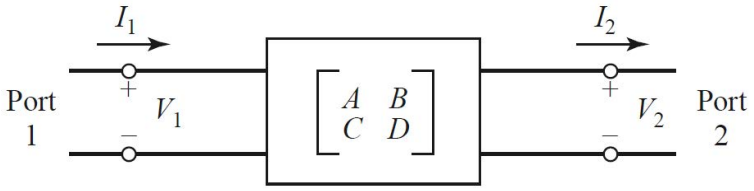

FIGURE 3.2: A two-port network [45].

The Floquet periodicity conditions verified by Bloch modes can be written for the port voltages and currents as:

$$\begin{aligned} V_1 &= \mathrm{e}^{+jk_x p} V_2 \\ I_1 &= \mathrm{e}^{+jk_x p} I_2 \end{aligned} \tag{3.2}$$

where, as it was described in Sec. 2.1.2, k_x is the propagation constant of the existing Bloch modes and it can be written as $k_x = \beta_x - j\alpha_x$ where β_x is the phase constant and α_x is the attenuation constant. Combining these equations with (3.1) gives the following result.

$$\left[\boldsymbol{T} - \mathrm{e}^{+jk_x p}\boldsymbol{I}\right] \begin{bmatrix} V_2 \\ I_2 \end{bmatrix} = 0 \tag{3.3}$$

For a nontrivial solution to this equation, the matrix on the left side must have a zero determinant. Therefore, finding the zeros of the determinant provides the propagation constant k of the Bloch modes. We call this analysis procedure "the T matrix method". Once k is known, the equivalent refractive index of the structure can also be calculated by:

$$n = \frac{\beta}{k_0} \tag{3.4}$$

where β is the phase constant of the Bloch wave and k_0 is the propagation constant of electromagnetic waves in free space.

We now consider the periodic example in Fig. 3.1 to demonstrate the application of this analysis. Often, a transmission line with light periodic discontinuities can be modeled as a line with periodic lumped shunt (or series) reactances embedded into a transmission line. This equivalent circuit is shown in Fig. 3.3. To be able to use the formulations discussed above, we need the T matrix of the unit cell. In the simple case of this equivalent circuit,

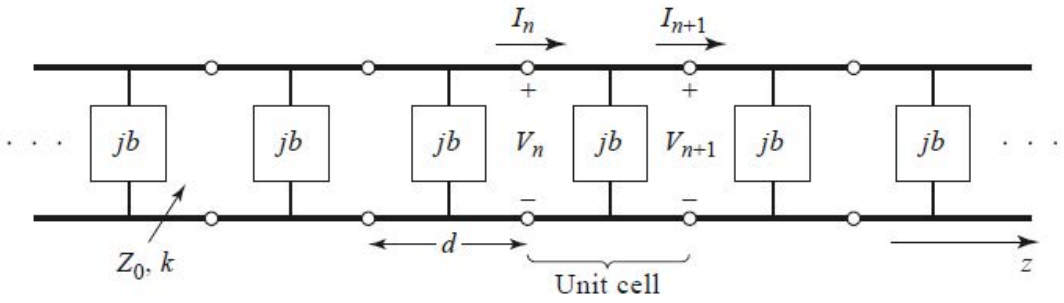

FIGURE 3.3: Equivalent circuit of a periodically loaded transmission line. The unloaded line has characteristic impedance Z_0 and propagation constant k [45].

we know the T matrix of a transmission line and that of a shunt susceptance. We also know that the total transmission matrix of N cascaded networks can be determined as the product of the T matrices of all N networks. Therefore, the T matrix of the unit cell simplifies to a cascade of a transmission line of length $d/2$, a shunt susceptance b, and another transmission line section of length $d/2$:

$$\begin{aligned} T &= \begin{bmatrix} \cos\left(\frac{k_0 d}{2}\right) & j\sin\left(\frac{k_0 d}{2}\right) \\ j\sin\left(\frac{k_0 d}{2}\right) & \cos\left(\frac{k_0 d}{2}\right) \end{bmatrix} \begin{bmatrix} 1 & 0 \\ jb & 1 \end{bmatrix} \begin{bmatrix} \cos\left(\frac{k_0 d}{2}\right) & j\sin\left(\frac{k_0 d}{2}\right) \\ j\sin\left(\frac{k_0 d}{2}\right) & \cos\left(\frac{k_0 d}{2}\right) \end{bmatrix} \\ &= \begin{bmatrix} \cos(k_0 d) - \frac{b}{2}\sin(k_0 d) & j\left(\sin(k_0 d) + \frac{b}{2}\cos(k_0 d) - \frac{b}{2}\right) \\ j\left(\sin(k_0 d) + \frac{b}{2}\cos(k_0 d) + \frac{b}{2}\right) & \cos(k_0 d) - \frac{b}{2}\sin(k_0 d) \end{bmatrix} \end{aligned} \tag{3.5}$$

Where k_0 is the propagation constant of the unloaded line. Now the T matrix in (3.5) can be used in (3.3) to find:

$$\cosh kd = \cosh \alpha d \cos \beta d + j \sinh \alpha d \sin \beta d = \cos k_0 d - \frac{b}{2}\sin k_0 d \tag{3.6}$$

In lossless lines, the right hand side is purely real. Therefore, two solutions are possible for this equation. The first solution is when $\alpha = 0$. This corresponds to a non-attenuated propagating wave on the periodic structure and defines the passband of the structure. In this case, (3.6) reduces to:

$$\cos \beta d = \cos k_0 d - \frac{b}{2}\sin k_0 d \tag{3.7}$$

which requires that the module of the right-hand side is smaller than 1. The second case happens when $\alpha \neq 0$ and $\beta = 0, \pi$. For these solutions, the wave is attenuated along the line and does not propagate. This corresponds to a stopband. The attenuation constant α can then be calculated from:

$$\cosh \alpha d = \left|\cos k_0 d - \frac{b}{2}\sin k_0 d\right| \tag{3.8}$$

These results demonstrate how application of this theory provides information both on the propagation and the attenuation of the waves in passband and stopband frequencies. In the next section, we will extend the transmission matrix to higher-order transmission matrices for our analyses. However, we will still use the term "T matrix method" for brevity. It will be shown that the procedure used here is a special case of the more general procedure presented in the next section.

3.2 Extension of the T Matrix Analysis

The basic T matrix method was introduced in Sec. 3.1. For solution purposes, the T matrix of each unit cell can be easily calculated from the scattering matrix (S matrix). To obtain the S matrix of each cell, a waveguide-port excitation is applied at each side of the unit cell in which only the dominant mode is excited for these measurements. However, we aim here at extending this theory to the case of N excited modes and we will show that this will increase the accuracy of the results. Such method has been used for different analysis and modeling purposes [46, 47, 48, 49]. We will demonstrate that the extension to multiple modes is in fact necessary for the analysis of some classes of periodic structures, and namely for many higher-symmetric structures.

3.2.1 Multimodal T Matrix

The monomodal T matrix of a 1-D periodic structure was defined for its unit cell in (3.1). The multimodal T matrix is a transmission matrix which considers multiple modes as sources instead of only one and relates among them the equivalent voltages and currents of these modes at the boundaries of the unit cell. Both 1-D and 2-D cases are defined in the next subsections.

In the following studies, we calculate the T matrix of a unit cell from its impedance matrix $\mathbf{Z}$, which can be computed with a full-wave method simulating one single unit cell excited with suitable waveguide ports. In our case we use the CST Microwave Studio frequency solver, which calculates the impedance parameters from the scattering parameters automatically by means of a post processing algorithm. We now explain how the T matrix can be computed from the Z matrix. If we consider N modes on each periodic boundary, the unit cell of a 1-D periodic structure having two opposite periodic boundaries has $2N$ voltages and $2N$ currents. For a 2-D periodic structure, having four periodic boundaries, this will correspond to $4N$ voltages and $4N$ currents. In both cases, the total number of voltages or currents are even. Therefore, let's imagine that the total number of equivalent voltages or

currents are $2N$. The Z matrix relates the voltages to the currents:

$$\begin{bmatrix} V_1 \\ V_2 \\ \vdots \\ V_{2N} \end{bmatrix} = \boldsymbol{Z} \cdot \begin{bmatrix} I_1 \\ I_2 \\ \vdots \\ I_{2N} \end{bmatrix} \tag{3.9}$$
$$\text{where} \quad \boldsymbol{Z} = \begin{bmatrix} \underline{\boldsymbol{Z}}_{\boldsymbol{aa}} & \underline{\boldsymbol{Z}}_{\boldsymbol{ab}} \\ \underline{\boldsymbol{Z}}_{\boldsymbol{ba}} & \underline{\boldsymbol{Z}}_{\boldsymbol{bb}} \end{bmatrix}$$

Let's assume that we have numbered the voltages and currents in such a way that the first N voltages and N currents correspond to input ports and the rest of the currents and voltages correspond to output ports. Remembering that the T matrix relates the voltages and the currents on the output port to the input port, we divide (3.9) into the following two equations:

$$\begin{bmatrix} V_1 \\ V_2 \\ \vdots \\ V_N \end{bmatrix} = \left[\underline{\boldsymbol{Z}}_{\boldsymbol{aa}}\right] \cdot \begin{bmatrix} I_1 \\ I_2 \\ \vdots \\ I_N \end{bmatrix} + \left[\underline{\boldsymbol{Z}}_{\boldsymbol{ab}}\right] \cdot \begin{bmatrix} I_{N+1} \\ I_{N+2} \\ \vdots \\ I_{2N} \end{bmatrix} \tag{3.10}$$

$$\begin{bmatrix} V_{N+1} \\ V_{N+2} \\ \vdots \\ V_{2N} \end{bmatrix} = \left[\underline{\boldsymbol{Z}}_{\boldsymbol{ba}}\right] \cdot \begin{bmatrix} I_1 \\ I_2 \\ \vdots \\ I_N \end{bmatrix} + \left[\underline{\boldsymbol{Z}}_{\boldsymbol{bb}}\right] \cdot \begin{bmatrix} I_{N+1} \\ I_{N+2} \\ \vdots \\ I_{2N} \end{bmatrix} \tag{3.11}$$

Multiplying (3.10) by $\left[\underline{\boldsymbol{Z}}_{\boldsymbol{ab}}\right]^{-1}$ gives:

$$\begin{bmatrix} I_{N+1} \\ I_{N+2} \\ \vdots \\ I_{2N} \end{bmatrix} = \left[\underline{\boldsymbol{Z}}_{\boldsymbol{ab}}\right]^{-1} \begin{bmatrix} V_1 \\ V_2 \\ \vdots \\ V_N \end{bmatrix} - \left[\underline{\boldsymbol{Z}}_{\boldsymbol{ab}}\right]^{-1} \cdot \left[\underline{\boldsymbol{Z}}_{\boldsymbol{aa}}\right] \cdot \begin{bmatrix} I_1 \\ I_2 \\ \vdots \\ I_N \end{bmatrix} \tag{3.12}$$

Inserting (3.12) in (3.11) results in:

$$\begin{bmatrix} V_{N+1} \\ V_{N+2} \\ \vdots \\ V_{2N} \end{bmatrix} = \left[\underline{\boldsymbol{Z}}_{\boldsymbol{bb}}\right] \cdot \left[\underline{\boldsymbol{Z}}_{\boldsymbol{ab}}\right]^{-1} \cdot \begin{bmatrix} V_1 \\ V_2 \\ \vdots \\ V_N \end{bmatrix}$$
$$+ \left(\left[\underline{\boldsymbol{Z}}_{\boldsymbol{ba}}\right] - \left[\underline{\boldsymbol{Z}}_{\boldsymbol{bb}}\right] \left[\underline{\boldsymbol{Z}}_{\boldsymbol{ab}}\right]^{-1} \left[\underline{\boldsymbol{Z}}_{\boldsymbol{aa}}\right] \right) \cdot \begin{bmatrix} I_1 \\ I_2 \\ \vdots \\ I_N \end{bmatrix} \tag{3.13}$$

(3.12) and (3.13) can be merged to achieve the following:

$$\begin{bmatrix} V_{N+1} \\ \vdots \\ V_{2N} \\ -I_{N+1} \\ \vdots \\ -I_{2N} \end{bmatrix} = \begin{bmatrix} [\underline{\boldsymbol{Z}}_{bb}]\,[\underline{\boldsymbol{Z}}_{ab}]^{-1} & [\underline{\boldsymbol{Z}}_{ba}] - [\underline{\boldsymbol{Z}}_{bb}]\,[\underline{\boldsymbol{Z}}_{ab}]^{-1}\,[\underline{\boldsymbol{Z}}_{aa}] \\ -[\underline{\boldsymbol{Z}}_{ab}]^{-1} & [\underline{\boldsymbol{Z}}_{ab}]^{-1}\,[\underline{\boldsymbol{Z}}_{aa}] \end{bmatrix} \cdot \begin{bmatrix} V_1 \\ \vdots \\ V_N \\ I_1 \\ \vdots \\ I_N \end{bmatrix} \tag{3.14}$$

This gives us the definition of the T matrix based on the Z matrix:

$$\boldsymbol{T} = \begin{bmatrix} [\underline{\boldsymbol{Z}}_{bb}]\,[\underline{\boldsymbol{Z}}_{ab}]^{-1} & [\underline{\boldsymbol{Z}}_{ba}] - [\underline{\boldsymbol{Z}}_{bb}]\,[\underline{\boldsymbol{Z}}_{ab}]^{-1}\,[\underline{\boldsymbol{Z}}_{aa}] \\ -[\underline{\boldsymbol{Z}}_{ab}]^{-1} & [\underline{\boldsymbol{Z}}_{ab}]^{-1}\,[\underline{\boldsymbol{Z}}_{aa}] \end{bmatrix} \tag{3.15}$$

In all the following sections, we use (3.15) to obtain the T matrix from the Z matrix that is calculated by CST Microwave Studio.

It is known that in the case of non-TEM excitation modes, the voltage and current definitions and therefore the characteristic impedance are not unique [45]. An important discussion is the uniqueness of the eigensolutions of the T matrix method, which is based on an arbitrary definition of the characteristic impedance, voltage and current of non-TEM background modes. These arbitrary definitions will lead to different transmission matrices and it is important to see how this will affect the eigensolutions. In this regard, it can be easily shown that if the same voltages, currents and hence characteristic impedances are defined on two opposite ports, the eigensolutions are unchanged no matter how these parameters are defined. To prove this claim, we can start by the conversion formula for obtaining the Z matrix based on the scattering matrix $\boldsymbol{S}$ [50]:

$$\boldsymbol{Z} = \sqrt{\boldsymbol{Z_0}}\,(\boldsymbol{I} + \boldsymbol{S})\,(\boldsymbol{I} - \boldsymbol{S})^{-1}\,\sqrt{\boldsymbol{Z_0}} \tag{3.16}$$

$\boldsymbol{I}$ is the $2N \times 2N$ identity matrix and $\sqrt{\boldsymbol{Z_0}}$ is defined as:

$$\sqrt{\boldsymbol{Z_0}} = \begin{bmatrix} \sqrt{\underline{\boldsymbol{Z}}_{\boldsymbol{0_1}}} & \underline{\boldsymbol{0}} \\ \underline{\boldsymbol{0}} & \sqrt{\underline{\boldsymbol{Z}}_{\boldsymbol{0_2}}} \end{bmatrix} \tag{3.17}$$

$\underline{\boldsymbol{0}}$ is the $N \times N$ null matrix and $\sqrt{\underline{Z}_{0_i}}$ corresponds to the ith boundary and is defined as:

$$\sqrt{\underline{Z}_{0_i}} = \begin{bmatrix} \sqrt{Z_{0_i}^{(1)}} & 0 & \cdots & 0 \\ 0 & \sqrt{Z_{0_i}^{(2)}} & \ddots & 0 \\ \vdots & 0 & \ddots & 0 \\ 0 & 0 & 0 & \sqrt{Z_{0_i}^{(N)}} \end{bmatrix} \tag{3.18}$$

$\sqrt{Z_{0_i}^{(j)}}$ is the characteristic impedance of the jth mode on the ith boundary. By defining $\boldsymbol{z}$ as the Z matrix that corresponds to the choice of $\sqrt{Z_{0_i}^{(j)}} = 1$ for all the modes, (3.16) can be reformulated as:

$$\begin{aligned} \boldsymbol{Z} &= \sqrt{\boldsymbol{Z_0}} \cdot \boldsymbol{z} \cdot \sqrt{\boldsymbol{Z_0}} \\ &= \begin{bmatrix} \left[\sqrt{\underline{\boldsymbol{Z}}_{\boldsymbol{0_1}}}\right] \cdot \left[\underline{\boldsymbol{z}}_{\boldsymbol{aa}}\right] \cdot \left[\sqrt{\underline{\boldsymbol{Z}}_{\boldsymbol{0_1}}}\right] & \left[\sqrt{\underline{\boldsymbol{Z}}_{\boldsymbol{0_1}}}\right] \cdot \left[\underline{\boldsymbol{z}}_{\boldsymbol{ab}}\right] \cdot \left[\sqrt{\underline{\boldsymbol{Z}}_{\boldsymbol{0_2}}}\right] \\ \left[\sqrt{\underline{\boldsymbol{Z}}_{\boldsymbol{0_2}}}\right] \cdot \left[\underline{\boldsymbol{z}}_{\boldsymbol{ba}}\right] \cdot \left[\sqrt{\underline{\boldsymbol{Z}}_{\boldsymbol{0_1}}}\right] & \left[\sqrt{\underline{\boldsymbol{Z}}_{\boldsymbol{0_2}}}\right] \cdot \left[\underline{\boldsymbol{z}}_{\boldsymbol{bb}}\right] \cdot \left[\sqrt{\underline{\boldsymbol{Z}}_{\boldsymbol{0_2}}}\right] \end{bmatrix} \end{aligned} \tag{3.19}$$

It can be shown that inserting the sub-matrices of the Z matrix from (3.19) in (3.15) results in the following equation:

$$\boldsymbol{T} = \begin{bmatrix} \sqrt{\underline{\boldsymbol{Z}}_{\boldsymbol{0_2}}} & \underline{\boldsymbol{0}} \\ \underline{\boldsymbol{0}} & \sqrt{\underline{\boldsymbol{Z}}_{\boldsymbol{0_2}}}^{-1} \end{bmatrix} \cdot \boldsymbol{t} \cdot \begin{bmatrix} \sqrt{\underline{\boldsymbol{Z}}_{\boldsymbol{0_1}}}^{-1} & \underline{\boldsymbol{0}} \\ \underline{\boldsymbol{0}} & \sqrt{\underline{\boldsymbol{Z}}_{\boldsymbol{0_1}}} \end{bmatrix} \tag{3.20}$$

where $\boldsymbol{t}$ is the normalized T matrix which corresponds to the normalized Z matrix $\boldsymbol{z}$. If $\sqrt{Z_{0_1}^{(j)}} = \sqrt{Z_{0_2}^{(j)}}$ for all modes j, then the relation $\sqrt{\underline{\boldsymbol{Z}}_{\boldsymbol{0_1}}} = \sqrt{\underline{\boldsymbol{Z}}_{\boldsymbol{0_2}}}$ holds. In this case, according to (3.20) the matrices $\boldsymbol{T}$ and $\boldsymbol{t}$ are similar and hence share the same eigenvalues.

3.2.2 Analysis of 1-D Periodic Structures

Let's imagine a 1-D periodic structure with period p along the x direction. Again, we can use the Floquet boundary conditions for the two sides of the unit cell that are faced along the $+x$ and $-x$ directions. However, this time, instead of one set of voltage and current for each side, we consider N sets. These sets can be attributed to N different excitation modes that will be applied at the two sides of the unit cell. The unit cell can therefore be modelled by a $2N$-port network with N input ports and N output ports. We define a multimodal transmission matrix $\boldsymbol{T}$ as follows:

$$\begin{bmatrix} \boldsymbol{V_1} \\ \boldsymbol{I_1} \end{bmatrix} = \boldsymbol{T} \cdot \begin{bmatrix} \boldsymbol{V_2} \\ \boldsymbol{I_2} \end{bmatrix}$$

$$\text{where} \quad \boldsymbol{V_i} = \begin{pmatrix} V_i^{(1)} \\ V_i^{(2)} \\ \vdots \\ V_i^{(N)} \end{pmatrix} \quad \text{and} \quad \boldsymbol{I_i} = \begin{pmatrix} I_i^{(1)} \\ I_i^{(2)} \\ \vdots \\ I_i^{(N)} \end{pmatrix} \tag{3.21}$$

$V_i^{(n)}$ and $I_i^{(n)}$ are the voltage and current on side i of the unit cell due to the nth excitation mode. Therefore, $\boldsymbol{V_i}$ and $\boldsymbol{I_i}$ are column vectors containing respectively the voltages and currents corresponding to the N modes. Again, in order to solve for the dispersion relation, we apply the Floquet conditions at the boundaries of the unit cell as it was done in Sec. 3.1. The Floquet

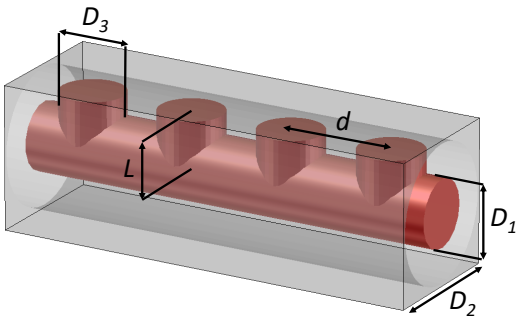

FIGURE 3.4: A coaxial cable loaded with periodic pins.

conditions will be expressed as:

$$\begin{bmatrix} \boldsymbol{V}_1 \\ \boldsymbol{I}_1 \end{bmatrix} = \mathrm{e}^{+jk_x p} \begin{bmatrix} \boldsymbol{V}_2 \\ \boldsymbol{I}_2 \end{bmatrix} \tag{3.22}$$

Applying (3.22) to (3.21) gives the eigenvalue problem in (3.23). The solution of this equation provides the dispersion results of the structure under study.

$$\left[\boldsymbol{T} - \mathrm{e}^{+jk_x p} \boldsymbol{I} \right] \begin{bmatrix} \boldsymbol{V_2} \\ \boldsymbol{I_2} \end{bmatrix} = 0 \tag{3.23}$$

Finding the zeros of the determinant of the left hand side's matrix provides the propagation constants of the Bloch waves. To put the formulation to test, we apply it to the 1-D periodic structure shown in Fig. 3.4. The structure is a coaxial cable that is periodically loaded with circular pins. Fig. 3.5 depicts the dispersion diagram of this structure when the parameters are $D_1 = 2.4$ mm, $D_2 = 4.84$ mm,$D_3 = 2.2$ mm, $L = 2$ mm and $d = 5$ mm. It is observed from the figure that using a single mode ($N = 1$) gives incorrect results for the dispersion diagram while using $N \geq 2$ modes ($N = 3$ and $N = 4$ modes are shown in the figure) results in the correct solution which matches the solution provided by the CST eigensolver. This example stresses why the extended T matrix formulation presented in this section should be preferred to the conventional formulation with $N = 1$ mode that was covered in Sec. 3.1. As we progress through this chapter, we provide more examples where the conventional formulation falls short in solving the problem.

3.2.3 Analysis of 2-D Periodic Structures

Let's imagine that we want to study a structure that is 2-D periodic with periods p_x and p_y in x and y directions respectively. An example is given in Fig. 3.6 (a). The unit cell is bound in the area $0 < x < p_x$ and $0 < y < p_y$ (shown in Fig. 3.6 (b)). In this case, our unit cell would have 2 faces along the x axis (namely, $x = 0$ and $x = p_x$) and 2 faces along the y axis ($y = 0$ and $y = p_y$). We number these 4 faces in the following way: The $x = 0$ face is numbered 1 and the $y = 0$ face is numbered 2. $x = p_x$ and $y = p_y$ are each numbered 3 and 4 respectively. Now, we can define the $\boldsymbol{T}$ matrix

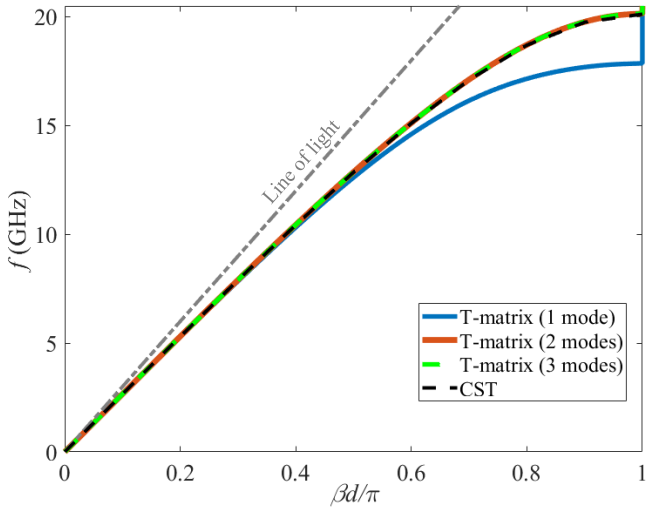

FIGURE 3.5: Normalized phase constant $\beta d/\pi$ versus frequency for the structure given in Fig. 3.4.

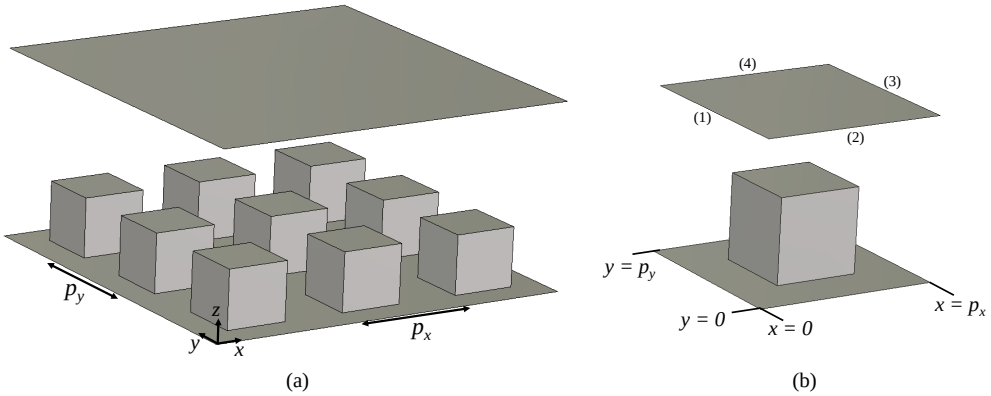

FIGURE 3.6: Parallel plates where the bottom plate is periodically loaded with rectangular pins: (a) part of the structure (b) the unit cell.

and the Floquet conditions according to these 4 boundary faces. Considering N modes on each of these faces makes the unit cell equivalent to a $4N$-port network. Therefore, we define the $\boldsymbol{T}$ matrix:

$$\begin{bmatrix} \boldsymbol{V}_1 \\ \boldsymbol{V}_2 \\ \boldsymbol{I}_1 \\ \boldsymbol{I}_2 \end{bmatrix} = \boldsymbol{T} \cdot \begin{bmatrix} \boldsymbol{V}_3 \\ \boldsymbol{V}_4 \\ \boldsymbol{I}_3 \\ \boldsymbol{I}_4 \end{bmatrix} \tag{3.24}$$

where $\boldsymbol{V_i}$ and $\boldsymbol{I_i}$ $(i = 1, 2, 3, 4)$ are voltage vectors and current vectors as defined in (3.21). The Floquet conditions are:

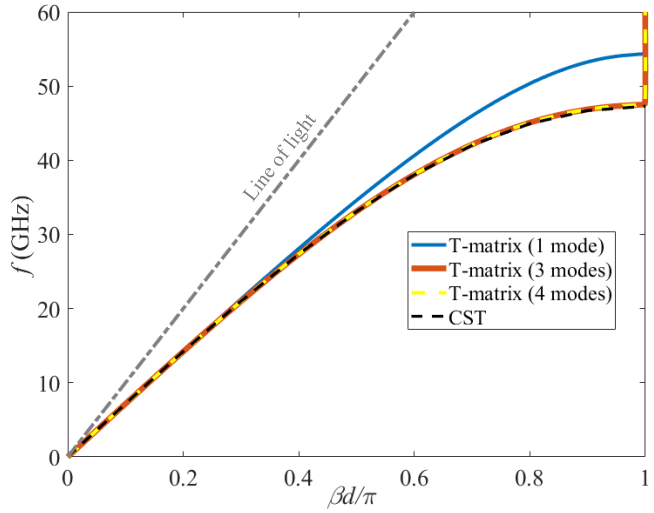

FIGURE 3.7: Dispersion diagram of the 2-D periodic structure in Fig. 3.6

$$\begin{bmatrix} \boldsymbol{V}_1 \\ \boldsymbol{V}_2 \\ \boldsymbol{I}_1 \\ \boldsymbol{I}_2 \end{bmatrix} = \begin{bmatrix} e^{+jk_x p_x}\boldsymbol{V}_3 \\ e^{+jk_y p_y}\boldsymbol{V}_4 \\ e^{+jk_x p_x}\boldsymbol{I}_3 \\ e^{+jk_y p_y}\boldsymbol{I}_4 \end{bmatrix} \tag{3.25}$$

Combining (3.24) and (3.25) provides the following eigenvalue problem:

$$\left[\boldsymbol{T} - \begin{pmatrix} e^{+jk_x p_x} & 0 & 0 & 0 \\ 0 & e^{+jk_y p_y} & 0 & 0 \\ 0 & 0 & e^{+jk_x p_x} & 0 \\ 0 & 0 & 0 & e^{+jk_y p_y} \end{pmatrix} \boldsymbol{I} \right] \begin{bmatrix} \boldsymbol{V_3} \\ \boldsymbol{V_4} \\ \boldsymbol{I_3} \\ \boldsymbol{I_4} \end{bmatrix} = 0 \tag{3.26}$$

Again, we look for the zeros of the determinant of the left hand-side matrix. Fig. 3.7 plots the dispersion diagram of the structure shown in Fig. 3.6 for propagation in the x direction ($k_y = 0$, $k_x \neq 0$) where $p_x = p_y = d$. The results from the extended T matrix formulations are compared to the result from the CST eigensolver. The results show that also in this case a single $N = 1$ mode is not sufficient to achieve convergence to the CST results. A minimum of $N \geq 3$ modes are needed for that matter. It can be observed in the figure that the results with $N = 3$ and $N = 4$ modes agree with the result from CST. Once again, it was important to consider the higher-order modes to increase the accuracy of the results. In the next sections, we apply this method to periodic structures with higher symmetries.

3.3 Glide Symmetric Structures

This section aims to use the eigenvalue problems in (3.23) and (3.26) to extract the dispersive relations of 1-D and 2-D glide-symmetric structures. The

transmission matrix in these equations is calculated through the procedure discussed in Sec. 3.2.1: First, the impedance matrix is calculated by CST Microwave Studio. Then this matrix is converted to the transmission matrix T using (3.15). We will compare the dispersion results of our proposed Bloch mode analysis with the results directly obtained from the eigensolver analysis of the CST Microwave Studio. This will validate our proposed method by verifying its accuracy. It is good to note that the imaginary part of the wavenumber cannot be compared to the CST eigensolver results as the latter software does not compute this quantity.

3.3.1 Glide Symmetry Along One Direction

Periodic-structure associated to a glide structure

Fig. 3.8 shows a 1-D glide-symmetric structure composed of two corrugated metallic surfaces off-shifted of half a period with respect to each other. For simplicity, the structure is assumed invariant along the y direction. We remind the reader that this structure is invariant under the 1-D glide symmetry operator and the 1-D translation operator given in (2.16) and (2.1) respectively.

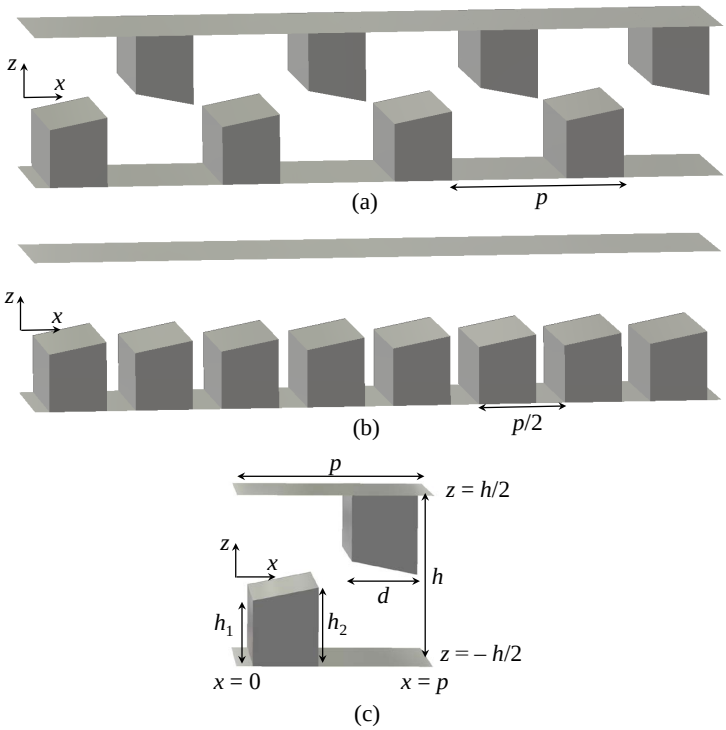

FIGURE 3.8: (a) 1-D glide-symmetric line whose period is p. (b) Non-glide symmetric periodic line obtained by moving the top metals to the bottom plate. Its period is $p/2$. (c) Unit cell of the glide-symmetric structure.

Before we apply the transmission matrix method developed in Sec. 3.1, we would like to discuss another structure which will help us gain some

physical insights into the higher order mode interactions at the unit cell level. Fig. 3.8 (b) is a periodic non-glide symmetric structure with period $p/2$. This structure was obtained by mirroring the upper corrugations in the glide-symmetric structure shown in Fig. 3.8 and moving them from the top plate to the bottom. We will calculate the dispersion diagrams of both of the structures given in Fig. 3.8 (a) and (b). We will refer to them as the glide-symmetric and the non-glide symmetric structure. We will show that the comparison of these structures will provide useful information on the effect of the glide symmetry in periodic structures.

[35] has discussed the equivalence between the structures of Fig. 3.8 (a) and Fig. 3.8 (b) based on the validity of an equivalent circuit proposed there. This equivalent circuit neglects the higher-order modes at the two borders of the unit cell. Therefore, it corresponds to the formulation given in Sec. 3.2.2 with $N = 1$, where only one mode is retained on each unit cell's face. This assumption is shown to be valid as long as $d > p/2$ [35]. In this sub-section, we use this observation to class glide-symmetric structures in two newly-defined kinds, namely *reducible* and *irreducible* structures. We will show that this classification is related to the nature of the modal interaction between adjacent cells.

Reducible and irreducible glide-symmetric structures

We define a reducible glide-symmetric structure as a structure where the mirroring operation of the glide operator does not have an impact on the dispersion diagram. For instance, a reducible line as in Fig. 3.8 (a) has the same dispersion relation as the structure in fig 3.8 (b) with the same parameter values. Conversely, we define an irreducible glide-symmetric structure as a structure where the mirroring operation does have an impact, so that an irreducible line with the shape of Fig. 3.8 (a) exhibits a different dispersion relation from the structure in Fig. 3.8 (b). It will be shown that the same geometry can be classified as a reducible or an irreducible structure according to the values of its geometrical parameters and the frequency range of interest. Using the T-matrix analysis, we aim at demonstrating that the difference between reducible and irreducible structures lies in the impact of higher-order modes on each unit-cell boundary. Reducible structures require only one mode at each face, whereas irreducible lines need higher-order modes at each face to compute the dispersion diagram correctly.

The unit cell of the glide-symmetric line is depicted in Fig. 3.8 (c). First, let us consider the structures in Fig. 3.8 (a) and (b) with geometrical parameters of $p = 3$ mm, $d = 0.25$ mm, $h_1 = 0.35$ mm, $h_2 = 0.45$ mm and $h = 1$ mm. Their dispersion diagrams are plotted in Fig. 3.9. Firstly, the results computed with the CST eigensolver are plotted and compared with each other in Fig. 3.9 (a). One can easily notice that the glide and the non-glide structures have the same dispersion diagram. This corresponds to a reducible glide symmetry. In Fig. 3.9, we plot the diagrams obtained with the T-matrix method. 1,2 and 3 modes were used and their dispersion diagrams were plotted. It is clear that using higher-order port modes does not change the

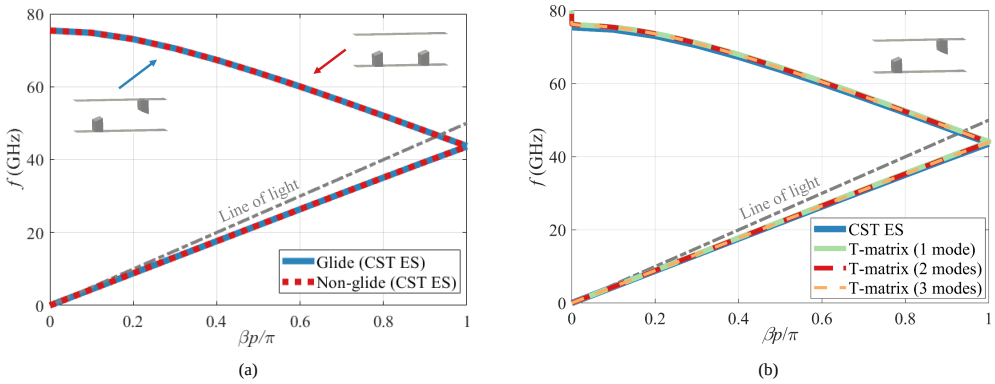

FIGURE 3.9: Dispersion diagram of the structures in Fig. 3.8 (a) and (b) with geometrical parameter: $p = 3$ mm, $d = 0.25$ mm, $h_1 = 0.35$ mm, $h_2 = 0.45$ mm and $h = 1$ mm.

results as the first mode is already enough to reach the accurate dispersion diagram.

To present an example of an irreducible line, a change of the parameters should be enforced. Let us consider again the same structure of Fig. 3.8 (a) with its corresponding non-glide symmetric line of Fig. 3.8 (b). We choose the parameters as $p = 1.5$ mm, $d = 0.5$ mm, $h_1 = 0.35$ mm, $h_2 = 0.45$ mm and $h = 1$ mm. This structure has a shorter period and a wider corrugation compared to the previous example. This means that the corrugations are now tightly adjacent to each other. We expect the proximity of these scatterers to form an irreducible line. Fig. 3.10 (a) uses the CST eigensolver to sketch the dispersion diagram of the glide-symmetric structure and its non-glide symmetric counterpart with halved period. Unlike the reducible line example discussed above, the dispersion diagrams for these structures are completely different. A tight adjacency of the scatterers in the glide-symmetric topology produces a dispersion response which is quite different from the non-glide symmetric counterpart. To validate our T-matrix method for irreducible structures, we plotted in Fig. 3.10 (b) the results that are obtained with this method using multiple modes. Investigation of these curves demonstrates that inclusion of just one waveguide mode provides the wrong dispersion diagram with an incorrect stop-band at mid-frequencies. In opposition, adding a second mode leads to the correct dispersion diagram. The result with $N = 3$ modes have also been plotted: it exactly matches the curve with $N = 2$ modes and demonstrates the convergence of the results. This confirms that the mirrored nature of half-cells in glide symmetries treats modes with different types of symmetry differently. It also emphasizes the need to use the multimodal transmission matrix to obtain more accurate results. In the next section, we use this observation to suggest a modified analysis that uses the higher symmetry to obtain the dispersion relation from half of a unit cell.

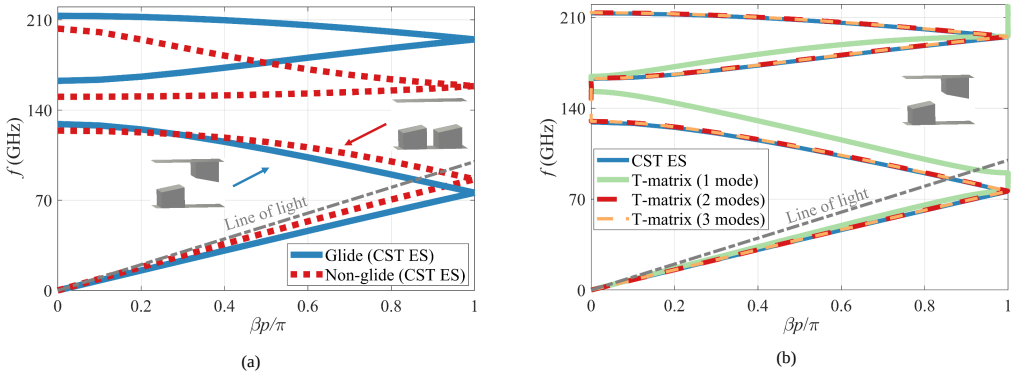

FIGURE 3.10: Dispersion diagram of the structures in Fig. 3.8 (a) and (b) with parameter values: $p = 1.5$ mm, $d = 0.5$ mm, $h_1 = 0.35$ mm, $h_2 = 0.45$ mm and $h = 1$ mm.

3.3.2 1-D Glide-Symmetric Boundary Conditions Along One Direction

In this section, we exploit glide symmetry in order to limit the computational domain to a sub-region of the entire unit cell. A generalized Floquet theorem discussed in [2] shows that the study of a glide-symmetric line can be limited to half of its unit cell (the region $0 < x < p/2$ in Fig. 3.8 (c)) by formulating the following eigenvalue problem associated to the glide operator:

$$G_{p\hat{\boldsymbol{x}}}\left[\boldsymbol{E}\left(x,z\right)\right] = \boldsymbol{E}\left(x+p/2,-z\right) = e^{-jk_x p/2}\boldsymbol{E}\left(x,z\right) \tag{3.27}$$

This means that the field measured after a translation of half a period and a mirroring with respect to the glide plane is a scalar multiple of the field at the initial position. It is evident from (3.27) that two consecutive $G_{p\hat{\boldsymbol{x}}}$ operations give the eigenvalue problem in (3.23). It is important to remark that a minus sign could be added to the last term of (3.27): this will still be consistent with (3.23). When a $-$ sign is added, the k_x wavenumber is transformed into the $k_x' = k_x + 2\pi/p$ wavenumber which is a harmonic of the same Bloch mode [33]. For this reason, the $+$ sign will be retained here without loss of generality.

We want to formulate the glide eigenvalue problem for a sub-region of the unit cell by means of a multimodal transmission matrix that we defined earlier in Sec. 3.2.2. To this aim, we define the multimodal transmission matrix $\underline{\boldsymbol{T}}_{1/2}$ associated to one half of a unit cell ($0 < x < p/2$ in Fig. 3.8 (c)). This transmission matrix performs a translation along the line from $x = 0$ to $x = p$. However, the glide operator in (3.27) consists of a translation and a mirroring. To overcome this issue, we write the translation operator $T_{\frac{p}{2}\hat{\boldsymbol{x}}}$ in terms of the the glide operator $G_{p\hat{\boldsymbol{x}}}$. We will show that this results in an eigenvalue problem for the transmission matrix $\underline{\boldsymbol{T}}_{1/2}$. Before writing the relation between the translation operator and the glide operator, we define the mirror operator $M_{\hat{\boldsymbol{z}}}$ as:

$$M_{\hat{z}}\left[\boldsymbol{E}\left(x,z\right)\right]=\boldsymbol{E}\left(x,-z\right) \tag{3.28}$$

We can express the translation operator $T_{\frac{p}{2}\hat{\boldsymbol{x}}}$ as a composition of the glide operator $G_{p\hat{\boldsymbol{x}}}$ and a mirroring operator:

$$T_{\frac{p}{2}\hat{\boldsymbol{x}}}\left[\boldsymbol{E}\left(x,z\right)\right]=M_{\hat{z}}G_{p\hat{\boldsymbol{x}}}\left[\boldsymbol{E}\left(x,z\right)\right]=e^{-jk_xp/2}M_{\hat{z}}\left[\boldsymbol{E}\left(x,z\right)\right] \tag{3.29}$$

In order to proceed, we need to convert this equation to a matrix form. By considering each Bloch mode as a composition of the background modes defined at the geometrical ports of the half cell, the translation operator $T_{\frac{p}{2}\hat{\boldsymbol{x}}}$ corresponds to the multi-modal transmission matrix $\underline{\boldsymbol{T}}_{1/2}$. To obtain the matrix equivalent of the mirroring operator, we need to understand the effect of mirroring on the background modes. Each mode is either odd or even with respect to the mirroring plane ($z=0$) and it is here named $\boldsymbol{E}^{\text{even}}$ and $\boldsymbol{E}^{\text{odd}}$ respectively. Here, we considered the z components of modal electric fields (e_z), used to define equivalent voltages at each port. However, due to the bi-dimensional nature of the problem, the same symmetry holds for the x components of the modal magnetic fields, which define equivalent currents. For both of these components, the mirror operation reduces to ±1 multiplication factor, according to the mode parity. The mirror is expressed as:

$$\begin{cases} M_{\hat{z}}\left[e_z^{\text{even}}(x,-z)\right] &= \quad e_z^{\text{even}}(x,z) \\ M_{\hat{z}}\left[e_z^{\text{odd}}(x,-z)\right] &= -\ e_z^{\text{odd}}(x,z) \end{cases} \tag{3.30}$$

The conditions in (3.29) and (3.30) lead to the following eigenvalue problem for the half-cell:

$$\underline{\boldsymbol{T}}_{1/2}\cdot\begin{bmatrix}\boldsymbol{V}_1\\ \boldsymbol{I}_1\end{bmatrix}=e^{-jk_xp/2}\begin{bmatrix}\underline{\boldsymbol{Q}} & \underline{\boldsymbol{0}}\\ \underline{\boldsymbol{0}} & \underline{\boldsymbol{Q}}\end{bmatrix}\cdot\begin{bmatrix}\boldsymbol{V}_1\\ \boldsymbol{I}_1\end{bmatrix} \tag{3.31}$$

where $\underline{\boldsymbol{0}}$ is the $N\times N$ null matrix and $\underline{\boldsymbol{Q}}$ is a sign matrix that corresponds to the mirror operation. It is a diagonal matrix defined as:

$$\underline{\boldsymbol{Q}}=\begin{bmatrix} q^{(1)} & 0 & \cdots & 0\\ 0 & q^{(2)} & \ddots & \vdots\\ \vdots & \ddots & \ddots & 0\\ 0 & \cdots & 0 & q^{(N)}\end{bmatrix} \tag{3.32}$$

$$\text{where}\quad q^{(i)}=\begin{cases}+1 & \text{mode } i \text{ has even symmetry}\\ -1 & \text{mode } i \text{ has odd symmetry}\end{cases}$$

For example, in a simple case where only two modes with different parity are retained, (3.31) reads as

$$\underline{\boldsymbol{T}}_{1/2} \cdot \begin{bmatrix} V_1^{(1)} \\ V_1^{(2)} \\ I_1^{(1)} \\ I_1^{(2)} \end{bmatrix} = e^{-jk_x p/2} \begin{bmatrix} V_1^{(1)} \\ -V_1^{(2)} \\ I_1^{(1)} \\ -I_1^{(2)} \end{bmatrix} \tag{3.33}$$

With this equation, the dispersion relation of a glide-symmetric structure is solved by considering the network parameters (namely, the transmission matrix) of only half of its unit cell. On one hand, from (3.31) and (3.33), it is clear that in reducible lines, where only one mode is retained, the glide-symmetric problem is equivalent to a periodic problem whose period is divided by two ($p/2$ instead of p). On the other hand, in irreducible lines, the presence of higher-order modes with different parity along the mirroring direction is responsible for a different interaction between elements with respect to the non-glide periodic line.

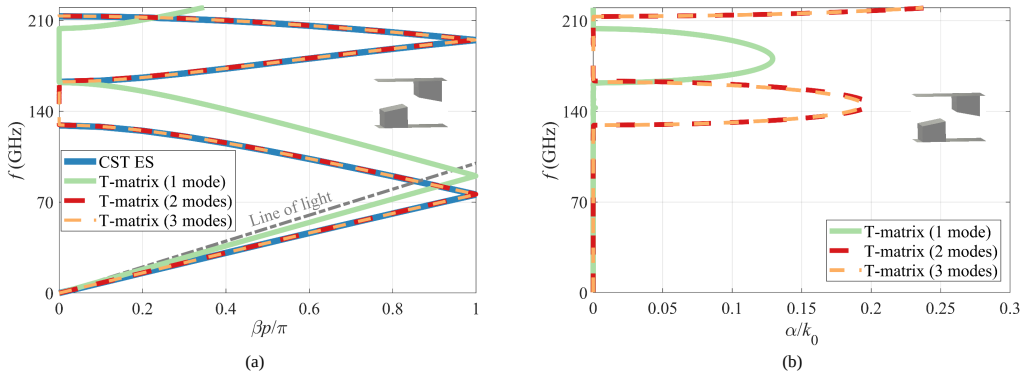

FIGURE 3.11: Dispersion diagram of the glide-symmetric structure in Fig. 3.8 (a) obtained from the simulation of half of a cell with N modes on each geometrical face. Geometrical parameters: $p = 1.5$ mm, $d = 1$ mm, $h_1 = 0.45$ mm, $h_2 = 0.55$ mm and $h = 1$ mm. $N = 1$ mode (*dotted blue line*), $N = 2$ modes (*solid red line*), $N = 3$ modes (*dashed green line*). (a) Normalized phase constant $\beta p/\pi$ vs. frequency. CST comparison (*solid thin line*), line of light *dashed dotted gray line*. (b) Normalized attenuation constant α/k_0 vs. frequency.

To put the formulation to test, we apply (3.31) to the example of the irreducible glide-symmetric line studied in the previous section. Fig. 3.11 depicts the results using the half-cell formulations. In Fig. 3.11 (a), the phase constant β from the half-cell transmission matrix is compared to the solution provided by the CST eigensolver. Again three cases of $N = 1$, $N = 2$ and $N = 3$ modes are considered. It is easy to notice that the dispersion diagram was fully predicted for $N = 2$ and $N = 3$ modes and that consideration of a single mode ($N = 1$) is not enough for proper modeling of the periodic structure. Like the full-cell configuration, the perfect agreement between the results obtained with 2 and 3 modes at each face validates the convergence of the solution. Fig. 3.11 (b) plots the normalized attenuation constant of the

propagating Bloch wave (α/k_0) with respect to frequency. Similar conclusions are made with this plot, namely, the convergence of the method and the necessity of considering multiple modes. In Fig. 3.11 (b), there is no comparison with CST results. This is due to the inability of the CST eigensolver method to calculate α. The calculation of the imaginary part (α) in addition to the real part (β) of the wavenumber is one of the advantages of the T-matrix method.

3.3.3 Glide Symmetry Along Two Directions

In this section, the T-matrix analysis of 2-D periodic structures that were discussed in Sec. 3.2.3 is applied to 2-D configurations exhibiting glide symmetry. Similar to the 1-D case, 2-D glide boundary conditions are introduced to be used on a sub-region of each unit cell. Then, the eigenvalue problem for this sub-region is presented. In this section's formulations, the two axes of periodicity are assumed orthogonal, but the formulation of the problems and all the results hold in the case of general skewed axes.

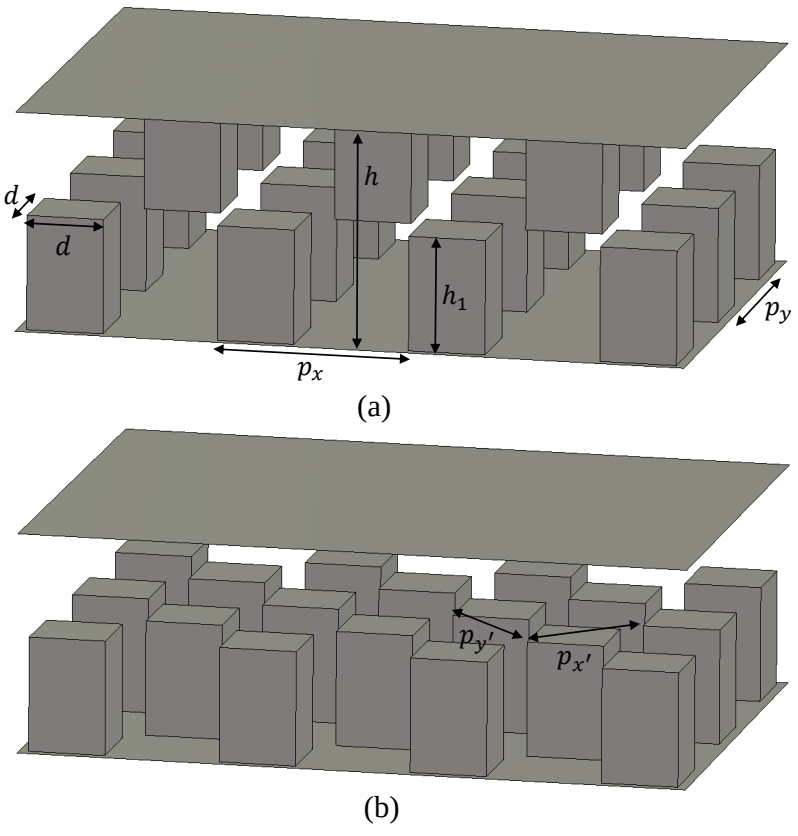

FIGURE 3.12: (a) 2-D glide-symmetric surfaces whose periods are p_x and p_y. (b) Non-glide symmetric periodic surfaces obtained by moving the top pins to the bottom plate. If $p_x = p_y$ its periods along the rotated axes are $p_{x'} = p_x/\sqrt{2}$ and $p_{y'} = p_y/\sqrt{2}$.

Fig. 3.12 (a) shows a 2-D glide-symmetric structure. Similar to a 1-D glide-symmetric structure, the 2-D version is invariant with respect to the glide symmetry operator. The 2-D glide symmetry operator $G_{p_x\hat{\boldsymbol{x}},p_y\hat{\boldsymbol{y}}}$ for a periodic structure with periods p_x in x and p_y in y direction, was defined in (2.17).

In a similar approach to the one we used for 1-D structures, a non glide-symmetric periodic structure in Fig 3.12 (b) can be obtained from the glide-symmetric structure in Fig. 3.12 (a) by mirroring the upper pins and moving them from the top to the bottom plate. If $p_x = p_y$, this transformation yields a periodic structure whose periods are $p/\sqrt{2}$ along the 45° rotated x', y' axes. If $p_x \neq p_y$, the formulation still applies, but a different rotation is required and different period values are obtained. The glide-symmetric unit cell is shown in Fig. 3.13, where black and white rectangles represent bottom and top vertical pins.

The eigenvalue condition in a 2-D periodic structure as Fig 3.12 (a) is:

$$\begin{aligned} T_{mp_x\hat{\boldsymbol{x}}}T_{np_y\hat{\boldsymbol{y}}}\left[\boldsymbol{E}\left(x,y,z\right)\right] &= \boldsymbol{E}\left(x+mp_x,y+np_y,z\right) \\ &= e^{-j\left(mk_xp_x+nk_yp_y\right)}\boldsymbol{E}\left(x,y,z\right) \end{aligned} \tag{3.34}$$

m, n being arbitrary integers. The choice of $m = 0, n = 1$ and $m = 1, n = 0$ enforces two independent conditions covering the full boundaries of a single minimal unit cell shown in Fig. 3.13 (in solid line):

$$\begin{aligned} \boldsymbol{E}\left(x+p_x,y,z\right) &= e^{-jk_xp_x}\boldsymbol{E}\left(x,y,z\right) \\ \boldsymbol{E}\left(x,y+p_y,z\right) &= e^{-jk_yp_y}\boldsymbol{E}\left(x,y,z\right) \end{aligned} \tag{3.35}$$

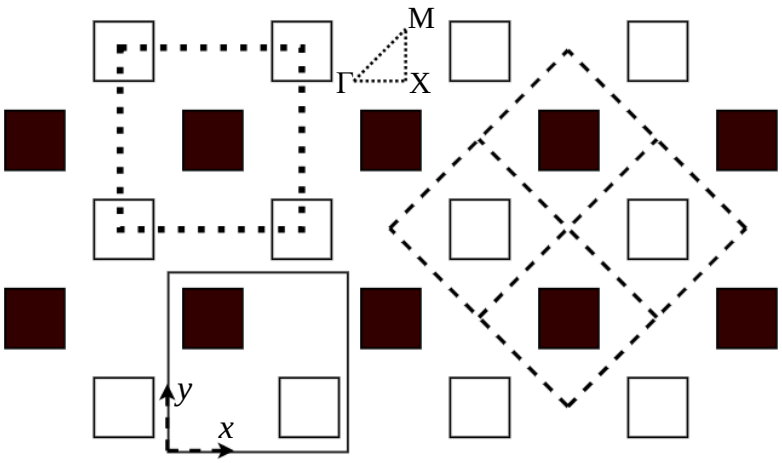

FIGURE 3.13: Top view of the periodic structure in Fig. 3.12 (a). Black and white squares are bottom and top pins, respectively. At the bottom left, the minimal unit cell ($0 < x < p_x, 0 < y < p_y$) used in (3.35) is shown (*solid lines*). The centrally symmetric minimal unit cell is shown at the top left(*dotted lines*). At the right, the non-minimal unit cell and its quarter used in (3.37) are shown (*dashed lines*).

In order to simplify the eigenvalue problem (3.35) and transform it into a finite-dimensional problem, we need to define four geometrical faces of the unit cell, i.e., the four straight boundaries of the unit cell in Fig. 3.13. N modes are attributed to each geometrical face. The unit cell would then be equivalent to a $4N$-port network of the kind described in Sec. 3.2.3. This means that to solve the dispersion problem, we need to find the roots of the determinant of the matrix on the left side of (3.26). In this section, we only consider an irreducible structure of the kind presented in Fig. 3.12.

To demonstrate the relevance of the inter-cell interactions of the higher-order modes in 2-D glide-symmetric structures, we apply this method to the unit cell of a glide-symmetric structure. The parameters for the structure in Fig. 3.12 (a) are $h = 1.15$ mm, $h_1 = 1$ mm, $p = 1.2$ mm and $d = 0.5$ mm. Fig. 3.14 (a) plots the dispersion diagram of the glide and the corresponding non-glide structures. It shows that this is an irreducible glide-symmetric structure. Fig. 3.14 (b) depicts the dispersion diagram of this structure when propagation is in the x direction ($k_x \neq 0$, $k_y = 0$). We computed the dispersion diagram using two methods: our transmission-matrix method and the CST eigensolver. We plotted both results for comparison. Considering the CST results as our reference, the comparison of the curves proves that a transmission-matrix with one mode on each face ($N = 1$) does not yield the correct answer. On the other hand, one with 11 modes on each face obtains a perfect match with the CST eigensolver. Fig. 3.14 (c) plots the normalized attenuation constant of the Bloch wave (α_x/k_0) with respect to frequency. Once again, these cannot be compared to CST as the latter provides no data on the attenuation constant. The agreement between the results with 11 and 12 modes (for both phase constant and attenuation constant) confirm that adding extra modes does not change the converged result. These diagrams show that the periodic structure is indeed irreducible according to the definition given in previous sections, as higher-order mode interactions are needed to obtain an accurate result. Fig. 3.15 sketches the full 2-D dispersion diagram using the transmission-matrix analysis with 11 modes and compares it to the CST eigensolver solution. A good match between the two curves validates that the extended T-matrix method presented in Sec. 3.2.3 provides correct results for all propagation directions. In the next section, we try to reduce the computation domain of our problem to a volume smaller than a unit cell. This will decrease the computational cost of the method.

3.3.4 2-D Glide Conditions on the Boundaries of a Quarter of a Non-Minimal Unit Cell

In Sec. 3.3.2, we exploited the higher-order symmetries of the 1-D glide-symmetric structures and simplified the calculations. We follow the same approach in the 2-D domain. We will use one quarter of a unit cell to obtain the dispersion relation. First, we need to search for a quarter-cell unit that has proper symmetric characteristics to utilize. The generalized Floquet theorem

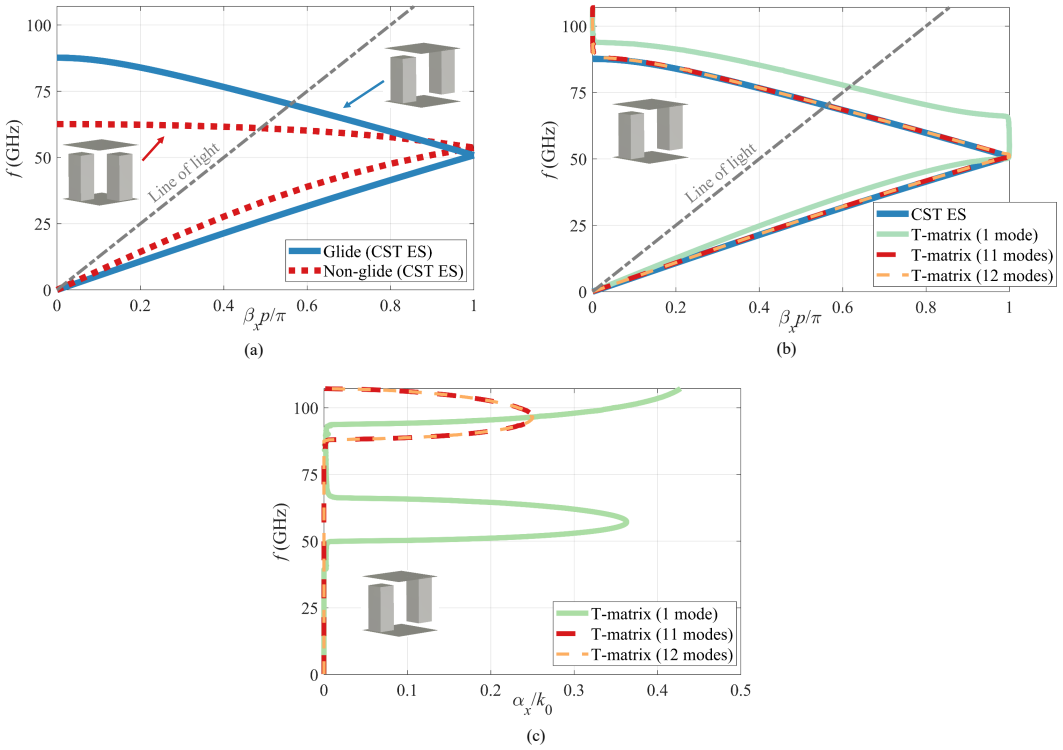

FIGURE 3.14: Dispersion diagram assuming a propagation along the x direction (i.e., $k_y = 0$) for the glide-symmetric structure in Fig. 3.12 (a). Geometrical parameters: $p_x = p_y = 1.2$ mm, $d = 0.5$ mm, $h_1 = 1$ mm and $h = 1.15$ mm.

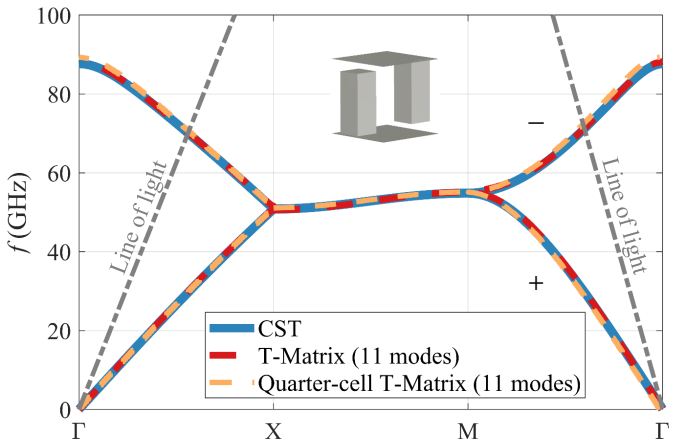

FIGURE 3.15: Full dispersion diagram of the structure in Fig. 3.12 (a). Geometrical parameters: $p_x = p_y = 1.2$ mm, $d = 0.5$ mm, $h_1 = 1$ mm and $h = 1.15$ mm.

for 2-D glide symmetric structures, not treated in [2], reads

$$\begin{aligned} &G_{mp_x\hat{\boldsymbol{x}},np_y\hat{\boldsymbol{y}}}\left[\boldsymbol{E}\left(x,z\right)\right] \\ &= \boldsymbol{E}\left(x+mp_x/2, y+np_y/2, -z\right) \\ &= \pm e^{-j\left(mk_xp_x/2+nk_yp_y/2\right)}\boldsymbol{E}\left(x,y,z\right) \end{aligned} \tag{3.36}$$

where m, n are odd integers. The factor $\pm$ in the last term of (3.36) allows to recover the translation property (3.34) if two glide operations are applied. Note that in order to apply 3.36 (in the general case of $m \neq 0$, $n \neq 0$), the boundaries of the minimal unit cell defined by (3.35) are not useful. We choose to enforce (3.36) on the boundaries defined by the two independent conditions $m = 1, n = 1$ and $m = 1, n = -1$:

$$\begin{aligned} \boldsymbol{E}\left(x + \frac{p_x}{2}, y + \frac{p_y}{2}, -z\right) &= \pm e^{-j\left(k_x \frac{p_x}{2} + k_y \frac{p_y}{2}\right)} \boldsymbol{E}\left(x, y, z\right) \\ \boldsymbol{E}\left(x + \frac{p_x}{2}, y - \frac{p_y}{2}, -z\right) &= \pm e^{-j\left(k_x \frac{p_x}{2} - k_y \frac{p_y}{2}\right)} \boldsymbol{E}\left(x, y, z\right) \end{aligned} \tag{3.37}$$

These boundaries define a quarter of the non-minimal cell in the new rotated (x', y') Cartesian reference system of Fig. 3.13 (dashed lines).

In order to recover the plus sign in (3.34) after the two glide operations are applied sequentially, the same $\pm$ signs must be chosen in both equations of (3.37). Notice that if either k_x or k_y is fixed, the sign choice is arbitrary as in the 1-D case, as long as the same sign is chosen. A change in both equations changes the harmonic of the fixed wavenumber. On the contrary, the choice is important if propagation along a certain skew direction is considered and the condition $k_y = ck_x$ is enforced, with c a non-zero constant. In this case, the choice of the (same) sign in (3.37) depends on the Floquet mode to be found (more specifically, on its behavior within each unit cell). This will be explained for the numerical example shown.

We transform the conditions of (3.37) into a finite-dimensional problem whose domain is restricted to the quarter of non-minimal unit cell whose transmission matrix is $\underline{\boldsymbol{T}}_{1/4}$:

$$\underline{\boldsymbol{T}}_{1/4} \cdot \begin{bmatrix} \boldsymbol{V}_1 \\ \boldsymbol{V}_2 \\ \boldsymbol{I}_1 \\ \boldsymbol{I}_2 \end{bmatrix} = \pm \begin{bmatrix} \underline{\boldsymbol{Q}} & \underline{\boldsymbol{0}} \\ \underline{\boldsymbol{0}} & \underline{\boldsymbol{Q}} \end{bmatrix} \cdot \begin{bmatrix} e^{-j\left(k_x \frac{p_x}{2} + k_y \frac{p_y}{2}\right)} \boldsymbol{V}_1 \\ e^{-j\left(k_x \frac{p_x}{2} - k_y \frac{p_y}{2}\right)} \boldsymbol{V}_2 \\ e^{-j\left(k_x \frac{p_x}{2} + k_y \frac{p_y}{2}\right)} \boldsymbol{I}_1 \\ e^{-j\left(k_x \frac{p_x}{2} - k_y \frac{p_y}{2}\right)} \boldsymbol{I}_2 \end{bmatrix} \tag{3.38}$$

where the $\pm$ sign, being the same in the two boundaries, can be brought outside the vectors in the right terms. The matrix $\underline{\boldsymbol{Q}}$ is defined as in (3.32) with respect to the parity of the vertical components of the modal electric fields e_z, used to define the equivalent voltages.

We have computed the full dispersion diagram of the irreducible structure of Fig. 3.12 (a) using the T matrix of a quarter of the unit cell using (3.38) and added the result to Fig. 3.15. The plot shows that with 11 modes, a convergence to the correct solution is reached. As an example, the first four relevant modes are those of a rectangular waveguide with PMC lateral walls. They are the TEM, TM_{01}, TE_{10} and TE_{11} modes. The TEM and TE_{10} have even symmetry with respect to z, so the sign factors $q^{(1)}$ and $q^{(3)}$ are chosen equal to +1. In contrast, TM_{01} and TE_{11} have odd symmetry in the z direction and a $q^{(i)}$ factor of -1 is adopted for these modes. The same procedure applies to the higher modes.

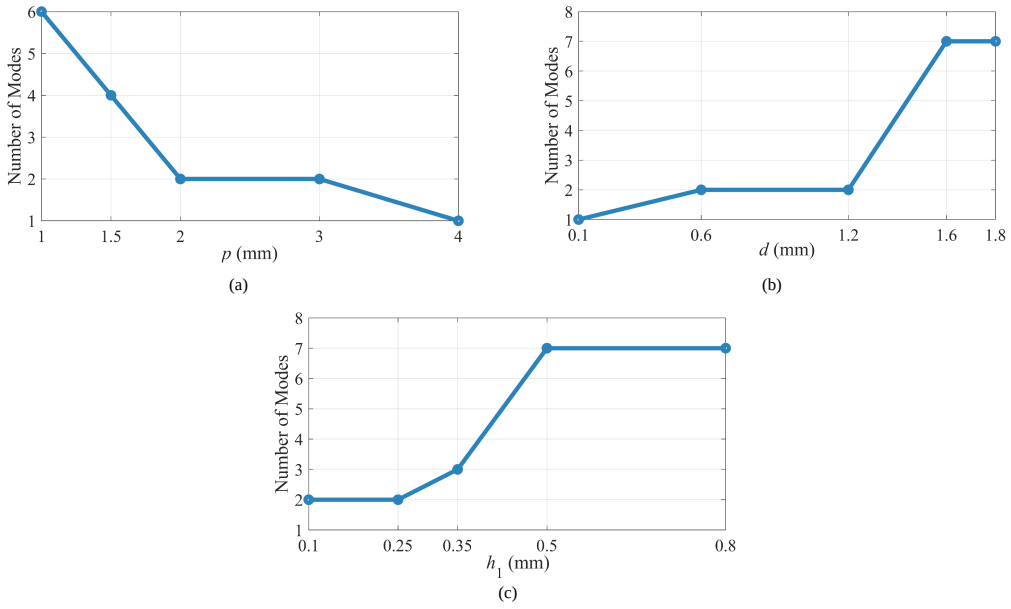

FIGURE 3.16: Number of modes needed for convergence of the T-matrix method: (a) Versus period p ($h_1 = 0.5$ mm, $h = 1.15$ mm and $d = 0.1$ mm). (b) Versus pin width d ($h_1 = 0.5$ mm, $h = 1.15$ mm and $p = 4$ mm). (c) Versus pin height h_1 ($p = 4$ mm, $h = 1.15$ mm and $d = 0.1$ mm).

Close to each curve, we show the sign used in (3.38) to recover the mode. As stated previously, in the segments $\Gamma - X$ and $X - M$ the choice of the sign is arbitrary since $k_y = 0$ and $k_x = \pi/p_x$ is fixed, respectively. In the segment $M-\Gamma$, $k_x = k_y$ and the sign used is shown close to each curve.

3.3.5 Parameter Study on the Reducible Condition

Now, we perform a parameter study on the structure of Fig. 3.12 (a). We consider the propagation of the Bloch waves to be in the x direction, and we look for the number of modes needed for convergence of the first two Bloch modes (e.g., from 0 to 100 GHz) using the transmission-matrix method. Fig. 3.16 (a) shows the required number of port modes for different periods while all the other parameters are kept constant. One can observe that as the period increases, fewer modes are needed for the convergence. This could be predicted since as the period increases, the corrugations are further away from each other, causing weaker couplings between them. Fig. 3.16 (b) shows a similar plot for different pin widths (d) and Fig. 3.16 (c) demonstrates the role of the height of the pins (h_1). Studying these two figures confirm that an increase in h_1 or in d, increases the number of modes required for the method's convergence. This can be explained by the fact that the increase of these values causes a closer proximity of the corrugations, thus making more waveguide modes significant.

The requirement of higher-order modes is partially related to the cut-off frequencies of the waveguide modes. In fact, as the number of modes increases, the higher-order modes become significant according to the order

of their cutoff frequencies. However, modes can be necessary even if under cutoff. For instance, the first two Floquet modes of the 2-D glide-symmetric structure of Fig. 3.12 (a) in Fig. 3.14 are both below the cut-off frequencies of all TM and TE modes of the exciting waveguide. Nevertheless, 11 modes are still needed to calculate the dispersion diagram.

The study of the convergence can be performed by running different simulations for increasing N, until the convergence is met. However, one can eliminate this step by knowing in advance how many modes are needed from the beginning. Our experiments show that the magnitude of the scattering parameters can be a good predictor of the number of significant modes. Significant modes are those for which at least one of the scattering parameters has a magnitude higher than a certain threshold (in our numerical results, a threshold of -10 dB is sufficient).

3.3.6 Computation Time

In this section, we study the time cost of our multimodal transmission matrix method. it would be useful to have a comparison between the computational time of the transmission-matrix method and the CST eigensolver. To this aim, we apply the two methods to the same structure and compare the execution time for each one. We consider the 2-D glide-symmetric example discussed in Sec. 3.3.3 and Sec. 3.3.4. For the calculations, we used a computer with 128 GB of RAM and an Intel(R) Xeon(R) CPU with 6 cores and a base frequency of 3.60 GHz for its CPU cores. First, it is necessary to note that it is not very straightforward to compare the time cost of these two methods due to the difference in their nature. For instance, the CST eigensolver performs a sweep of the phase constant, whereas the transmission-matrix method perform a sweep on the frequency.

For our comparison, we computed 74 points on the dispersion diagram in each method. The execution time of the CST eigensolver, in this case, was 402 seconds. Next, we applied the transmission-matrix method in two steps. In the first step, we used the CST Frequency solver to extract the scattering parameters for the quarter of a unit cell used in Sec. 3.3.4. For this matter, the frequency range of 0-90 GHz was used and four waveguide ports were applied with 12 modes at each port. This provided us with the multimodal scattering matrix for $N \leq 12$. The execution time for the first step was 82 seconds. Then, we calculated the transmission matrix from the CST scattering parameters using a simple MATLAB code [51], whose execution time (around 10 ms) is negligible. In the second step, we used the algorithm in [52] to find the complex roots of the eigenvalue problem in (3.38). This part was also done in MATLAB. The execution time of the second step is given in Table 3.1, and it is clearly much faster than the full-wave simulation. In fact, calculation of all the first 11 cases (11 modes were needed for convergence) takes less than 4 seconds in total. As a result, the standard CST eigenvalue solver (solving for a full cell) required 402 s, while the transmission matrix method (solving for a quarter of cell) with 12 modes required 82+1.13 s with 12 modes at each port.

TABLE 3.1: Computational time for solving the eigenvalue problem in (3.38)

Number of modes (N)	Time (seconds)	Number of modes (N)	Time (seconds)
1	0.04	7	0.39
2	0.07	8	0.49
3	0.07	9	0.52
4	0.08	10	0.64
5	0.11	11	0.88
6	0.16	12	1.13

3.4 Twist-Symmetric Structures

In this section, first we apply the 1-D transmission matrix eigenvalue problem that was developed in Sec. 3.2.2 to a few twist symmetric structures. Then, we try to come up with a new eigenvalue problem that concerns only one of the N sub-unit cells to reduce the computational complexity of the analysis.

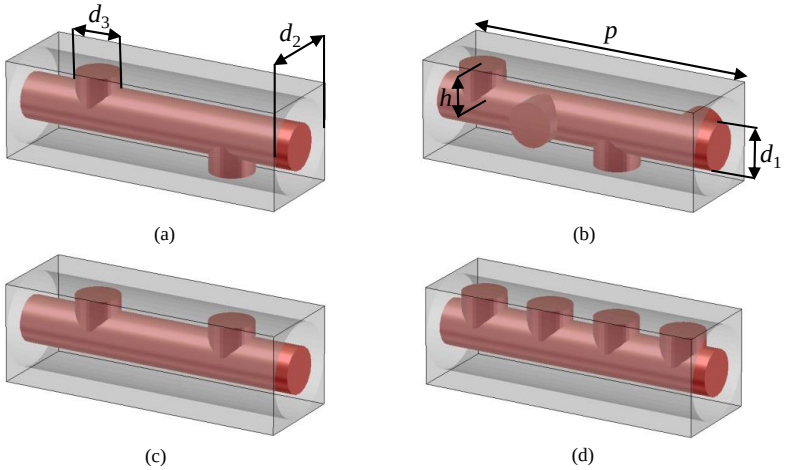

FIGURE 3.17: pin-loaded coaxial transmission lines: (a) 2-fold twist-symmetric (b) 4-fold twist-symmetric (c) Non-twist symmetric with 2 pins (d) Non-twist symmetric with 4 pins ($d_1 = 2.4$ mm, $d_2 = 4.84$ mm, $d_3 = 2.4$ mm and $h = 2$ mm).

3.4.1 Reducible and Irreducible twist structures

Fig. 3.17 (a) and (b) show the unit cells of twist-symmetric coaxial transmission lines loaded with circular pins. Fig. 3.17 (a) has a 2-fold twist symmetry. Therefore, the two pins are distanced half a period and rotated 180° with respect to each other. Fig. 3.17 (b) shows a 4-fold twist symmetry with 4 pins in each unit cell. The translations of the sub-unit cells have a length equal to a quarter of a period and the rotation between adjacent sub-unit cells is 90° in this case.

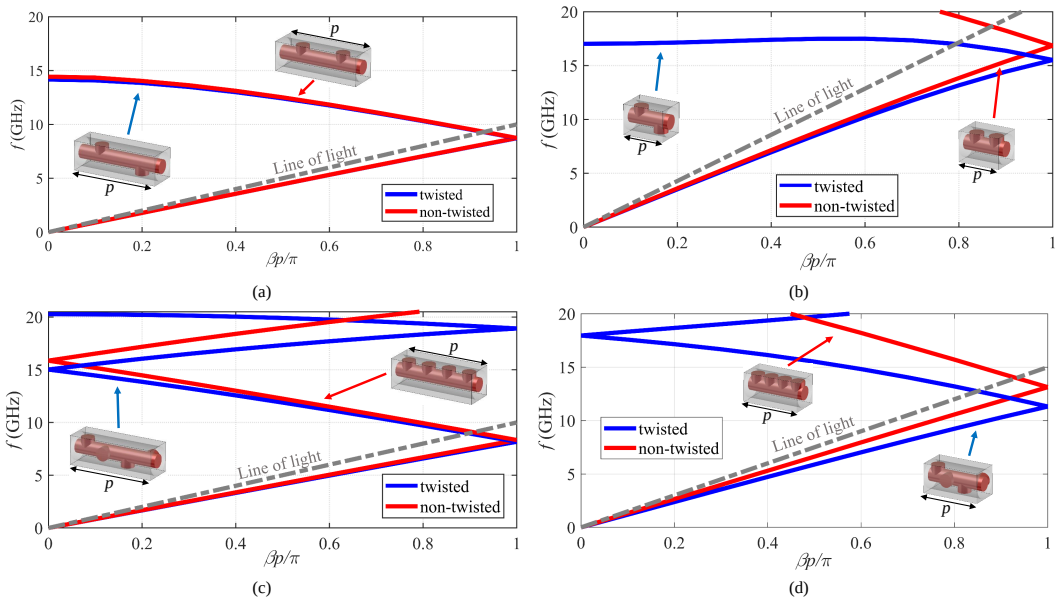

FIGURE 3.18: Dispersion diagram comparison of the twist-symmetric and their non-twist symmetric structures shown in Fig. 3.17: (a) with 2 pins ($p = 15$ mm) (b) with 2 pins ($p = 7$ mm) (c) with 4 pins ($p = 15$ mm) (d) with 4 pins ($p = 10$ mm).

Similar to the glide symmetry, we consider an equivalent non-twist symmetric unit cells to distinguish reducible and irreducible structures. The non-twist symmetric equivalent unit cells are shown in Fig. 3.17 (c) and (d). These unit cells are derived by ignoring the $2\pi/N$ rotation of the sub-unit cells while retaining their π/N translations. It is easy to notice that this equivalent structure is a loaded periodic structure with period p/N.

Fig. 3.18 (a) shows the comparison between the dispersion diagram of a 2-fold twisted structure as in Fig. 3.17 (a) and its non-twisted associated structure as in Fig. 3.17 (c). The results are obtained with the CST eigensolver tool (CST ES) [53]. The structure in Fig. 3.17 (a) is reducible to a non-twisted periodic line, since the two dispersion curves are perfectly superimposed. The rotation of its sub-unit cells does not have an impact on its dispersion diagram. Fig. 3.18 (b) depicts the dispersion diagrams of similar structures as in Fig. 3.17 (a) and (c) but with different parameters (a shorter period of $p = 7$ mm). This time, the twisted line is irreducible, since it has a different dispersion diagram with respect to the non-twisted one. Fig. 3.18 (c) depicts the dispersion diagrams for a 4-fold twisted structure as in Fig. 3.17 (b) and its associated non-twisted structure as in Fig. 3.17 (d) with $p = 15$ mm. The comparison of the diagrams suggests that the 4-fold twisted line is irreducible at higher frequencies while it can be reduced to a simple non-twisted structure with smaller period in the lower frequencies. Fig. 3.18 (d) depicts the dispersion diagrams for the the same structures where the twisted line has a smaller period of $p = 10$ mm. The difference between the two results in this case demonstrates that this 4-fold twisted line is irreducible even at low frequencies.

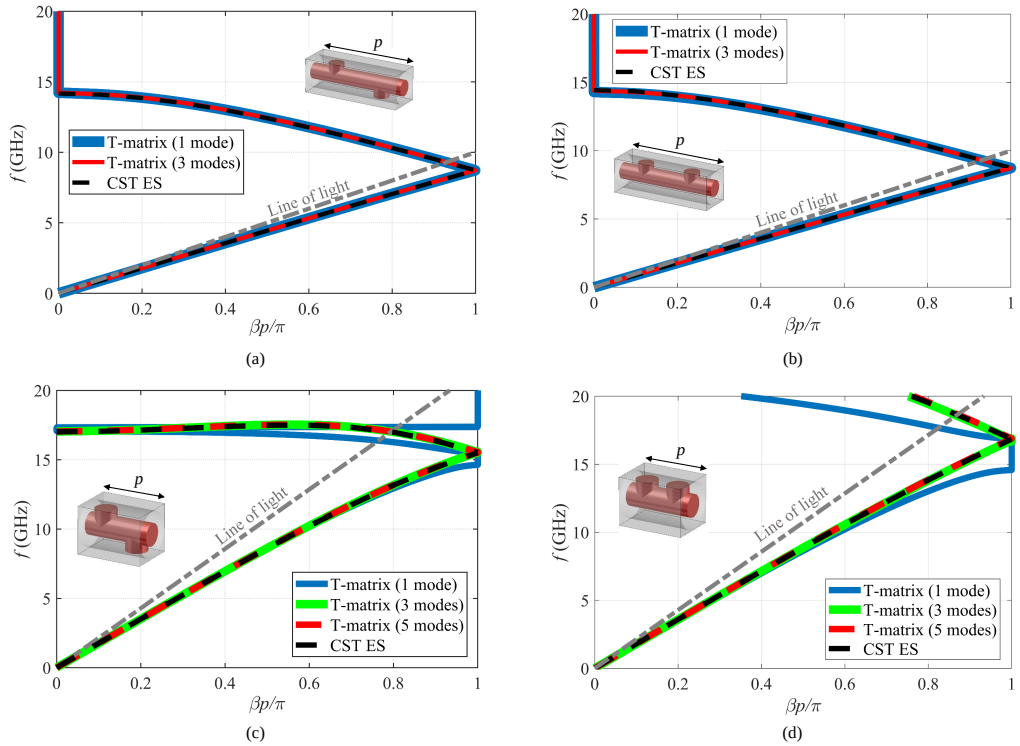

FIGURE 3.19: (a) Dispersion diagram of 2-fold twist-symmetric structures in Fig. 3.17 derived from the T matrix method and CST ES applied to their unit cells. (a) Twisted ($p = 15$ mm) and (b) associated non-twisted ($p = 15$ mm). (c) Twisted ($p = 7$ mm) and (d) associated non-twisted ($p = 7$ mm).

To examine the T-matrix method analysis on periodic structures with twist symmetry, we apply the 1-D eigenvalue problem of (3.23) to the unit cells of Fig. 3.17 and we compare the results to the CST eigensolver. Fig. 3.19 (a) depicts the dispersion curves obtained with (3.23) for the 2-fold *reducible* twisted cell studied in Fig. 3.18 (a). It also plots the dispersion diagram obtained with CST eigensolver for comparison. We observe that in this case, a monomodal T matrix (1 mode) is already enough to match the results obtained by CST. The results for a T matrix with 3 modes also matches the monomodal T matrix and the CST eigensolver results. This demonstrates that adding an extra set of degenerate modes does not vary the already converged results.

Fig. 3.19 (b) shows the same results for the associated non-twisted line. Also in this case, one single mode is sufficient to reach convergence. This confirms that in a reducible case a single mode is sufficient to accurately calculate the dispersion diagram of both the twisted and non-twisted lines.

Fig. 3.19 (c) depicts the dispersion diagram of the *irreducible* ($p = 7$ mm) 2-fold twisted unit cell studied in Fig. 3.18 (b) together with the dispersion diagram calculated with the CST eigensolver. Here a monomodal T-matrix method leads to the correct dispersion curve in the lower range of frequency. At higher frequencies, at least 3 modes are required. The results for 5 modes is also sketched in the figure to further emphasize the convergence.

Fig. 3.19 (d) shows the same results for the associated non-twisted line.

In this case, one mode only is not enough even at low frequencies. This confirms that the irreducibility of a twisted line is related to the presence of coupling through higher-order modes either in the twisted line or in its associated non-twisted line. These higher order modes interact with each other differently in presence or in the absence of twists, and lead to different dispersive behaviors.

Fig. 3.20 (a) depicts the dispersion diagram for the 4-fold twisted cell *irreducible at high frequencies* studied in Fig. 3.18 (c); Fig. 3.20 (b) shows the associated non-twisted line. Again, in the frequency ranges where the twisted line is irreducible, the presence of higher-order modes is necessary in at least one the two lines (the non-twisted line). This confirms that the difference between the lines arise from the presence of higher-order modes.

The same results are confirmed in Fig. 3.20 (c) and Fig. 3.20 (d) (4-fold twisted cell *irreducible over the entire frequency range* studied in Fig. 3.18 (d)): higher order modes are important in the non-twisted line over the entire range.

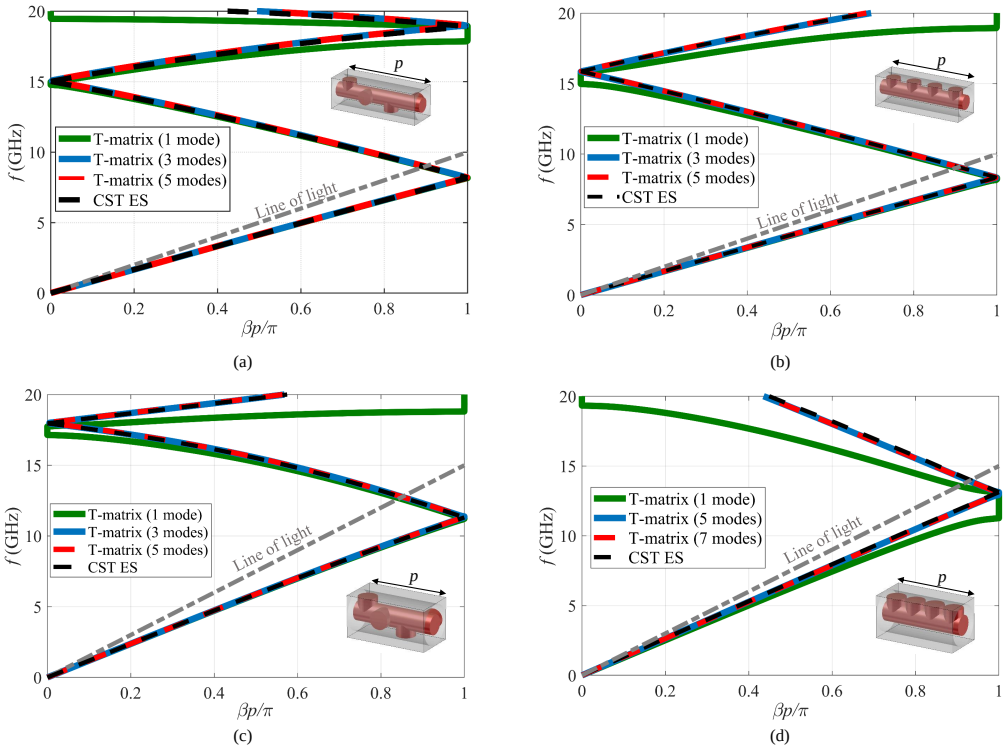

FIGURE 3.20: (a) Dispersion diagram of 4-fold twist-symmetric structures in Fig. 3.17 derived from the T-matrix method and CST ES applied to their unit cells. (a) Twisted ($p = 15$ mm) and (b) associated non-twisted ($p = 15$ mm). (c) Twisted ($p = 10$ mm) and (d) associated non-twisted ($p = 10$ mm).

These results confirm that, while reducible structures need a single fundamental mode, irreducible structures have a more complex modal interaction: either they or their associated non-twisted line need a multimodal T matrix. In this specific structure, the proximity of the pins is the key parameter that

makes higher-order modes relevant. The more tightly coupled the pins are, the more relevant the higher-order modes become. For instance, a reducible twisted structure in Fig. 3.17 (b) could become an irreducible structure by decreasing the period and increasing the size of the pins since these changes will move the pins closer to each other.

We have shown that modelling a unit cell with a multimodal T matrix is required for accurate dispersion results. As in the previous glide case, this approach can also be an effective alternative to retaining multiple unit cells as in [54]. Finally, we stress that also in this case this method leads to accurate results also when current eigenvalue tools of commercial software are not available, for example in the case of open structures, where the attenuation constant α can be related to radiation (e.g., leaky waves).

3.4.2 Twist Symmetry Conditions on a Sub-unit Cell

The N-fold twist symmetry operator defined in (2.18) is repeated here:

$$S_{N,p\hat{z}} : (\rho, \phi, z) \rightarrow \left(\rho, \phi + \frac{2\pi}{N}, z + \frac{p}{N}\right) \tag{3.39}$$

We again observe from (3.39) that a composition of N twist operators gives $T_{p\hat{z}}$, the translation operator of length p along z ($S^N_{N,p\hat{z}} = T_{p\hat{z}}$) which is expected since a twist-symmetric structure is also a periodic structure. Similar to the glide symmetry, the twist symmetry operator will help us to simplify the eigenvalue problem by reducing the computational domain from the unit cell to a sub-unit cell. Again, we consider n background modes for our analysis. Since the background structure has a circular section, the radial component of the electric field of the background modes has the following profile:

$$\Psi^{(m,i),e/h}_{(\pm)}(\rho, \phi) = f_{m,i}(\rho)\, e^{\pm jm\phi} \tag{3.40}$$

where $f_{m,i}$ are suitable linear combinations of Bessel functions expressing the radial dependence of each mode. The index m represents the order of angular dependence ($e^{\pm jm\phi}$), the index i the radial dependence, and e and h in the superscript stand for a TM and TE mode, respectively.

In periodic lines, Bloch modes are eigensolutions of the translation operator $T_{p\hat{z}}$:

$$T_{p\hat{z}}\left[\boldsymbol{E}(\rho, \phi, z)\right] = \boldsymbol{E}(\rho, \phi, z + p) = e^{-jk_z p}\boldsymbol{E}(\rho, \phi, z) \tag{3.41}$$

By virtue of the twist symmetry, Bloch modes are also eigensolutions of the twist operator $S_{N,p\hat{z}}$ [2]:

$$S_{N,p\hat{z}}\left[\boldsymbol{E}(\rho, \phi, z)\right] = \lambda \boldsymbol{E}(\rho, \phi, z) \tag{3.42}$$

where λ is the relevant eigenvalue. Note that the twist operator acts here on the observation point, and does not rotate the $\boldsymbol{E}$ field. Since $S^N_{N,p\hat{z}} = T_{p\hat{z}}$, from

(3.41) we can state that $\lambda^N = \mathrm{e}^{-jk_z p}$, and :

$$\lambda = \mathrm{e}^{-jk_z \frac{p}{N}} \tag{3.43}$$

where the different Nth roots merely correspond to different Floquet harmonics, so that they do not appear in (3.43).

The new eigenvalue problem in (3.42) with λ given in (3.43) determines the Bloch modes. However, we are interested to formulate an eigenproblem for the translation operator $T_{\frac{p}{N}\hat{\boldsymbol{z}}}$ rather than the twist operator. In fact, commercial software can easily compute a sub-cell transmission matrix, which describes the translation of fields and not the twist transformation. To overcome this problem, we first define the rotation operator:

$$R_{\frac{2\pi}{N}\hat{\boldsymbol{z}}}\left[\boldsymbol{E}\left(\rho,\phi,z\right)\right] = \boldsymbol{E}\left(\rho,\phi+2\pi/N,z\right) \tag{3.44}$$

and we express the translation operator $T_{\frac{p}{N}\hat{\boldsymbol{z}}}$ as a composition of the symmetry operator $S_{N,p\hat{\boldsymbol{z}}}$ and the inverse rotation operator $R^{-1}_{\frac{2\pi}{N}\hat{\boldsymbol{z}}} = R_{-\frac{2\pi}{N}\hat{\boldsymbol{z}}}$:

$$T_{\frac{p}{N}\hat{\boldsymbol{z}}}\left[\boldsymbol{E}\left(\rho,\phi,z\right)\right] = R^{-1}_{\frac{2\pi}{N}\hat{\boldsymbol{z}}} S_{N,p\hat{\boldsymbol{z}}}\boldsymbol{E}\left(\rho,\phi,z\right) = \mathrm{e}^{-jk_z\frac{p}{N}} R^{-1}_{\frac{2\pi}{N}\hat{\boldsymbol{z}}}\boldsymbol{E}\left(\rho,\phi,z\right) \tag{3.45}$$

The T-matrix formulations requires to express the Bloch mode as a composition of the modes of the background structure. This is a convenient basis when dealing with rotations, since each background mode in (3.40) satisfies the simple property:

$$R^{-1}_{\frac{2\pi}{N}\hat{\boldsymbol{z}}}\left[\Psi^{(m,i)}_{(\pm)}(\rho,\phi)\right] = e^{\mp jm\frac{2\pi}{N}}\Psi^{(m,i)}_{(\pm)}\left(\rho,\phi\right) \tag{3.46}$$

(the e/h polarization is not stated for simplicity). If the transmission matrix of a single *sub-unit* cell of an N-fold twisted structure, associated to the translation operator $T_{\frac{p}{N}\hat{\boldsymbol{z}}}$, is $\underline{\boldsymbol{T}}_{1/N}$, the conditions in (3.46) and (3.45) lead to the following eigenvalue problem:

$$\underline{\boldsymbol{T}}_{1/N}\begin{bmatrix}\boldsymbol{V}\\ \boldsymbol{I}\end{bmatrix} = e^{-jk_z\frac{p}{N}}\begin{bmatrix}\underline{\boldsymbol{Q}} & \underline{\boldsymbol{0}}\\ \underline{\boldsymbol{0}} & \underline{\boldsymbol{Q}}\end{bmatrix}\cdot\begin{bmatrix}\boldsymbol{V}\\ \boldsymbol{I}\end{bmatrix} \tag{3.47}$$

where $\boldsymbol{V}$ is the voltage and $\boldsymbol{I}$ is the current vector defined as:

$$\boldsymbol{V} = \begin{bmatrix} V^{\mathrm{TEM}}\\ \vdots\\ V^{(m,i),e/h}_{(\pm)}\\ \vdots\\ V^{(M,I),e/h}_{(\pm)}\end{bmatrix} \quad \text{and} \quad \boldsymbol{I} = \begin{bmatrix} I^{\mathrm{TEM}}\\ \vdots\\ I^{(m,i),e/h}_{(\pm)}\\ \vdots\\ I^{(M,I),e/h}_{(\pm)}\end{bmatrix} \tag{3.48}$$

The matrix $\underline{\underline{Q}}$ can be written as:

$$\underline{\underline{Q}} = \begin{bmatrix} 1 & 0 & \cdots & 0 \\ 0 & q_{(\pm)}^{(m,i)} & \ddots & \vdots \\ \vdots & \ddots & \ddots & 0 \\ 0 & \cdots & 0 & q_{(\pm)}^{(M,I)} \end{bmatrix} \tag{3.49}$$

where $q_{(\pm)}^{(m,i)} = \mathrm{e}^{\mp jm\frac{2\pi}{N}}$, and $\underline{\underline{0}}$ is the null square matrix.

Solving the generalized eigenvalue problem in (3.47) gives the propagation constant k_z starting from the simulation of a sub-unit cell of the twisted line. This formulation reduces the volume of the computational domain of the periodic problem by a factor N.

However, commercial electromagnetic software often calculates scattering parameters by means of waveguide modes with angular dependence of the trigonometric forms $\cos(m\phi)$ or $\sin(m\phi)$ rather than the exponential form of $\mathrm{e}^{\pm jm\phi}$. Therefore, a generalized eigenvalue problem based on these functions is useful for a practical implementation of the method. The radial components of the electric fields of these trigonometric modes are:

$$\begin{aligned} \Psi_{\cos}^{(m,i),e/h}(\rho,\phi) &= g_{(m,i)}^{e/h}(\rho)\cos(m\phi) \\ \Psi_{\sin}^{(m,i),e/h}(\rho,\phi) &= g_{(m,i)}^{e/h}(\rho)\sin(m\phi) \end{aligned} \tag{3.50}$$

where $g_{(m,i)}^{e/h}$ are suitable radial functions. Applying the inverse rotation operator to these electromagnetic fields gives (note again that the rotation is performed on the observation point, not on the vector field):

$$\begin{aligned} R_{\frac{2\pi}{N}\hat{z}}^{-1}\left[\Psi_{\cos}^{(m,i),e/h}(\rho,\phi)\right] = \Bigg[&\cos\left(\frac{2\pi m}{N}\right)\Psi_{\cos}^{(m,i),e/h}(\rho,\phi) \\ &+ \sin\left(\frac{2\pi m}{N}\right)\Psi_{\sin}^{(m,i),e/h}(\rho,\phi)\Bigg] \end{aligned} \tag{3.51}$$

$$\begin{aligned} R_{\frac{2\pi}{N}\hat{z}}^{-1}\left[\Psi_{\sin}^{(m,i),e/h}(\rho,\phi)\right] = \Bigg[&-\sin\left(\frac{2\pi m}{N}\right)\Psi_{\cos}^{(m,i),e/h}(\rho,\phi) \\ &+ \cos\left(\frac{2\pi m}{N}\right)\Psi_{\sin}^{(m,i),e/h}(\rho,\phi)\Bigg] \end{aligned} \tag{3.52}$$

It is interesting to note that the rotation (and then also the twist condition) is no more diagonal in the trigonometric basis: rotating one mode gives a combination of two degenerate modes, with the only exception occurring for $m = 0$, where only the cos term exists. This means that we have to retain both the cos and the sin modes for each $m \neq 0$.

The generalized eigenvalue in (3.47) changes to:

$$\underline{\boldsymbol{T}}_{1/N}\begin{bmatrix}\boldsymbol{V}'\\ \boldsymbol{I}'\end{bmatrix} = e^{-jk_z\frac{p}{N}}\begin{bmatrix}\underline{\boldsymbol{Q}}' & \underline{\boldsymbol{0}}\\ \underline{\boldsymbol{0}} & \underline{\boldsymbol{Q}}'\end{bmatrix}\cdot\begin{bmatrix}\boldsymbol{V}'\\ \boldsymbol{I}'\end{bmatrix} \tag{3.53}$$

where the primed voltage and current vectors $\boldsymbol{V}'$ and $\boldsymbol{I}'$ are defined based on the trigonometric background modes:

$$\boldsymbol{V}' = \begin{bmatrix} V^{\text{TEM}}\\ \vdots\\ V_{\cos}^{(m,i),e/h}\\ V_{\sin}^{(m,i),e/h}\\ \vdots\\ V_{\cos}^{(M,I),e/h}\\ V_{\sin}^{(M,I),e/h}\end{bmatrix} \quad \text{and} \quad \boldsymbol{I}' = \begin{bmatrix} I^{\text{TEM}}\\ \vdots\\ I_{\cos}^{(m,i),e/h}\\ I_{\sin}^{(m,i),e/h}\\ \vdots\\ I_{\cos}^{(M,I),e/h}\\ I_{\sin}^{(M,I),e/h}\end{bmatrix} \tag{3.54}$$

The definition of the primed matrix $\underline{\boldsymbol{Q}}'$ is also given here:

$$\underline{\boldsymbol{Q}}' = \begin{bmatrix} 1 & 0 & \cdots & \cdots & \cdots & \cdots & 0\\ 0 & \ddots & \ddots & \ddots & \cdots & \cdots & \vdots\\ \vdots & \ddots & \cos\left(\frac{2\pi m}{N}\right) & \sin\left(\frac{2\pi m}{N}\right) & \cdots & \cdots & \vdots\\ \vdots & \ddots & -\sin\left(\frac{2\pi m}{N}\right) & \cos\left(\frac{2\pi m}{N}\right) & \cdots & \cdots & \vdots\\ \vdots & \ddots & \ddots & \ddots & \ddots & 0 & 0\\ \vdots & \ddots & \ddots & \ddots & 0 & \cos\left(\frac{2\pi M}{N}\right) & \sin\left(\frac{2\pi M}{N}\right)\\ 0 & \cdots & \cdots & \cdots & 0 & -\sin\left(\frac{2\pi M}{N}\right) & \cos\left(\frac{2\pi M}{N}\right)\end{bmatrix} \tag{3.55}$$

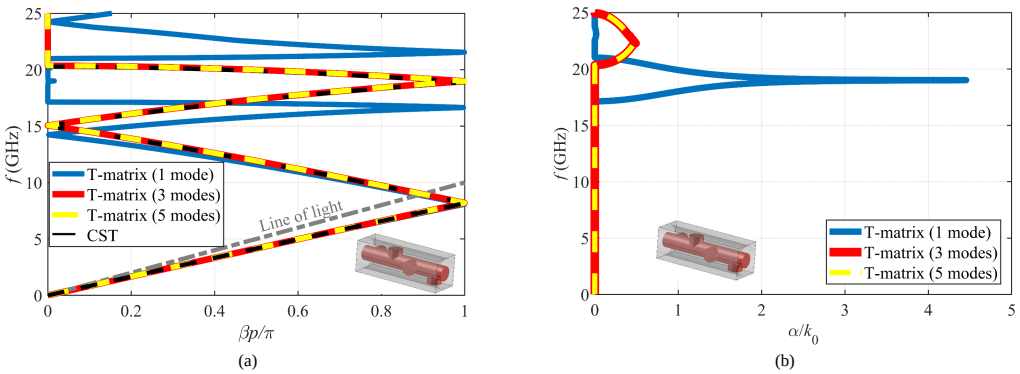

FIGURE 3.21: Dispersion diagram derived with T matrix method on the sub-unit cell of the structure in Fig. 3.17 (b) (p=15 mm): (a) Normalized phase constant $\beta p/\pi$ vs. frequency. (b) Normalized attenuation constant α/k_0 vs. frequency (k_0 being the free-space wavenumber).

TABLE 3.2: Computational time for solving the periodic structure in Fig. 3.17 (b)

1 frequency point	**T matrix (sub-unit cell)**	**T matrix (unit cell)**	**CST (eigensolver)**
Time (s)	12	19	13
76 frequency points	**T matrix (sub-unit cell)**	**T matrix (unit cell)**	**CST (eigensolver)**
Time (s)	21	88	780

Fig. 3.21 (a) plots the normalized phase constant of a structure with a 4-fold twist-symmetry in Fig. 3.17 (b) ($p = 15$ mm) derived with (3.53) and compares it to the results given by CST. It is observed that a single mode does not provide the correct dispersion diagram at high frequencies, whereas considering 3 modes (TEM mode and the first two degenerate higher order modes) leads to the accurate diagram which matches the CST results over the entire frequency band shown. To further emphasize the advantages of the T matrix method, the normalized attenuation constant of the structure is also given in Fig. 3.21 (b) where it is easy to notice that the stopband predicted with a single mode is not correct while using 3 modes correctly predicts the frequency range of first stopband. These results could not be compared to CST since the commercial software does not provide such information. The results with inclusion of 5 modes is also plotted in these two figures and they match the results of 3-mode T matrix method. It is important to note that even though we have used the pin-loaded transmission lines in Fig. 3.17 to verify our method, the eigenvalue problems in (3.47) and (3.53) are general and they can be applied to any structure with a twist symmetry. Furthermore, the method is also valid for a larger class of structure, characterized by the invariance under the twist transformation (2.18) with non-integer N. In this last case, the structure is no more periodic and therefore cannot be studied with available commercial software. The present approach still holds and at the best of the author's knowledge is the only formulation available for a rigorous solution of the problem.

Finally, it is interesting to compare the solving time of the T-matrix method applied to a sub-cell and the CST eigensolver in an entire unit cell. To do so, we consider the more complex case of the 4-fold twist symmetry where 3 modes were needed in the T matrix method. To make this comparison, we choose 76 points on the first passband and solved the problem for this frequency range. For CST eigensolver, an adaptive mesh refinement with maximum of 1% relative error in frequency is defined using tetrahedral meshes. As a result, the cell is meshed with 19 850 tetrahedrons. For CST frequency-domain solver, a relative error of 1% for scattering parameters is defined in the adaptive mesh refinement routine with tetrahedral meshes, resulting in a total of 14 310 tetrahedrons for the entire cell and 4 016 tetrahedrons for the sub-cell. We have used a computer with 128 GB of RAM and an Intel(R) Xeon(R) CPU with 6 cores and a base frequency of 3.60 GHz for its CPU cores.

The computation time for these methods are included in Table 3.2. A

quick comparison for the case of a single frequency point shows that even though the T matrix method with a unit cell has a higher computation time compared to CST, the T matrix method with the sub-unit cell is slightly faster than CST. It should be noted that a higher computation time of the unit cell formulation may be justified since the T matrix generally produces extra information on the attenuation constant of the Bloch waves and can be applied also to open structures. As we consider a large frequency range, the computation time difference changes dramatically. The T matrix method has a shorter computation time for both the unit cell and sub-unit cell formulations (88 and 21 seconds respectively) compared to CST (780 seconds). This occurs because the computation of the scattering parameters is accelerated significantly by the broadband sweep techniques. The rest of the computation (solving the T matrix eigenvalue problem) is executed very fast. For instance, this part was executed in less than 2 seconds for 76 frequency points and 3 modes for both the unit cell and the sub-unit cell formulations. This is a significant reduction in computation time compared to the CST eigensolver.

3.5 Conclusions

In summary, in this chapter, we developed and introduced a multimodal T matrix method to obtain the Bloch modes of periodic structures. we used this method to investigate the relation between higher-symmetric and non-higher-symmetric structures with reduced periods. We discussed the idea of reducibility based on whether a higher symmetric structure is equivalent to a non-higher-symmetric structure with no higher symmetry. We studied the relevance of higher order modal interactions between the unit cells to give a more precise definition of the concept of reducibility of a higher-symmetric configuration. We then used the symmetry operators corresponding to the two higher symmetries, namely glide and twist symmetries, to present a new formulation of the multimodal T matrix method which utilizes a sub-region of the unit cell instead of the entire cell. We showed that this leads to faster computation time for structures with higher symmetries. We pointed out how this multimodal method computes both phase and attenuation constants of Bloch modes, which is not achieved with commercial software. This characteristic makes such method useful for applications such as electromagnetic bandgap materials or leaky-waves.

Chapter 4

Reconfigurable Waveguide Technology Based on Glide Symmetry

4.1 Introduction on MM-Wave Switches

Fifth-generation (5G) of mobile communication systems tackles the problem of ever-growing capacity demands and aims to provide higher throughput wireless connectivity [55, 56, 57]. High data rate of the order of gigabits per second (Gb/s), a latency time in milliseconds, high traffic volume density, and improved spectral and energy efficiencies are the main requirements that are attributed to this new generation of wireless communications. Millimeter-wave (MMW) wireless systems are emerging as a promising technology for achieving these requirements [58, 59, 60, 61]. Recent advances in design of low-cost high performance integrated circuits (ICs) at MMW frequencies and the large amount of underutilized spectrum in these frequencies are the main factors in their emergence as the go-to technology in 5G [62, 63, 64]. Therefore, frequency bands such as 28 GHz and 40 GHz have been authorized for 5G use while the 3GPP release 17 is currently investigating the spectrum above 52.5 GHz, with a specific focus on the 60 GHz licence-free band [65]. MMW multibeam antennas (MBAs) are considered in the phase 2 of 5G deployment with suitable beamforming techniques to achieve massive multiple-input, multiple-output (MIMO) [66, 67, 68]. This significantly enhances the spectral and energy efficiency while it minimizes interference levels.

The most expensive parts of a wireless transceiver are the radio frequency (RF) chains, digital-to-analog converters (DACs), and analog to digital converters (ADCs). In MMW massive MIMO wireless systems, a huge number of antennas are used to mitigate the large free-space attenuation. Therefore, employing one RF chain and one ADC or DAC for each antenna would prove too costly. Furthermore, it would also increase the energy consumption of the transceiver to an unacceptably high degree. Hence, employing one RF chain for each antenna is not feasible. Hybrid analog/digital beamforming architectures are proposed as a solution to this limitation [69, 70, 71, 72]. In such architectures, the number of RF chains is typically much lower than the number of antennas and therefore, analog beamformers with phase shifters

[73], Butler Matrices [74], or lenses [75], are considered to feed all antennas. While Butler-Matrix-based and lens-based hybrid arrays exhibit less complexity, they require a beam selector made of switches to map the few RF chains to the large number of analog beamformer inputs [75].

Recently, switching networks have also been suggested to replace phase shifters in analog beamformers in order to reduce their complexity while increasing their power and spectral efficiencies [76]. Consequently, the design of power-efficient millimeter-wave switches is a key aspect in the implementation of hybrid analog/digital massive MIMO systems.

Typical conventional waveguide switches are represented by mechanical, semiconductor pin diodes, and FET switches [77]. Mechanical switching is done by physically blocking or opening the transmission path in a device, by activating an electromagnetic relay with a control signal. An electromagnetic relay normally uses an electromagnet that moves an armature for actuation. A control spring is also used to pull the armature back to its initial position. Electromechanical switches demonstrate low insertion loss and high isolation and they can handle high power applications. However, they are bulky and very slow in their switching speed. For applications where the switching speed is more important than the power handling, solid-state semiconductor switches are preferred. These electronic switches use either diodes or FETs as their semiconductor switching element. These semiconductor devices have a semiconductor junction acting as an electronic control element which can be switched on or off by controlling its bias voltage. [78] discusses the series and parallel configuration of PIN diodes in waveguide switches at MMW frequencies. Furthermore, FET switches are regarded as important monolithic microwave integrated circuits (MMIC) elements. Compared to PIN diodes, the MMIC switches operate over a broad bandwidth, lower power consumption and faster switching speed whereas they exhibit a higher insertion loss [77]. For signal frequencies above 1 GHz, the solid-state switches have large insertion loss and poor isolation [77]. These limitations in solid-state technology has led to research for alternative technologies.

To summarize the characteristics of these two classes of switches, solid-state switches have low power handling and high insertion loss, while electromechanical switches can handle high power with low insertion loss, but are useful only at lower RF frequencies and operate at slower switching speeds. This led to the emergence of the microelectromechanical systems (MEMS) as a technology which incorporates the advantages of both solid-state and electromechanical systems. MEMS switches have low insertion loss, good isolation and low power consumption while they have a better power handling capability than semiconductor switches. Different actuation mechanisms exist for MEMs technology and they include electrostatic, electromagnetic, piezoelectric, magnetic and thermal actuation. One of the main disadvantages of MEMS switches is the low switching speed compared to solid-state switches [77]. Multiple MEMS-based waveguide switches have been designed for the MMW frequency band [79, 80, 81]. [82] reviews the research and analysis of MEMS switches in different frequency bands.

We are here interested to develop a reconfigurable technology capable to drive a millimeter-wave multi-beam antenna (Butler-Matrix or lens-like based) by selecting the input port of the system. The frequency range is the unlicensed band 57-70 GHz. The switching technique is chosen to be based on piezoelectric actuator, because of their low power consumption, despite the low switching rate. We use SLC-1730 linear piezoelectric actuators from the SmarAct company with dimensions of $30 \times 17 \times 8.5$ mm and weight of 20 N. It has a velocity of more than 20 mm/s, closed loop resolution of 50 nm and closed loop repeatability of 1000 nm.

Since the switch is capable of modifying mechanically the distance between different surfaces (by pulling or pushing them apart), it is compatible with a common millimeter-wave technology, the with gap waveguide [83]. In this technology, the electromagnetic wave is guided in an air region rather than inside a dielectric, resulting in reduced losses compared e.g. to substrate-integrated waveguides. Gap waveguide technology uses two contact-less plates that are separated by a gap. This not only eases the manufacturing process (which can be performed in two separate parts) but also allow to modify their distance with the aim of reconfiguring the wave propagation properties of the device. In gap waveguides, perfect magnetic conductor (PMC) boundary conditions are created on the two sides of the waveguide by means of an electromagnetic band-gap (EBG) material [84, 85, 86]. Bed-of-nail metasurface is among the most widely used configurations for this purpose [87, 88].

As said in Ch. 2, new EBG designs for gap waveguides have been proposed in order to enhance their confinement properties without adding significant complexity to the design by means of glide-symmetric holes or pins [17, 18]. This symmetrical configuration exhibit wider and stronger stop-bands compared to non-glide-symmetric periodic structures, which explains the motive to use them as EBG materials for gap waveguides. These properties along with the contact-less nature of the metasurfaces, make glide-symmetric metasurfaces an interesting candidate to embed reconfigurable properties in gap waveguides. The impact of multiple geometric parameters on the transmission properties of glide-symmetric waveguides was studied in recent work [89]. Recently, a mechanical waveguide switch was designed in Ku frequency using the contact-less properties of the gap waveguide technology [90].

In this chapter, we propose an integrated waveguide presenting a two-state functioning. An “on-state” allows the propagation through the guide, while an “off-state” stops the propagation. Thanks to the contact-less configuration, the switching between the two states is done by mechanically adjusting the distance between the top and bottom plates. In this design, glide-symmetric EBGs offer strong stop-band characteristics while glide-symmetric pin-like medium inside the waveguide ensure nearly dispersion-less wave propagation. This kind of geometry can open the implementation of switches where the signal propagation can occur along different paths, each one formed by a reconfigurable waveguide described here.

4.2 Reconfigurable Waveguide Design

The aim of this section is to propose a structure to implement a reconfigurable artificial waveguide that can alternate between "on" and "off" states in MMW region. It discusses the design of both "on" and "off" states and provides simulation results of the waveguide to study its performance in the two states.

The artificial waveguide employs EBG structures at its lateral boundaries to confine the field inside the guide. Fig. 4.1 shows a perspective view of an artificial waveguide with its different medium regions. The guiding medium is sandwiched between the two EBG regions and the propagation direction is shown with an arrow. The EBG medium confines the fields within the guiding medium while the guiding medium propagates them along the direction shown by the arrow. In our design, the guiding region is filled with an artificial medium to create possibilities for reconfiguration of the waveguide. The choice of the artificial media and the complete design procedure of different parts of the waveguide, including the guiding medium, the EBG, and a matching section is discussed in the subsequent subsections.

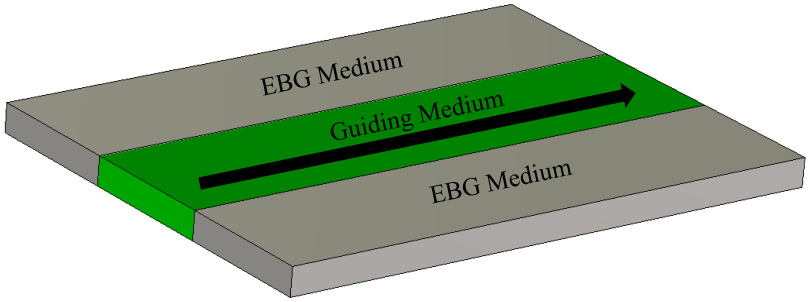

FIGURE 4.1: Division of medium regions in an artificial waveguide.

The artificial waveguide employs two parallel plates. These parallel plates are loaded with pins to create glide-symmetric pin-like media as in Fig. 3.12. In the EBG regions, the pin-like medium is designed to create strong EBG performance (namely, a high attenuation in the operating frequency range of interest). In the guiding medium, the geometric parameters ensure that a passband exists to enable wave propagation.

The reconfiguration is achieved by modifying the distance between the pin-like surfaces. One of the two surfaces can be pulled/pushed by means of a piezoelectric actuator. Therefore, when passing from the "on" to the "off" state the PPW height of both EBG and guiding medium will vary *of the same quantity*. Going into the "off" state, the EBG must keep its bandgap properties and the guiding medium must transform its passband into a stopband to prevent wave propagation.

4.2.1 Design of Guiding Medium and EBG

It was discussed in Ch. 2 that glide symmetric structures achieve wider and stronger stopband compared to a single metasurface with no glide symmetry [17]. Therefore, to achieve a high EBG performance, a glide-symmetric configuration of pins is chosen as the EBG medium. The guiding medium of the waveguide is also realized with a pin-like pair of metasurfaces exhibiting glide symmetry in order to benefit of its weak frequency dispersion.

The unit cells of both EBG and guiding media are shown in Fig. 4.2. It is important to note that the different behavior between the unit cells are achieved by only modifying the period p of the unit cell while keeping all the other parameters the same in the two. A parametric study on the unit cell of the glide-symmetric pin-like unit cells shown in Fig. 4.2 is adopted next to provide information on the effects of modifying different geometric parameters. This study clarifies how modification of the period can create the desired behaviors in the two media.

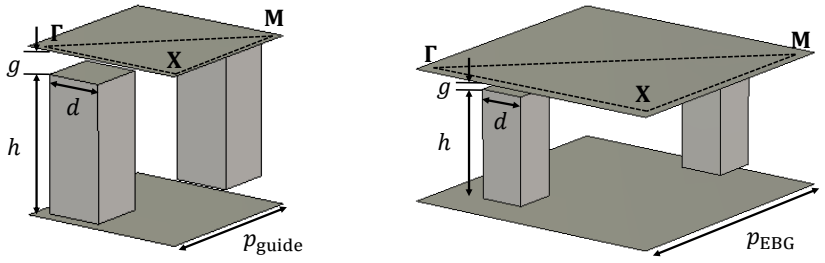

FIGURE 4.2: Unit cells of the glide-symmetric pin-like media used in the artificial waveguide. The unit cell on the left hand side is for the guiding medium and the one on the right hand side is for the EBG. The unit cells are shown with the correct ratio to highlight the differences in their geometrical parameters.

Parametric Study of the EBG Unit Cell

The main target in design of EBG materials is to maximize their stopband. Therefore, a parametric study is performed on the unit cell shown in Fig. 4.2 to provide some guidelines on the design of the EBG medium. In the parametric studies the period is referred to simply as p instead of p_{guide} or p_{EBG}. The stopband is calculated from the full dispersion diagram of the 2-D periodic unit cell along the edges of the irreducible Brillouin zone determined by the ΓXM triangle shown in Fig. 4.2. The eigenmode solver of CST Microwave Studio is used to find the dispersion diagrams in this chapter [53]. The unit cell with $p = 3$ mm, $d = 0.8$ mm, $g = 0.25$ mm and $h = 1.2$ mm is taken as the reference case and its full dispersion diagram is shown in Fig. 4.3. The lower and higher limits of the stopband in this example are given by the second and third Bloch modes and are 40.624 GHz and 83.909 GHz respectively. Next, the effect of different parameters on the lower and higher limits of the stopband will be studied.

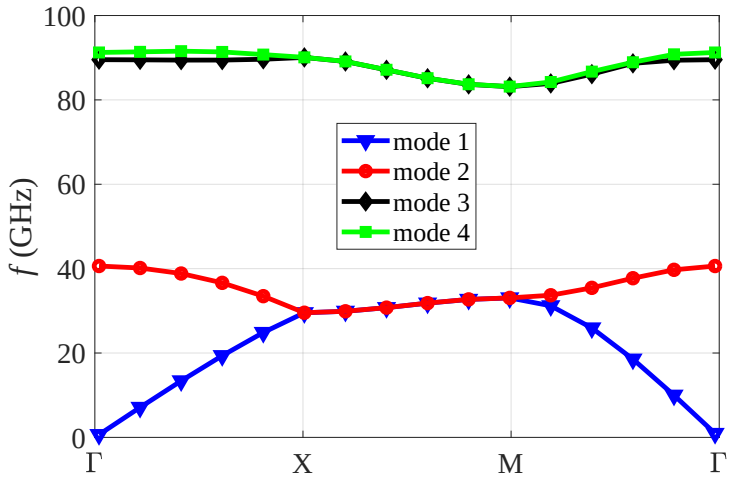

FIGURE 4.3: Full dispersion diagram of the unit cells shown in Fig. 4.2 with parameters $p = 3$ mm, $d = 0.8$ mm, $g = 0.25$ and $h = 1.2$ mm.

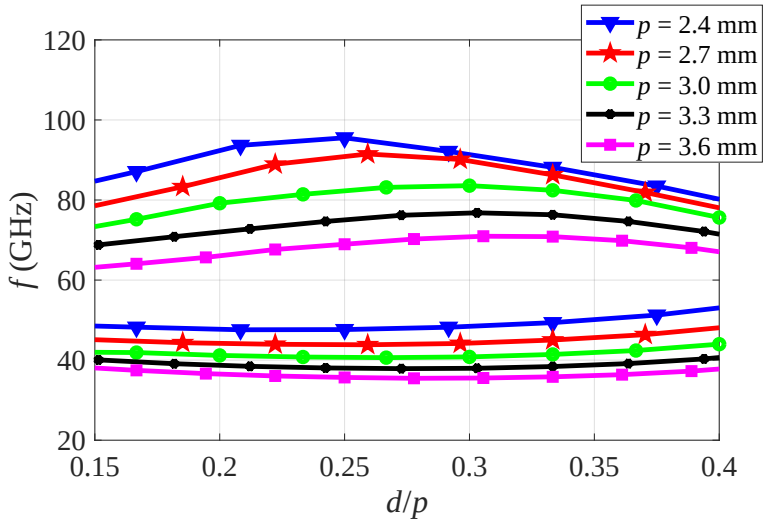

FIGURE 4.4: Effect of the ratio d/p in the unit cell of Fig. 4.2 on the lower and upper limits of the stop-band for a number of periods. Other geometrical parameters: g=0.25 mm and h=1.2 mm.

Fig. 4.4 depicts the lower and upper limits of the stopband versus the ratio d/p for a number of periods. Investigation of the results suggest that the change of d/p affects the upper limit more than the lower limit of the stopband. In addition, the bandwidth increases while increasing d/p up to a certain value and decreases after that value. Finally, it is observed that increasing the period p moves the stopband region to lower frequencies. To better visualize these findings, two new representation of the same results is given in the next two figures. Fig. 4.5 depicts the center frequency of the stopband versus d/p for a number of periods. This figure clearly displays how the period p affects the center frequency of the stopband. This is analogous

to photonic crystals where the periodicity controls the center of the stopband [1]. Fig. 4.6 plots the percentage of the stopband bandwidth around its center frequency for a number of periods. It shows that for each period there is a maximum for a particular value of d/p. This optimum occurs for d/p values between 0.25 and 0.3. For lower p, this optimum happens more towards $d/p = 0.25$ while for higher p, it occurs closer to the $d/p = 0.3$ value.

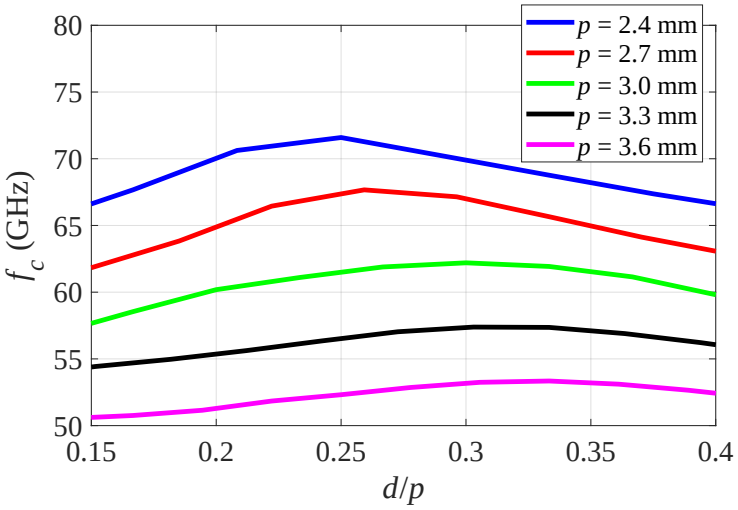

FIGURE 4.5: Effect of the ratio d/p in the unit cell of Fig. 4.2 on the center frequency of the stop-band f_c for a number of periods. Other geometrical parameters: g=0.25 mm and h=1.2 mm.

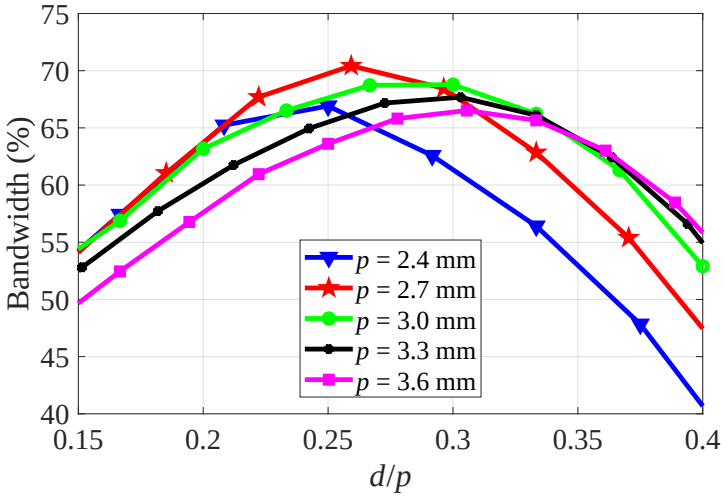

FIGURE 4.6: Effect of the ratio d/p in the unit cell of Fig. 4.2 on the percentage of stopband bandwidth around its center frequency f_c for a number of periods. Other geometrical parameters: g=0.25 mm and h=1.2 mm.

Next, the effect of the normalized gap size g/p is studied. Fig. 4.7 demonstrates the lower and upper limits of the stopband for several d/p. It is noticeable that the smaller the gap is, the wider the stopband becomes. This

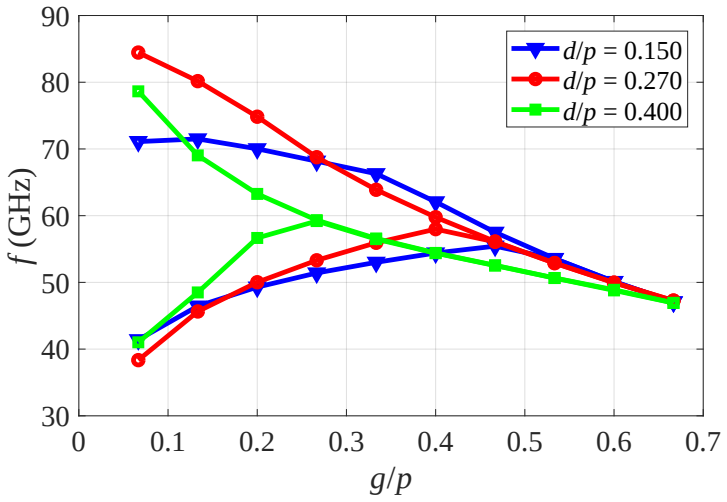

FIGURE 4.7: Effect of the normalized gap size g/p in the unit cell of Fig. 4.2 on the lower and upper limits of the stopband for a number of d/p ratios. Other geometrical parameters: p=3 mm and h=1.2 mm.

means that to have a better EBG with wider stopband, it is desirable to have the lowest gap possible between the parallel plates. Also, the figure shows that when then gap is larger than a particular value, the stopband no longer exists. This value is different for different d/p ratios and it is seen that it decreases as the d/p ratio increases meaning that for a higher filling factor (d/p ratio) a closer pin-plate configuration is necessary (the maximum g/p leading to a stopband is lower). Finally, it is noticeable that for any value of the normalized gap size g/p, the stopband corresponding to $d/p = 0.275$ is wider than those for $d/p = 0.15$ and $d/p = 0.4$ which is in accordance with the results obtained from Fig. 4.4.

Finally, the effect of the normalized pin height h/p is studied. Fig. 4.8 plots the lower and upper limits of the stopband versus h/p ratio for several values of d/p. It is observed that no stopband exists below a certain h/p value which means that a minimum pin height is needed to achieve a stopband. Furthermore, it is seen that increasing the h/p ratio decreases the lower stopband limit while the upper limit stays almost constant up to a certain h/p and decreases after. For higher values of h/p the slope of the decrease in the higher limit is steeper than that of the lower limit. This results in the stopband getting narrower. Therefore, an optimum stopband bandwidth is achieved at mid h/p range. To better visualize the changes in the bandwidth, the percentage of bandwidth around the center frequency of the stopband is plotted versus h/p in Fig. 4.9. It confirms that no stopband exists for low h/p values. Then by increasing h/p ratio, the stopband appears, gets wider and reaches a maximum for a certain h/p value.

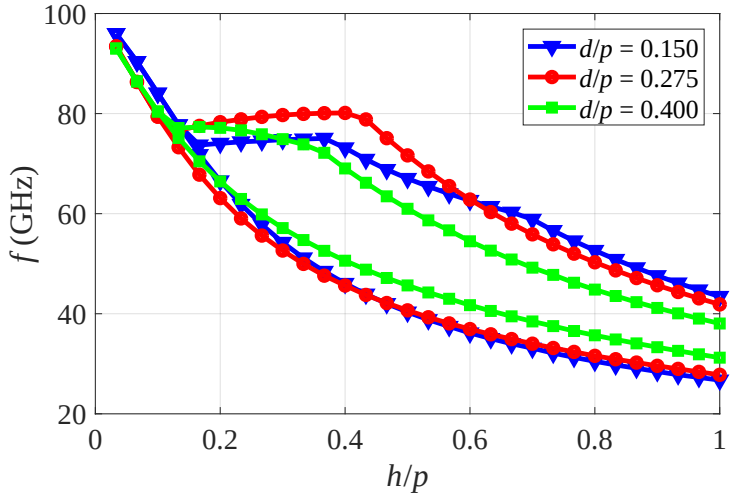

FIGURE 4.8: Effect of the normalized pin height h/p in the unit cell of Fig. 4.2 on the lower and upper limits of the stopband for a number of d/p ratios. Other geometrical parameters: $p =$ 3 mm and $g = 0.4$ mm.

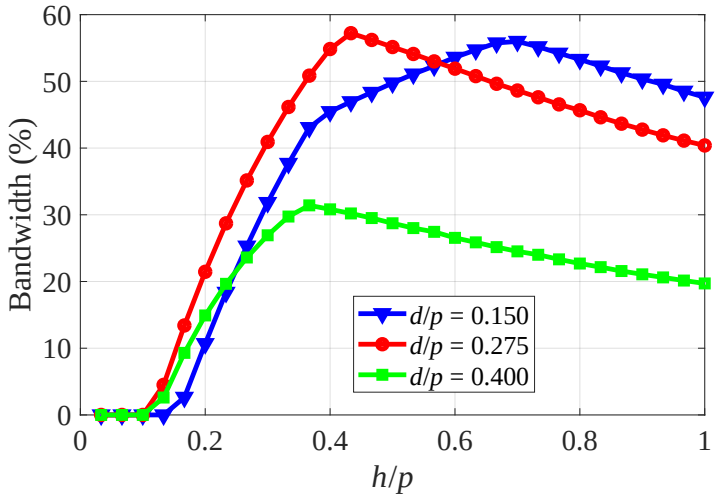

FIGURE 4.9: Effect of the normalized pin height h/p in the unit cell of Fig. 4.2 on the percentage of bandwidth of the stopband for a number of d/p ratios. Other geometrical parameters: $p =$ 3 mm and $g = 0.4$ mm.

The graphs and the discussions that were presented in these parametric studies can be used as guidelines for design of an EBG material using glide-symmetric pin-like medium. For instance, to design an EBG material with near optimum stopband bandwidth, one can choose an arbitrary period p. Then Figs. 4.4 and 4.6 suggest that a $d/p = 0.275$ ratio provides a near optimum design to maximize the stopband bandwidth. Therefore, d is chosen accordingly. Next, Fig. 4.7 shows that the lower the gap size g, the larger the stopband is. Hence, the lowest possible g based on the design requirements is chosen. After that, a $h/p = 0.5$ ratio can be chosen as an initial value for

the pin height while this parameter can be tuned for maximum bandwidth. Finally, if the center frequency of the designed stopband is different from the desired center frequency, all the parameters can be scaled to scale the dispersion diagram along the frequency axis.

The "on" State

The first step in design is the "on" state of the waveguide. In this state, the guiding medium needs to be designed to be in its pass-band, while the EBG needs to be in its stop-band to attenuate the fields outside the guiding medium. It was shown in Fig. 4.5 that modifying the period modifies the center frequency of the stopband. Therefore, choosing two periodic media that only differ in their period can produce two media with shifted stopbands that can be used as EBG and guiding medium. An EBG and a guiding medium are designed with this strategy. Fig. 4.10 plots the full dispersion diagrams of their unit cells that were shown in Fig. 4.2. The geometrical parameters of the guiding medium are $p_{\text{guide}} = 1.5$ mm, $h = 1.2$ mm, $d = 0.5$ mm and $g = 0.25$ mm. The parameters for EBG unit cell are $p_{\text{EBG}} = 3$ mm, $h = 1.2$ mm, $d = 0.5$ mm and $g = 0.25$ mm. The potential operating frequency range is highlighted by an orange rectangle in Fig. 4.10 and covers the 42-71 GHz bandwidth. Indeed, within this range, the guiding medium exhibits a linear-frequency-dependent propagation constant and the EBG medium exhibits a bandgap. The field can therefore propagate while being confined with no dispersion.

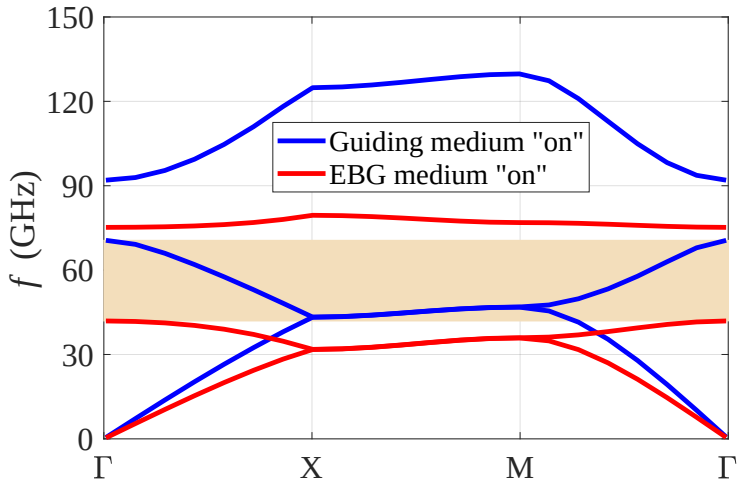

FIGURE 4.10: Full dispersion diagram of the structure with the unit cells shown in Fig. 4.2 in the "on" state. Geometrical parameters of the guiding medium and EBG: $d = 0.5$ mm, $h = 1.2$ mm and $g = 0.25$ mm, $p_{\text{guide}} = 1.5$ mm and $p_{\text{EBG}} = 3$ mm.

Two-State Reconfigurability

The next step is to realize a transition from the "on" (or propagating) state to an "off" (or attenuating) state. In the "off" state, both the EBG and the guiding medium should still present stop-band characteristics within the waveguide's operating frequency range. This prevents any wave propagation in the longitudinal direction of the waveguide and ensures attenuation of the fields in all directions.

To achieve such a transition from the "on" to the "off" state, the contactless configuration of the structure is employed. Such configuration allows for adjusting the distance between the two plates. Next, the effect of variation in the parameter g of the unit cells shown in Fig. 4.2, i.e. the distance between the top of a pin and the opposite metallic plate is investigated again to prove that it provides a meaningful way to control the transition from the "on" to the "off" state. The distance can be easily controlled by moving the two metallic plates either closer to or further away from each other. Since no deformation occurs in the plates, both unit cells should be modified with the same Δg variation.

Fig. 4.11 (a) depicts the full dispersion diagrams of the guiding medium when varying the gap g of $\Delta g = 0.15$ mm. The two different gaps are $g_{\text{off}} = 0.1$ mm and $g_{\text{on}} = 0.25$ mm. Similar to Fig. 4.7, we notice that by decreasing the gap g, the stop-band of the guiding medium is increased around its center frequency. Hence, part of the frequency region that was highlighted in Fig. 4.10 with an orange rectangle now passes from an "on" state (pass-band) to an "off" state (stop-band). This frequency range which covers $54 - 71$ GHz is shown by a gray rectangle. The operating frequencies of the waveguide is given by the intersection of the orange rectangle in Fig. 4.10 and the gray rectangle in Fig. 4.11 which results in the gray rectangle.

Next, the same gap variation $\Delta g = 0.15$ mm is investigated on the EBG (varying the gap from $g_{\text{on}} = 0.25$ mm to $g_{\text{off}} = 0.1$ mm). Fig. 4.11 (b) displays the full dispersion diagrams of the EBG medium for the two aforementioned gap sizes. Similar to the guiding medium, it is observed that the smaller the gap gets, the wider the stop-band becomes and the material still behaves as an EBG in the gray-shaded frequency range. Therefore, both the guiding medium and the EBG medium attenuate the fields with the smaller gap $g = 0.1$ mm and the design of the "off" state is complete.

4.2.2 Feeding Mechanism and Impedance Matching

To complete the design, a proper feeding mechanism along with a working impedance matching is necessary. Fig. 4.12 (a) shows a perspective view of our waveguide including the feeding part and the impedance matching. A standard rectangular waveguide feed with dimensions of 3.7592 mm $\times$ 1.8796 mm (a standard WR-15 for V band) is used to excite the structure from the bottom. The excitation accesses are indicated by black arrows. Fig. 4.12 (b) displays a top view of the waveguide while the upper plate is removed for a clear visualisation of the pins. While gray squares are pins on the bottom

plate, white squares stand for the pins on the upper plate, removed from the picture.

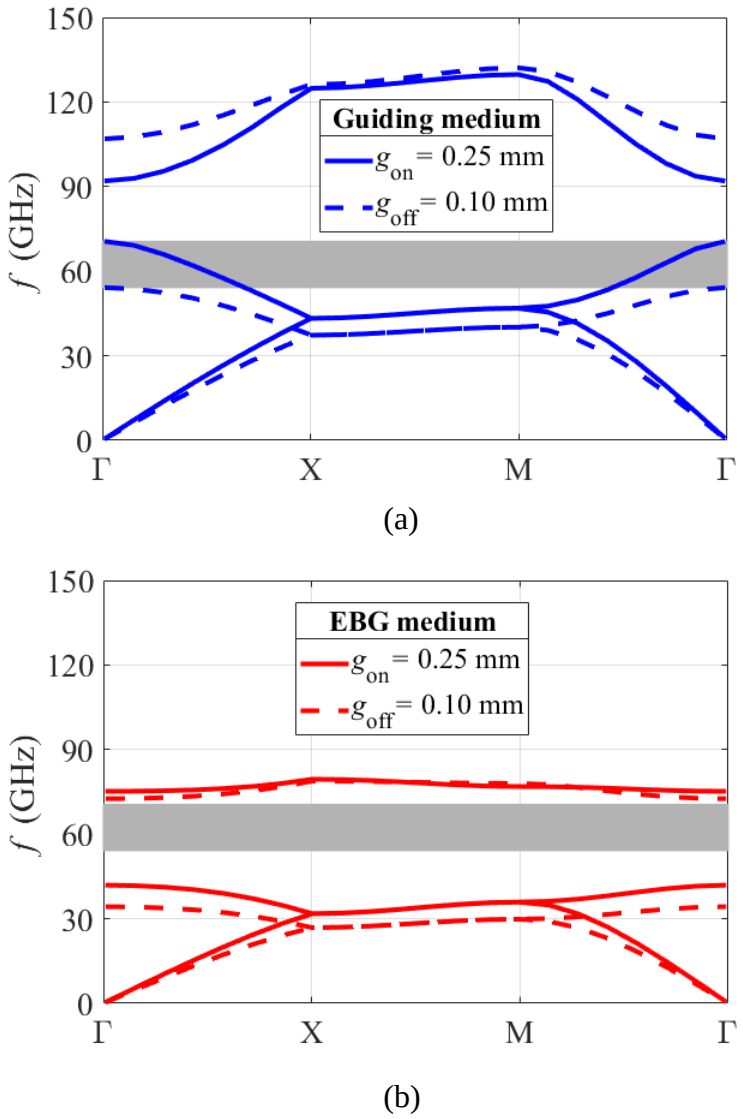

FIGURE 4.11: Full dispersion diagram of the unit cell shown in Fig. 4.2 (a) for two values of $g = 0.1$ mm (off state) and $g = 0.25$ mm (on state) in the guiding medium with geometrical parameters: $d = 0.5$ mm, $h = 1.2$ mm and $p_{\text{guide}} = 1.5$ mm (b) for two values of $g = 0.1$ mm (off state) and $g = 0.25$ mm (on state) in the EBG medium with geometrical parameters $d = 0.5$ mm, $h = 1.2$ mm and $p_{\text{EBG}} = 3$ mm.

The waveguide can be divided into 3 sections: the guiding section in the middle and two matching sections at both ends of the longitudinal x direction. Each matching section includes the feeding slot and the required tapering for a smooth transition. The guiding section and one of the two matching sections are shown in Fig. 4.12 (b).

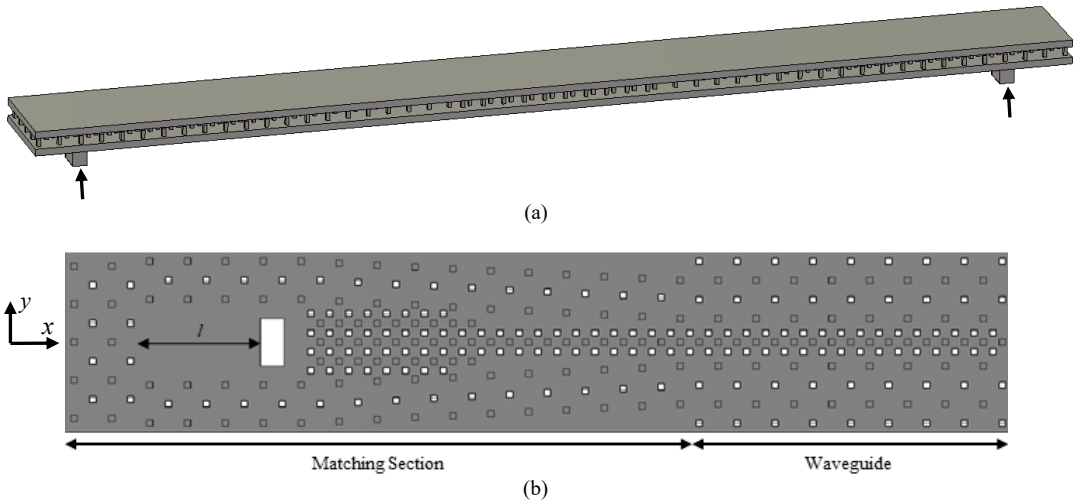

FIGURE 4.12: The designed artificial waveguide: (a) perspective view (b) the top view cut in half along the longitudinal direction and with the top metal plate removed for better visualisation of the inner parts.

To better visualize the matching section, it is divided into two smaller subsections that are shown in Figs. 4.13 (a) and (b). Fig. 4.13 (a) includes the feeding slot at a distance l from the EBG at one end of the structure. With a proper choice of l, the EBG medium reflects the wave from the feed towards the waveguide. In Fig. 4.13 (b) the required matching tapering is shown. Two types of tapering are used. Firstly, since the guiding medium in the guiding section of Fig. 4.12 (b) has a different width from the subsection shown in Fig 4.13 (a), a width tapering of the guiding medium is applied. For instance, in the structure shown in Fig. 4.12 (b), the width of the guiding medium is larger at the end of the matching section than the guiding section in the middle of the waveguide. Therefore, as it is displayed in Fig. 4.13 (b), the width of the guiding medium is tapered from narrow to wide. This is done by slowly pushing the two side EBG media further away from each other. Furthermore, it should be noted that as the width increases, extra rows of pins are inserted into the guiding medium to completely fill that region. The second type of tapering that we use in our designs is the tapering of the pin height. The pin height can start from low and smoothly increase to the final pin height that is used in the guiding section of the artificial waveguide. These two types of tapering will provide a smooth transition in the guiding medium and therefore prevent undesired reflection of the electromagnetic wave due to abrupt changes in the guiding medium.

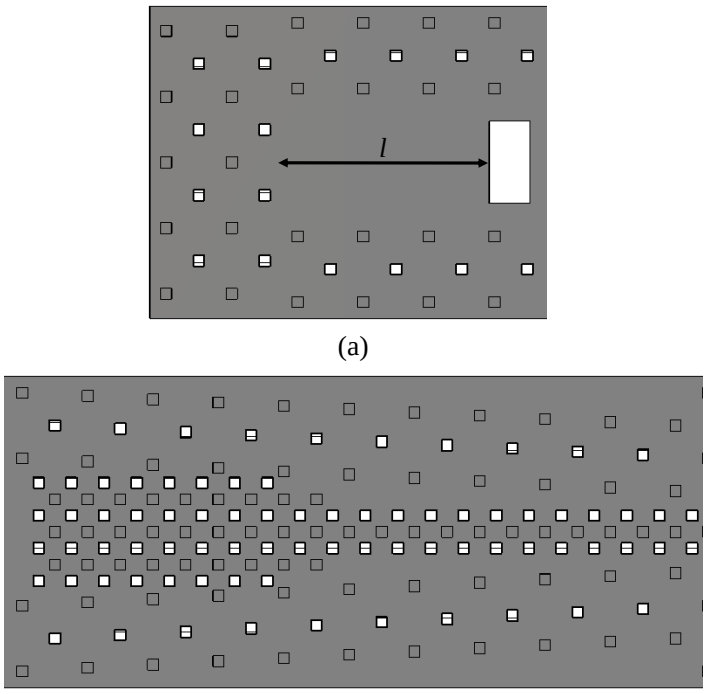

FIGURE 4.13: The top view of (a) the first subsection of the matching that includes the rectangular feed (the top metal plate is removed). (b) the second subsection of the matching that includes the tapering of pin height and width of the guiding medium (the top metal plate is removed).

4.2.3 Simulation Results

In this subsection, the simulation results of the waveguide designed in previous subsections are studied and discussed. It is recalled that the guiding medium is a periodic structure with a unit cell shown in Fig. 4.2 and parameters $h = 1.2$ mm, $d = 0.5$ mm, $g = 0.25$ mm and period $p_{\text{guide}} = 1.5$ mm. The EBG medium has the same structure with the only difference of a higher period $p_{\text{EBG}} = 3$ mm. In Fig. 4.13 (b), it is seen that we chose 3 rows of pins in the guiding medium. This corresponds to a width of $1.5 \times p_{\text{guide}}$ which equals 2.25 mm. At the end of the waveguide, the width of the guiding medium should be larger than the length of the WR-15 rectangular waveguide feed. Thus, the minimum number of pin rows that qualifies is 7. Hence, the width of the guiding medium at the end of the waveguide is set to $3.5 \times p_{\text{guide}}$ or equally 5.25 mm. This means that a width tapering is required to eliminate the width difference of the guiding medium in different sections of the structure. A 10-step linear width tapering is applied to the structure. Therefore, the width difference from one step to the next is always the same. This part of the matching section is therefore $10 \times p_{\text{EBG}} = 30$ mm long. In addition to width tapering, a 20-step linear pin height tapering is applied to the guiding medium. The length of this tapering is $20 \times p_{\text{guide}} = 30$ mm and therefore it does not add to the length of the matching. This is due

to the fact that both the pin height tapering and the guide width tapering are applied over the same length as it was already shown in Fig. 4.13 (b). The EBG media surrounding the waveguide are chosen to have a width of $1.5 \times p_{\text{EBG}} = 4.5$ mm. This corresponds to 3 rows of pins in the EBG medium. Furthermore, we found that the distance l which provides the best matching bandwidth is 2.5 mm.

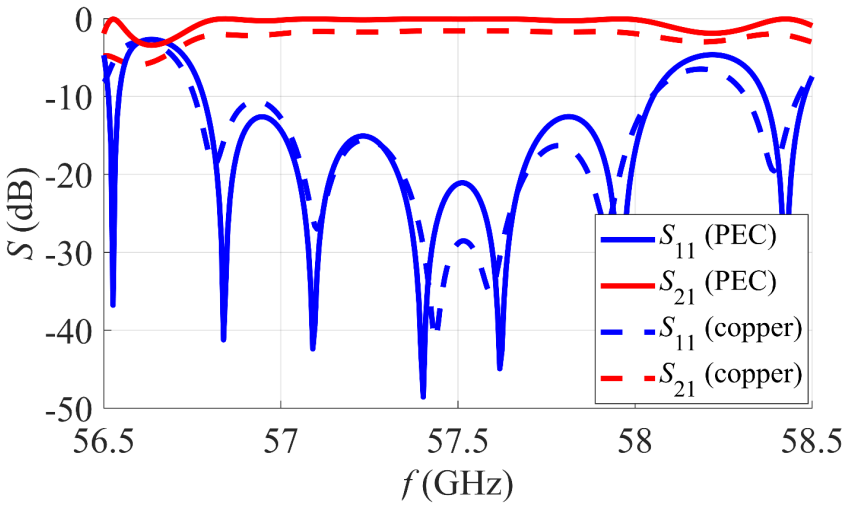

FIGURE 4.14: Scattering parameters of the structure shown in Fig. 4.12 simulated with PEC and copper in the "on" state. Geometrical parameters: $l = 2.5$ mm $d = 0.5$ mm, $h = 1.2$ mm, $g = 0.25$ mm, $p_{\text{guide}} = 1.5$ mm and $p_{\text{EBG}} = 3$ mm.

Fig. 4.14 plots the scattering parameter results from the simulation of the designed waveguide with the aforementioned geometrical parameters. Two simulations have been carried out: one with perfect electric conductor (PEC) and the other with copper (a lossy metal) in the structure. Both results are shown in the figure. The simulation results with PEC are shown in solid lines. The S_{11} curve displays a -10 dB impedance matching bandwidth of 1.26 GHz around the center frequency of 57.42 GHz. The S_{21} curve confirms the full transmission of power from the first waveguide port at one end to the waveguide port at the other end of the guide. The simulation results using copper are shown in dashed lines. These results clarify the effect of introducing a metal loss in the structure. We observe from the S_{11} result that the structure with copper still provides the same -10 dB bandwidth as the structure with PEC. The S_{21} curve, however, displays a drop of more than 1.5 dB compared to the structure with PEC which corresponds to 0.053 dB/wavelength at the center frequency. This emphasizes that the power loss due to the ohmic losses in metal can be significant for long waveguides. In the simulated waveguide, the length of the structure was approximately 29 times the wavelength at the center frequency and the length of each matching section is approximately 11.5 times the wavelength of the wave at the center frequency. Therefore, the matching sections are very large and they need to be minimized. Even though this design verifies the possibility of implementing reconfigurability

in the propagation of the waves using the proposed technology, the characteristics of the design need further improvements to justify the use of such technology. The next section focuses on improving the current design.

4.3 The Improved Reconfigurable Waveguide

We start this section by enumerating the shortcomings of the artificial waveguide designed in the previous section. First, even though a working matched bandwidth was achieved, the bandwidth was very narrow. It would be beneficial to have a waveguide with a wider working bandwidth. Secondly, the insertion losses due to the metal was not negligible. This makes the longer versions of the design inefficient. A new design with less insertion loss due to the lossy metal is desirable. Finally, the size of the matching sections was not large. This leads to extra losses while making the structure less practical and compact. Therefore, a new design with much smaller matching sections is desired. In the next subsections, these needs are addressed with proposition of a modified design.

To overcome the shortcomings of the previous design, two modifications are applied to the waveguide structure. It will be shown later that these modifications improve the performance and practicality of the design.

4.3.1 Modifications of the guiding medium

The first modification is applied to the unit cell of the guiding medium. In the previous design the gap g was very small and the pins were very long. In fact, the pins on the two opposite plates protruded through the vertical mid-plane. In order to improve our design, we choose a new unit cell for the guiding medium, whose geometry is closer to the free-space PPW and then easier to match. In this new unit cell, we use shorter pins which leave an empty space between the pins on the opposite plates. This modification is shown in Fig. 4.15 in which the unit cell shown in Fig. 4.15 (a) displays the one used in the previous design and the unit cell in Fig. 4.15 (b) exhibits the new one for which the gap g is increased and the pin height h is decreased while the sum $g + h$ was kept the same as that in Fig. 4.15 (a).

By decreasing the pin height in the new unit cell, we decrease the lateral surfaces of the metallic pins. We predict that with this modification the electromagnetic wave will now propagate mostly in the air gap between the top and bottom pins. Hence, we expect that metal losses will decrease in the new format. The second prediction concerns the cross-sectional field distribution of the propagating waves. We predict that as the pins get smaller, they will cause less perturbation in the modal fields of the rectangular waveguide. We expect that smaller perturbation of the modal fields may lead to a larger matched bandwidth for the structure. This also helps reduce the size of the matching section as the smaller pins need less or no height tapering steps.

The chosen parameters for the new unit cells in the "on" state are $g = 0.9$ mm, $h_{\text{guide}} = 0.2$ mm, $d_{guide=}0.4$ mm and $p_{\text{guide}} = 1.5$ mm.

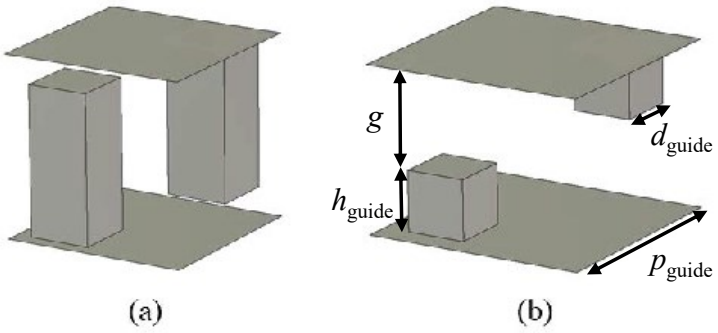

FIGURE 4.15: Unit cell of the guiding medium in the "on" state: (a) initial waveguide presented in sec. 4.2.1 (b) modified waveguide presented in sec. 4.3

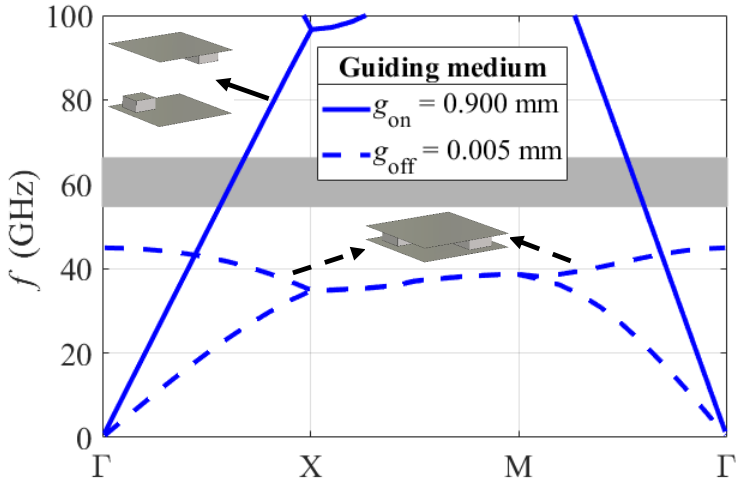

FIGURE 4.16: Full dispersion diagram of the unit cell shown in Fig. 4.15 (b) for two values of $g = 0.005$ mm (off state) and $g = 0.9$ mm (on state) in the guiding medium with geometrical parameters: $d_{guide} = 0.4$ mm, $h_{guide} = 0.2$ mm and $p_{guide} = 1.5$ mm.

To study the transition of the new guiding medium from the "on" to the "off" state, its full dispersion diagrams in the two states are shown next to each other in Fig. 4.16. The gray rectangle refer to the final operational band of the complete structure and will be commented later. It is interesting to note the difference between the guiding medium that was discussed in Sec. 4.2.1 and the one discussed in this section in their "on" state. In the former, the potential operating frequency region (shown by the orange rectangle in Fig. 4.10) belonged to frequencies at the end of the first passband and therefore in proximity to the first stopband. In that case, a small change in the gap g (from $g_{on} = 0.25$ mm to $g_{off} = 0.10$ mm, $\Delta g = 0.15$ mm) could move the stopband edge and transform a passband regime into a stopband one. In the new unit cell "on" state, however, we do not operate close to a stopband

edge. To create the stopband, a larger change of the gap g is required (from $g_{on} = 0.09$ mm to $g_{off} = 0.005$ mm, $\Delta g = 0.085$ mm).

4.3.2 Modifications of the EBG medium

Fig. 4.16 showed that the new guiding medium can be used to reconfigure the structure between the states. However, this new design creates a new challenge. The new design requires a gap variation of $\Delta g = 0.895$ mm while the previous design required a $\Delta g = 0.15$ mm. This requires a new EBG design. The EBG in Fig. 4.2 has a gap equal to $g = 0.25$ mm in the "on" state and the change of $\Delta g = 0.895$ mm is not possible for such a medium: the pins would touch the opposite plates before the full variation occurred. A new EBG medium design is required having a gap g larger than 0.895 mm. This is why a new EBG unit cell is designed with parameters $g = 0.9$ mm, $h_{EBG} = 1.2$ mm, $d_{EBG} = 0.8$ mm and $p_{EBG} = 3$ mm and is shown in Fig. 4.17 (a). Here, the only difference between the new and old EBG is a larger gap g of 0.9 mm in the new design. The old EBG is shown in Fig. 4.17 (b) for the sake of comparison.

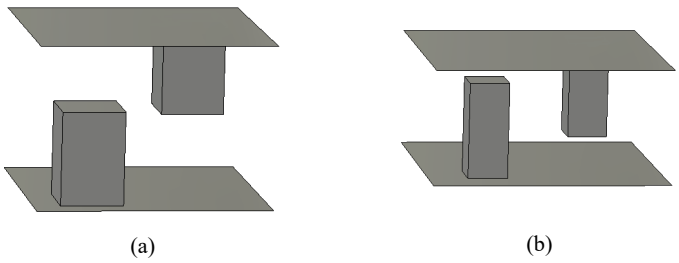

FIGURE 4.17: (a) Unit cell of the EBG media of the modified waveguide presented in sec. 4.3 (b) Unit cell of the EBG media of the initial waveguide presented in sec. 4.2.1. The unit cells are shown with the correct ratio to highlight the differences in their geometrical parameters.

Fig. 4.18 displays the unit cells of the EBG and the guiding media in the modified waveguide next to each other. The full dispersion diagram of the new EBG unit cell is shown in Fig. 4.19. The gray region of frequencies covers the whole stopband of the new EBG in the "on" state, and it is the same shown in Fig. 4.16. To confirm the effectiveness of the EBG design in the "off" state, we have also plotted the dispersion diagram of this unit cell when its gap g decreases to 0.005 mm. The new curve proves that the width of the stopband increases and the structure stays a good EBG in our desired frequencies. The two curves show that the EBG medium works as expected while the structure is reconfigured.

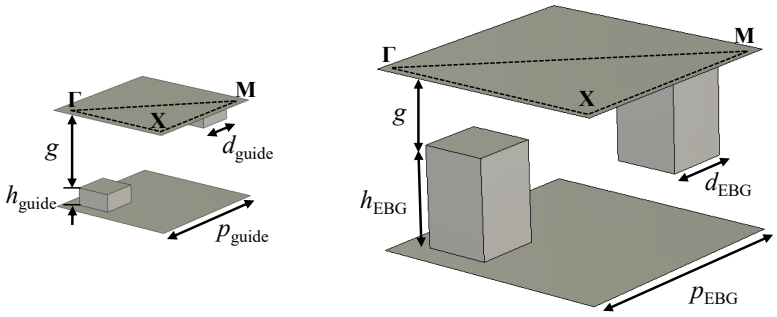

FIGURE 4.18: Unit cells of the glide-symmetric pin-like media used in the modified artificial waveguide presented in sec. 4.3. The unit cell on the left hand side is for the guiding medium and the one on the right hand side is for the EBG. The unit cells are shown with the correct ratio to highlight the differences in their geometrical parameters.

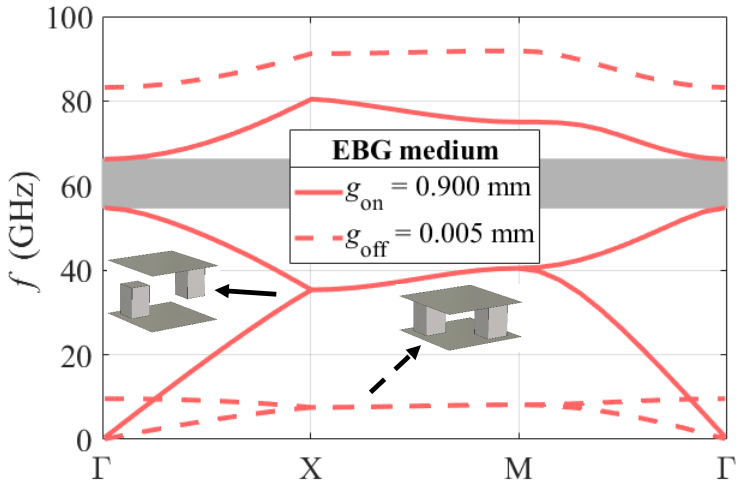

FIGURE 4.19: Full dispersion diagram of the unit cell shown in Fig. 4.18 (b) for two values of $g = 0.005$ mm (off state) and $g = 0.9$ mm (on state) in the EBG medium with geometrical parameters $d_{EBG} = 0.8$ mm, $h_{EBG} = 1.2$ mm and $p_{EBG} = 3$ mm.

It is interesting to compare the EBG medium in this new waveguide design with the previous one in terms of their attenuation characteristics. To do so, Fig. 4.20 plots the normalized attenuation constant versus frequency for the two EBG media and for different values of transversal phase shift $k_y p = 0$, $k_y p = \pi/2$ and $k_y p = \pi$. The results are calculated by the multimodal T-matrix method developed in Ch. 3. It was discussed there that an advantage of the method is the calculation of the attenuation constant in addition to the propagation constant of the wave. The attenuation constant of an EBG in its stopband is an important value since it clarifies how strongly the EBG attenuates the unwanted electromagnetic fields.

The first noticeable difference between the two EBG media is the decreased stopband width in the new EBG. This was already expected from

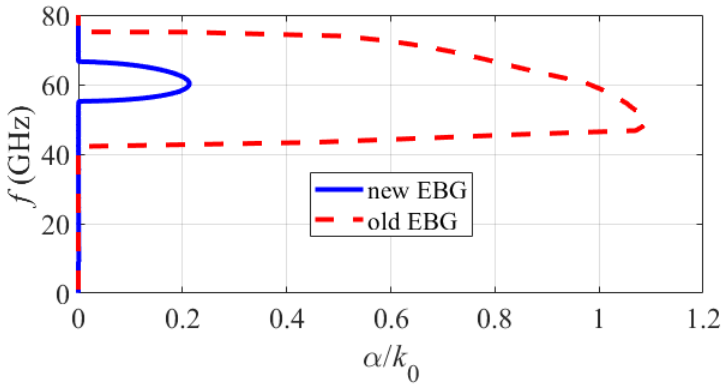

(a)

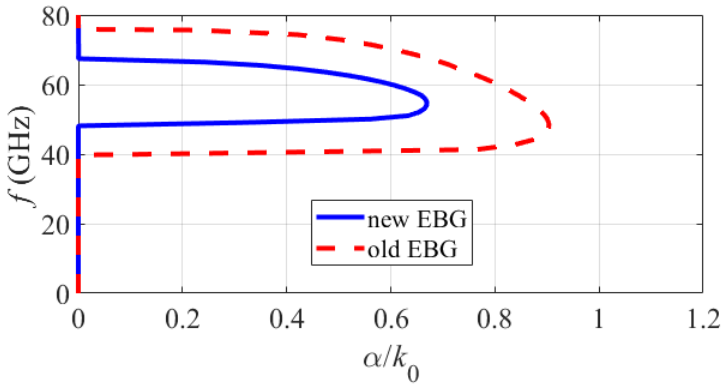

(b)

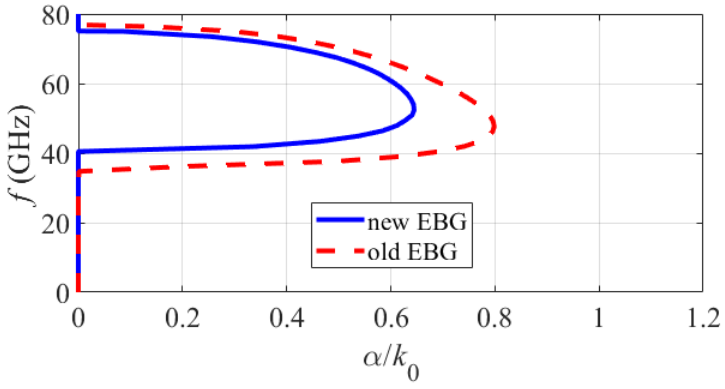

(c)

FIGURE 4.20: Normalized attenuation constant α/k_0 vs. frequency for the EBG media designed for the two proposed waveguides in this chapter with (a) $k_y p = 0$, (a) $k_y p = \pi/2$ and (c) $k_y p = \pi$. The "on" state of the waveguides are considered. Geometrical parameters of the old EBG: $p_{\text{EBG}} = 3$ mm, $d_{\text{EBG}} = 0.5$ mm, $h_{\text{EBG}} = 1.2$ mm and $g_{\text{EBG}} = 0.25$ mm. Geometrical parameters of the new EBG: $p_{\text{EBG}} = 3$ mm, $d_{\text{EBG}} = 0.8$ mm, $h_{\text{EBG}} = 1.2$ mm and $g_{\text{EBG}} = 0.9$ mm.

the findings of Fig. 4.7 which predicts a smaller stopband width when the gap g increases while keeping the other parameters constant. However, the very large stopband of the old EBG was not used, since the final matched frequency range was much smaller than the EBG's stopband width. Therefore, loosing part of the EBG bandwidth with the aim of improving the matching bandwidth is considered acceptable. It is also interesting to note from Fig. 4.20 (a) that the normalized attenuation constant has been approximately divided by 5 around 60 GHz when $k_y p = 0$. The decrease in normalized attenuation constant is also observed for $k_y p = \pi/2$ and $k_y p = \pi$ even though the decrease is not as much as for $k_y p = 0$. These results mean that the modifications to improve the matching bandwidth lead to a weaker EBG. This may lead to a wider EBG region around the guiding medium necessary in order to achieve a good isolation if adjacent lines are present. However, this is an acceptable downside if the operational bandwidth of the waveguide improves dramatically. A discussion on the isolation between two adjacent guides will be proposed after presenting the complete design.

4.3.3 The Final Structure

Fig. 4.21 (a) shows a perspective view of the modified waveguide structure. It is important to notice the height difference between the guiding medium and the EBG medium. This is because the distance between the two parallel plates is no more the same in the new design. While in the previous design the same distance between the plates defined a flat plane in the entire structure, here, we keep the bottom plate flat, and on the top plate a step is created to tune the correct PPW distance according to the guiding/EBG region. The feeding component is still attached to the bottom plate. Fig. 4.21 (b) displays the top view of the same structure while removing the top plates. Gray squares are pins on the bottom plate and white squares are the pins locations on the upper plate, removed from the picture. It is interesting to compare the matching section of this structure with respect to the one of the previous structure (Fig 4.21). The lack of tapering of the width of the guiding medium and of the pin heights makes the matching section of this new structure much shorter. The excitation is applied through a rectangular waveguide feed the same way as before. The rectangular-waveguide feeding ports are displayed with black arrows.

7 rows of pins have been used in the guiding medium. This corresponds to a width of $3.5 \times p_{\text{guide}}$ which equals 5.25 mm and is slightly wider than the length of the rectangular waveguide feed. We have used a width of $1.5 \times p_{\text{EBG}} = 4.5$ mm for the EBG regions surrounding the waveguide. The length of the structure is 25.5 mm. Furthermore, we empirically found that the distance $l = 3.4\ mm$ provides the best matching bandwidth.

4.3.4 Simulation Results

In this section, the simulation results of the final reconfigurable waveguide is studied. These simulations are operated for the two cases of single and

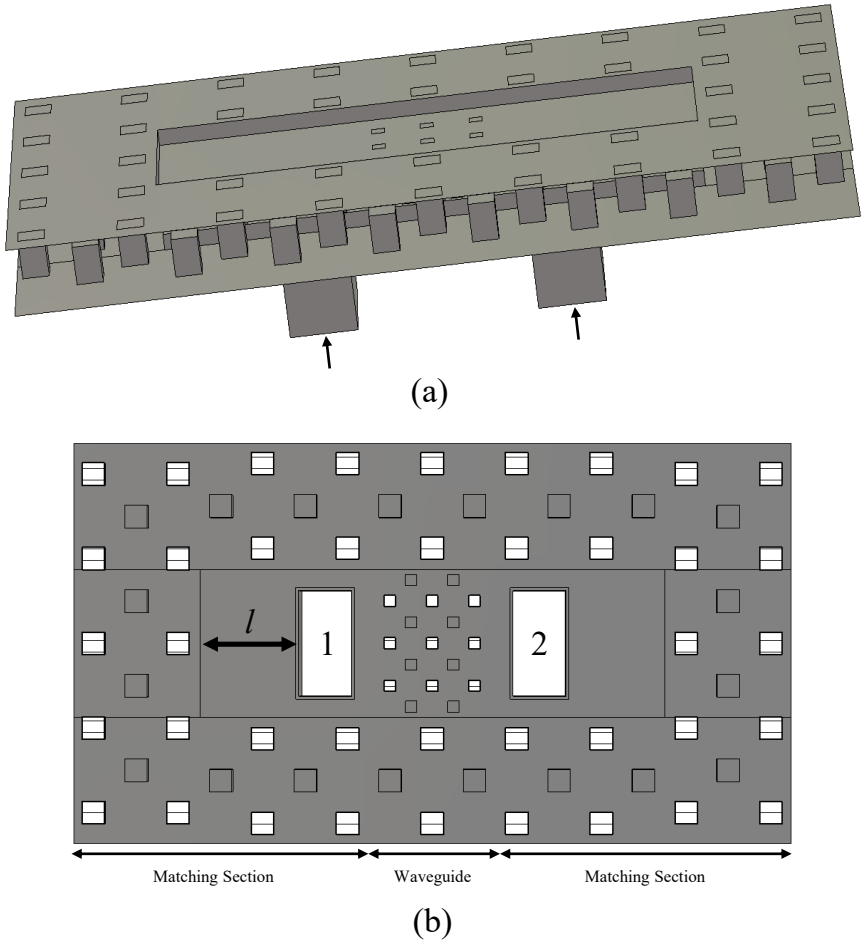

FIGURE 4.21: The designed artificial waveguide: (a) perspective view (b) the top view with the top metal plate removed for better visualisation of the inner parts.

double waveguides. At first, the scattering parameters of a single waveguide are studied to determine the matched bandwidth of the design. Then the more specific case of two adjacent waveguides is considered to investigate the correct operation of the designed waveguide. Moreover, the coupling between the two waveguides is discussed and the required precision of the mechanical adjustment for achieving the reconfigurability is studied.

Single Waveguide

Fig. 4.22 plots the simulated scattering parameters for the modified waveguide with its aforementioned geometrical parameters and the gap $g = g_{\text{on}} =$ 0.9 mm (the "on" state discussed in the previous section). The simulations are performed with both PEC and copper as the structure's material to again observe the losses due to the lossy metal. Looking at the simulation results with PEC, the S_{11} curve displays a -10 dB impedance matching bandwidth of 5.7 GHz between the frequencies $f_{min} = 57.1$ GHz and $f_{max} = 62.8$ GHz. This shows a great improvement from the matched bandwidth of 1.26 GHz in the initial design of the waveguide which was investigated in Sec. 4.2.3.

The S_{21} curve confirms the full transmission from the first waveguide port at one end to the waveguide port at the other end of the guide. S_{21} levels are above -4 dB in the entire -10 dB impedance matching bandwidth. If S_{21} levels of higher than -0.7 dB are required, the bandwidth reduces to 5 GHz between $f_{min} = 57.1$ GHz and $f_{max} = 62.1$ GHz.

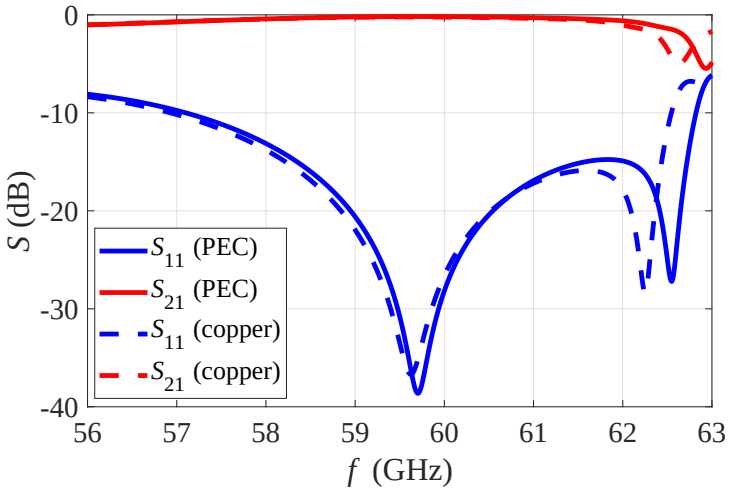

FIGURE 4.22: Scattering parameters of the structure shown in Fig. 4.21 in the "on" state. Geometrical parameters: $l = 3.4$ mm, $p_{\text{guide}} = 1.5$ mm, $h_{\text{guide}} = 0.2$ mm $d_{\text{guide}} = 0.4$ mm, $p_{\text{EBG}} = 3$ mm, $h_{\text{EBG}} = 1.2$ mm $d_{\text{EBG}} = 0.8$ mm, $g = 0.9$ mm.

Copper and PEC results shows a close match between them. The matched bandwidth is moved 0.3 GHz toward lower frequencies when using copper. It is observed that S_{21} levels drops less than 0.05 dB for the structure with copper compared to the structure with PEC and it corresponds to a loss of 0.009 dB/wavelength at the center frequency. Therefore, the losses are strongly reduced with respect to the previous design where the losses were at 0.26 dB/wavelength. It is good to note that the length of the new structure is approximately 5 times the wavelength of an electromagnetic wave in free space at the center frequency of its operating bandwidth. To observe the linear response of the structure, Fig. 4.23 plots the phase of S_{21} versus frequency. From the figure, it is clearly seen that the phase is linear in the aforementioned bandwidth, which is typical of waveguides realized with glide-symmetric geometries.

Next, the "off" state of the waveguide is studied. Fig. 4.24 displays the S parameter results of the structure in Fig. 4.18 when the gap $g = g_{\text{off}} = 0.005$ mm is considered. The result shows an insertion loss higher than 68 dB. Therefore, this waveguide can implement a switch with satisfactorily high isolation levels.

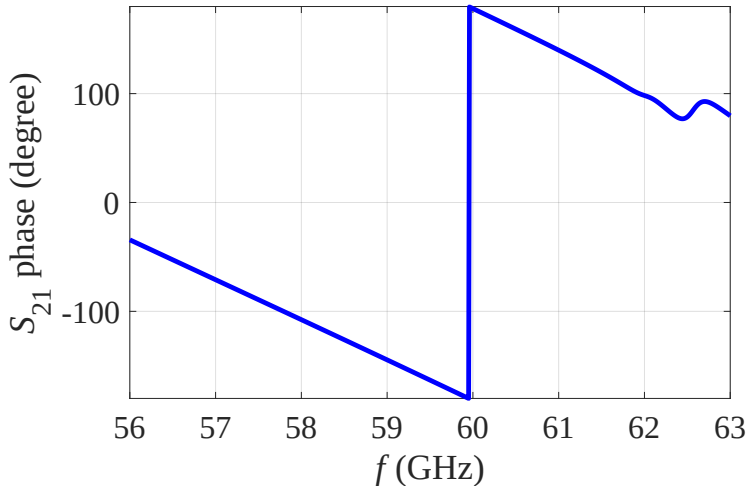

FIGURE 4.23: Phase of S_{21} versus frequency for the structure shown in Fig. 4.21 in the "on" state. Geometrical parameters: $l = 3.4$ mm, $p_{\text{guide}} = 1.5$ mm, $h_{\text{guide}} = 0.2$ mm $d_{\text{guide}} = 0.4$ mm, $p_{\text{EBG}} = 3$ mm, $h_{\text{EBG}} = 1.2$ mm $d_{\text{EBG}} = 0.8$ mm, $g = 0.9$ mm.

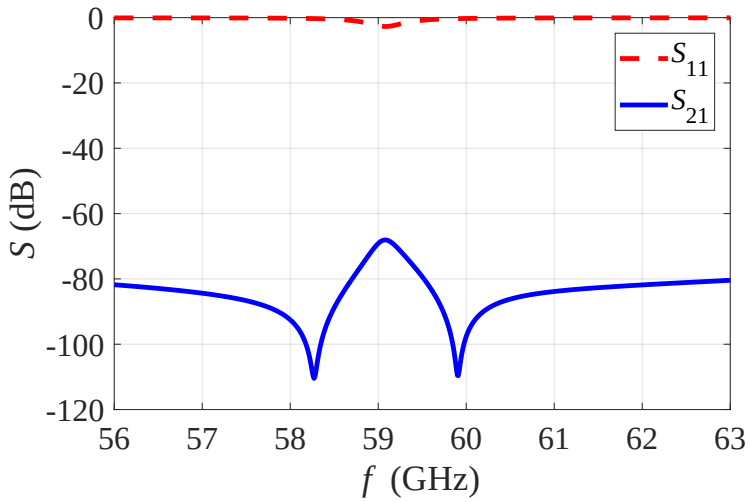

FIGURE 4.24: Scattering parameters of the structure shown in Fig. 4.21 in the "off" state. Geometrical parameters: $l = 3.4$ mm, $p_{\text{guide}} = 1.5$ mm, $h_{\text{guide}} = 0.2$ mm $d_{\text{guide}} = 0.4$ mm, $p_{\text{EBG}} = 3$ mm, $h_{\text{EBG}} = 1.2$ mm $d_{\text{EBG}} = 0.8$ mm, $g = 0.005$ mm.

An important factor in the designed technology is the precision of the mechanical adjustments needed to achieve reconfigurability. To recognize the required precision, sensitivity of the design to changes in the gap g is studied. Fig. 4.25 (a) depicts S_{11} results for the structure shown in Fig. 4.18 with $g = 0.9$ mm in the "on" state and compares it to the two cases for which there is a $\Delta g = \pm 0.05$ mm difference. The results confirm that a change of this magnitude does not deteriorate the bandwidth by much. In fact, it only moves the -10 dB bandwidth to slightly higher or lower frequencies in each case. Fig. 4.25 (b) plots S_{21} results for the same structure with $g = 0.005$ mm

in the "off" state and compares it to $g = 0.008$ mm and $g = 0.009$ mm. Here, we observe that the gap change of $\Delta g = +0.003$ mm does not prevent the "off" state operation, since $|S_{21}|$ stays below -40 dB after this change. The gap change of $\Delta g = +0.004$ mm provides S_{21} levels that are lower than -20 dB.

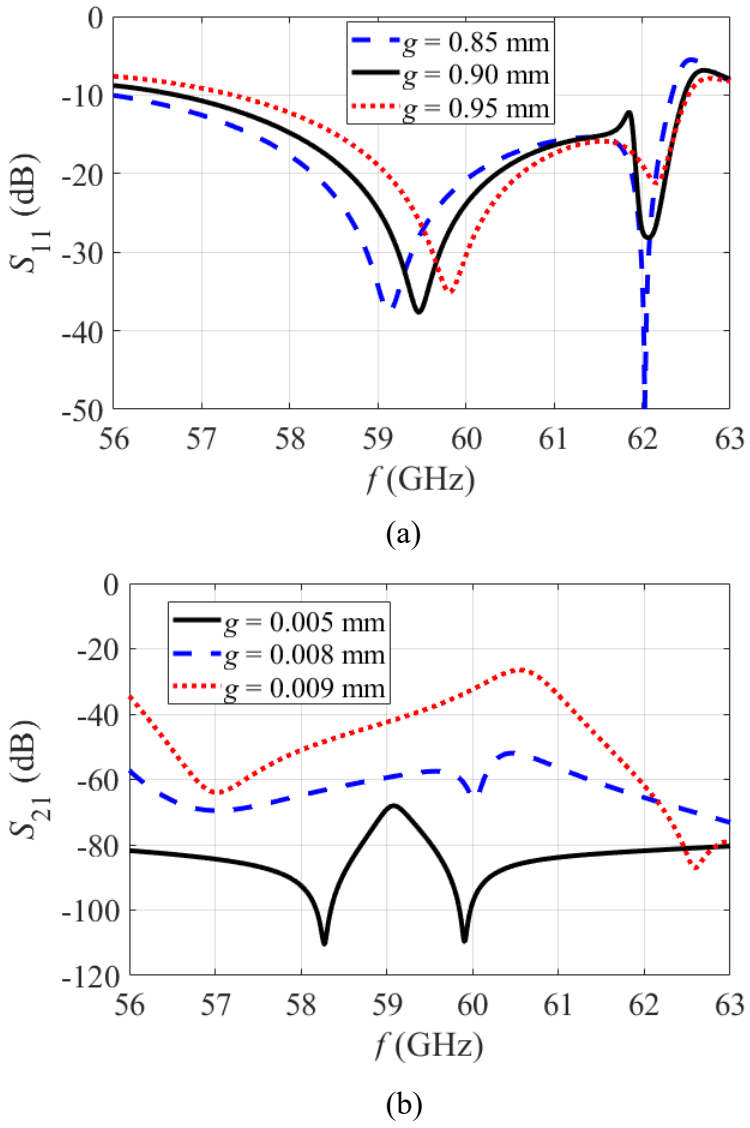

FIGURE 4.25: (a) Scattering parameters of the structure shown in Fig. 4.21 for 3 different values of g in the "on" state. (b) Scattering parameters of the structure shown in Fig. 4.21 for 3 different values of g in the "off" state. Geometrical parameters: $l = 3.4$ mm, $p_{\text{guide}} = 1.5$ mm, $h_{\text{guide}} = 0.2$ mm $d_{\text{guide}} = 0.4$ mm, $p_{\text{EBG}} = 3$ mm, $h_{\text{EBG}} = 1.2$ mm $d_{\text{EBG}} = 0.8$ mm.

Adjacent Waveguides

In this subsection, we study two adjacent waveguides to evaluate the coupling between the two waveguides, both in the "on" and "off" states. This

provides some insights regarding the use of such technology in a switching network. Fig 4.26 (a) displays the top view of the two adjacent waveguides with the top plate removed to better visualize their inner structure. The waveguide ports are numbered in the figure. We excite waveguide port 1 to compute the power flow inside the two waveguides. The waveguides are considered to be made of copper in the simulations. The distance between the two waveguides is 7.5 mm ($1.5\lambda_0$) and the length of the simulated waveguides is 25.5 mm (approximately $5\lambda_0$) where λ_0 is the wavelength of the electromagnetic wave in free space at 60 GHz. Fig 4.26 (b) displays the power flow inside the waveguides at 60 GHz when the structure is in the "on" state. The figure clearly displays that there is a power flow along the longitudinal direction of the excited waveguide from port 1 towards port 2. It also displays that the EBG is completely confining the electromagnetic fields inside the upper waveguide and consequently the good isolation between the two waveguides. In contrast, Fig 4.26 (c) shows the power flow at 60 GHz when the structure is in the "off" state. We observe that there is no power flow along the length of the top excited waveguide. This means that the "off" state is working properly and the waveguide is attenuating the wave in both cross-sectional and longitudinal directions to avoid propagation of the wave in any direction.

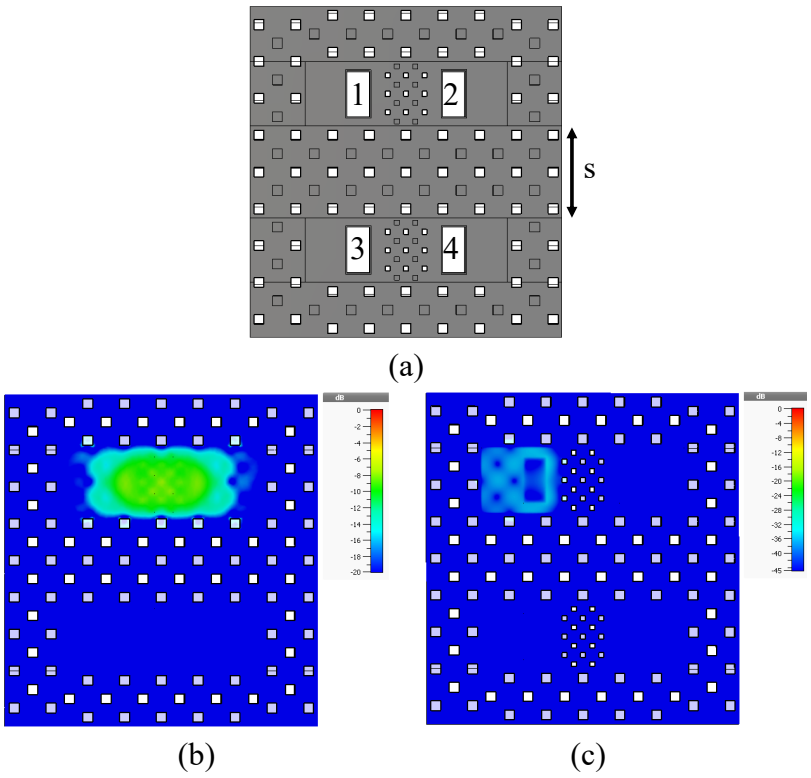

FIGURE 4.26: Two coupled lines: (a) the top view with the top metal plate removed for better visualisation of the inner parts (b) power flow while exciting port 1 at 60 GHz in "on" state (c) power flow while exciting port 1 at 60 GHz in "off" state.

Fig. 4.27 plots the scattering parameters of the structure in Fig. 4.26 (b)

by exciting the upper waveguide through waveguide port 1. S_{11} and S_{21} curves are similar to those shown in Fig. 4.22 with copper as the material. The matched bandwidth is the same and the waveguide is still functioning correctly in it. The -10 dB S_{11} bandwidth is 57.4-62.8 GHz. The insertion loss of less than 0.7 dB is achieved for most of the S_{11} bandwidth (57.4-62.2 GHz). In a small portion of the S_{11} bandwidth (62.2-62.8 GHz) the insertion loss goes beyond 0.7 dB and increases to a maximum of 3.3 dB at the end of the $S_{11} < -10$ dB bandwidth. S_{31} and S_{41} results are plotted in addition to these two curves to demonstrate the coupling between ports of the two waveguides. We observe that there is a good isolation between the waveguides and that the coupling is below -22 dB over the whole operational bandwidth.

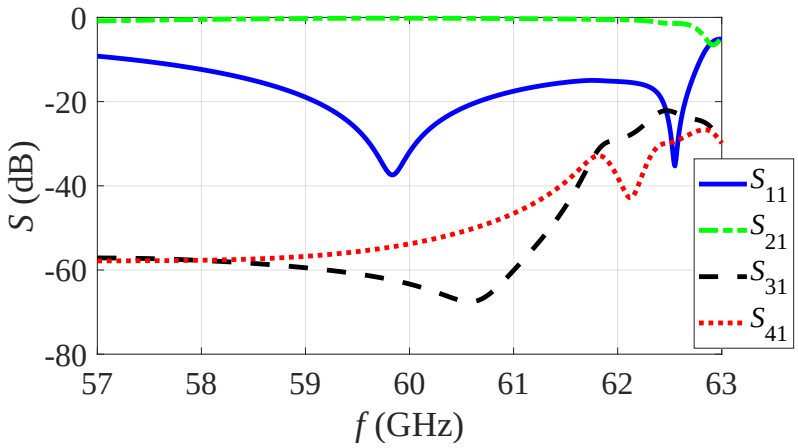

FIGURE 4.27: Scattering parameters of the structure shown in Fig. 4.26 (a).

Fig. 4.28 (a) studies the coupling in more detail. It displays S_{31} for different values of lateral spacing s between the two adjacent waveguides shown in Fig. 4.26 (a). It is observed that the S_{31} decreases as the distance between the two waveguides increases. Due to the increased distance, there is more attenuation of the wave across the EBG region between the two waveguides and lower S_{31} is achieved. An $s = 1.5\, p_{\text{EBG}}$ results in S_{31} of below -40 dB in the first 4 GHz of the $S_{11} < -10$ dB bandwidth. But it increases up to -13.5 dB at one point in the higher frequencies of the bandwidth. Distances of $s = 2.5\, p_{\text{EBG}}$ and $s = 3.5\, p_{\text{EBG}}$ provide better isolation and their S_{31} is below -40 dB for a larger part of the S_{11} bandwidth. S_{31} levels for $s = 2.5\, p_{\text{EBG}}$ and $s = 3.5\, p_{\text{EBG}}$ are respectively below -22 dB and -32 dB over the whole bandwidth. The case $s = 4.5\, p_{\text{EBG}}$ has S_{31} levels below -37 dB in the entire S_{11} bandwidth. It is good to note that since $p_{\text{EBG}} = 3$ mm, tthe spacing $s = 1.5\, p_{\text{EBG}} = 4.5$ mm is ten percent smaller than the free space wavelength $\lambda_0 = 5$ mm at 60 GHz. Fig 4.28 (b) plots S_{41} for the same four values of spacing s to study the effect of s on S_{41}. The observations are similar to those from S_{31}. An increase of s leads to a decrease of S_{41}. Similarly, $s = 4.5\, p_{\text{EBG}}$ achieves the lowest S_{41} levels which is lower than -44 dB in all the -10 dB S_{11} bandwidth.

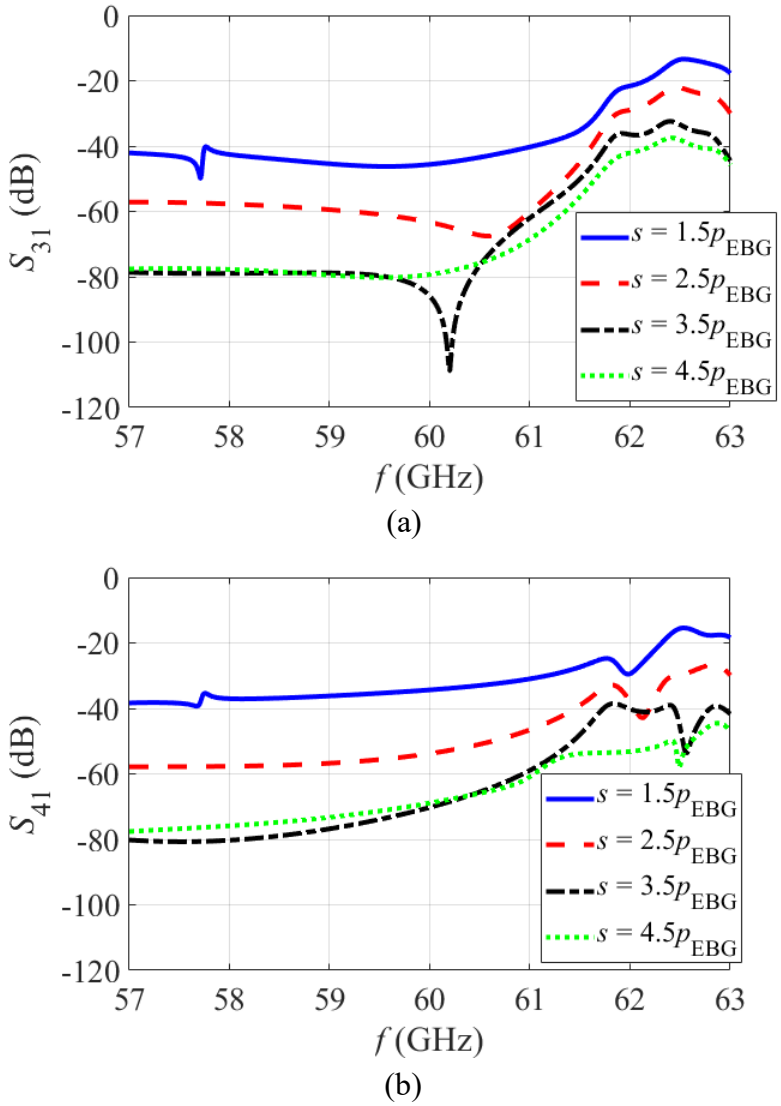

FIGURE 4.28: (a) S_{31} in the structure shown in Fig. 4.26 (a) for different values of s (b) S_{41} in the structure shown in Fig. 4.26 (a) for different values of s.

Comparisons with Non-Glide Waveguides

We investigate the results of the designed coupled waveguides when all the pins on the top plate are removed. The S parameter results of this structure in the "on" state are shown in Fig. 4.29. $S_{11} < -10$ dB occurs around the center frequency of 62 GHz with only 1 GHz width, where S_{21} is below -7.4 dB. Therefore, there is almost no transmission from the first to the second port. Furthermore, S_{31} and S_{41} show considerably higher levels in the same frequency range which signals the inability of the new EBG to remove the coupling between the two lines at these frequencies. To better explain this observation, the full dispersion diagram of the new EBG which is obtained by removing all the top pins from the glide-symmetric EBG is given in Fig. 4.30. Only the first four Bloch modes are shown in this figure. It is easy to notice

that the stopband of this new unit cells falls below the frequency range of our design. This means that these frequencies fall in a passband region and hence this structure does not act as an EBG in these frequencies anymore. This explains why the coupling between the two lines were high for this structure. To achieve a stopband region at the desired frequencies, this unit cell has to be re-designed. Lower periods will be required to push the stopband region to higher frequencies which will in turn lead to higher requirements in terms of the fabrication precision.

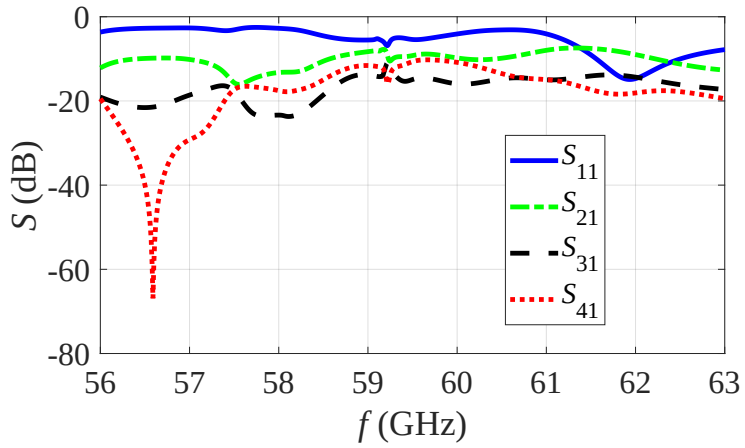

FIGURE 4.29: S parameters of the structure shown in Fig. 4.26 (a) (with glide-symmetric EBG media) in the "on" state with all the top pins removed. Geometrical parameters: $l = 3.4$ mm, $p_{\text{guide}} = 1.5$ mm, $h_{\text{guide}} = 0.2$ mm $d_{\text{guide}} = 0.4$ mm, $p_{\text{EBG}} = 3$ mm, $h_{\text{EBG}} = 1.2$ mm $d_{\text{EBG}} = 0.8$ mm, $g = 0.9$ mm.

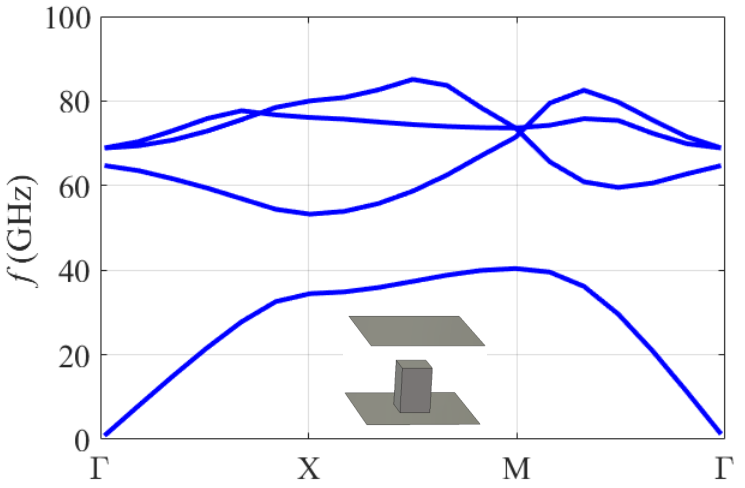

FIGURE 4.30: The full dispersion diagram of the of the EBG media with all the top pins removed. Geometrical parameters: $p_{\text{EBG}} = 3$ mm, $h_{\text{EBG}} = 1.2$ mm $d_{\text{EBG}} = 0.8$ mm, $g = 0.9$ mm.

It should also be noted that the guiding medium used in Fig. 4.26 falls in the reducible glide-symmetry category meaning that it can be replaced by

a non-glide-symmetric medium where all the upper pins are pushed to the lower plate. This is related to the fact that the pins of the guiding medium are not very close in the "on" state, and was of course purposely done to achieve better matching as discussed in Sec. 4.3.1. The glide-symmetric configuration has been preferred to the non-glide-symmetric one since it requires less manufacturing precision.

4.3.5 Measurements

To perform the measurements on the designed reconfigurable waveguide, two coupled lines similar to the one shown in Fig. 4.26(a) were fabricated. The length of the waveguide was increased to allow for coaxial rectangular waveguide adapters to be screwed to the structure. Fig. 4.31 shows a 3D sketch of the final design for fabrication. The structure is designed to be fabricated in three pieces. We chose to fabricate the bottom plate of the structure in one piece while fabricating the top plate in two pieces. This allows the two top plates to move independently of each other and enables us to adjust the gap between the top and bottom plates in each waveguide independently. Therefore, any of the two waveguides can be placed in the "on" or "off" state. To better understand the geometry of the final design shown in Fig. 4.31, separate sketches of the top and bottom plates are helpful.

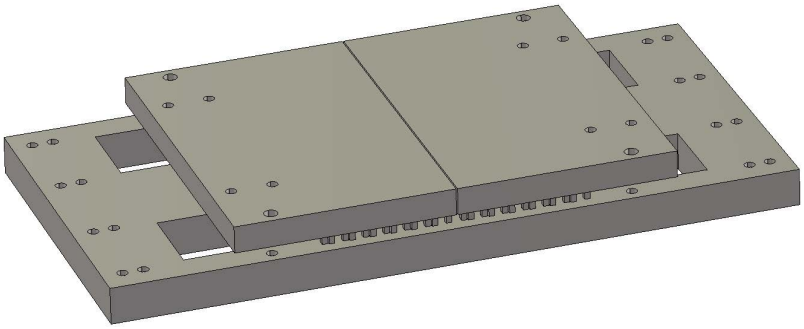

FIGURE 4.31: Perspective view of the final design for fabrication.

Fig. 4.32 (a) depicts the top view of the bottom plate while Fig. 4.32 (b) shows the bottom view of the same plate. The four big rectangular holes in this piece which are labelled "A" in the figures are included to provide the arm of mechanical actuators the free space to move for adjustment of the gap between the top and bottom plates. There are two of these rectangular holes next to each waveguide meaning that each of the top plates can be controlled using two mechanical actuators inserted inside these holes. Four smaller rectangular holes are also visible in the bottom plate which are not labelled. These holes correspond to WR-15 rectangular waveguides dimensions and will be connected to a coaxial to rectangular waveguide adapter for measurements.

In addition to the rectangular holes, the bottom plate possesses many circular holes as shown in Figs. 4.32 (a) and (b). These holes account for the

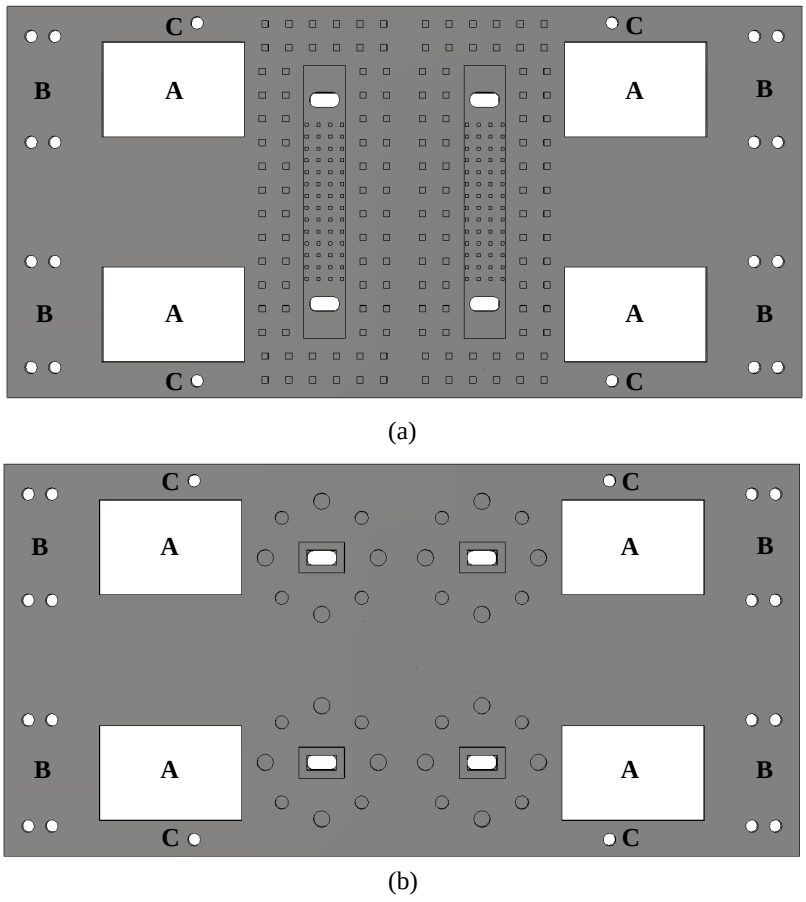

FIGURE 4.32: (a) Top (b) Bottom view of the bottom plate of the final design for fabrication.

required screws. For instance, the actuators will be connected to the bottom plate through metal brackets. For each bracket, four screws are used to connect them to the bottom plate. This corresponds to a total of 16 screws for the four actuators. The sets of four circular holes related to each bracket are labelled "B" in the figure. Furthermore, for each waveguide, two alignment holes have been placed in the bottom plate to make sure that the top and bottom plates are well-aligned and the glide symmetry is not broken. This results in a total of four alignment holes which are labelled "C" in the figure. We will see that similar alignment holes are included in the top plate too. The alignment is done by passing long screws through these alignment holes from the bottom to the top plates. Finally, Fig. 4.32 (b) shows other circular holes which are not labelled. These holes correspond to the screws of the coaxial to rectangular waveguide adapters. In our design, these holes have been chosen according the specifications of the Quinstars QR-15 series rectangular waveguide to coaxial adapters which are used to take the measurements.

Similarly, Fig. 4.33 (a) demonstrates the bottom view of the two top plate pieces while Fig. 4.33 (b) shows their top view. As mentioned earlier the top plates also possess alignment holes. These holes are labelled "E" in the

figure. It should be noted that for the correct alignment of the structure, these holes should be placed at the same horizontal position as those labelled "C" in Figs. 4.32 (a) and (b). We previously discussed that the base of each actuator gets connected to the bottom plate with a bracket. In contrast, the arm of the actuator gets connected to a top plate. Therefore, by placing the bottom plate on a fixed surface, the top plate can be moved higher or lower relative to the bottom plate through mechanical actuation. Again a bracket is used for each connection between a top plate and an actuator arm. The holes corresponding to screwing these brackets are labelled "F" in the figure.

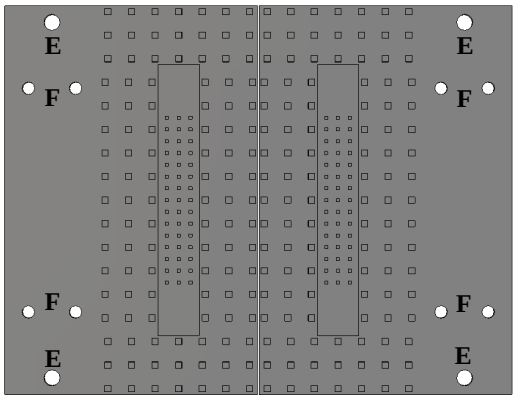

(a)

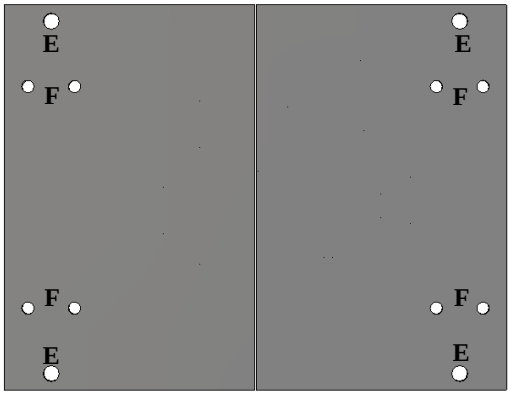

(b)

FIGURE 4.33: a) Bottom (b) Top view of the bottom plate of the final design for fabrication.

Fig. 4.34 shows the photo of the fabricated bottom plate next to the top plate piece. As the photo shows, a one euro coin is placed next to the pieces to provide a visual comparison between the physical dimensions of the pieces. The plates are fabricated in aluminum and coated with silver. The thickness of the top plates is 7 mm while the thickness of the bottom plate is 5.5 mm.

As it was mentioned earlier, the actuators we use for mechanically switching the waveguides between the "on" and "off" states are from the SLC series of SmarAct's linear piezoelectric stages. Fig. 4.35 shows a photo of the piezoelectric actuator model that we use in our prototype. This model provides a high precision positioning with a linear travel range of 21 mm.

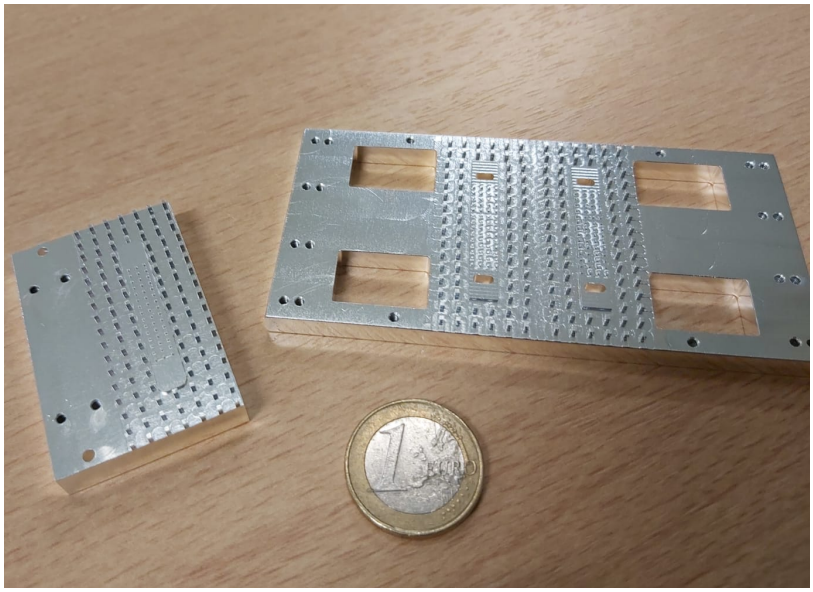

FIGURE 4.34: The fabricated top and bottom pieces of the final design.

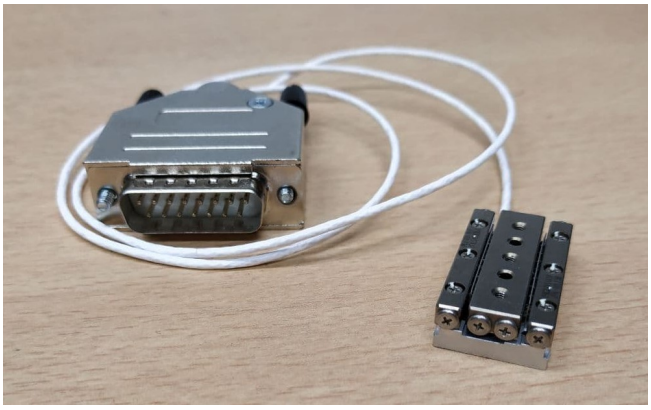

FIGURE 4.35: The piezoelectric actuator used in our prototypes for mechanically switching the waveguides between "on" and "off" states.

To drive the actuators to the "on" and "off" required positions, a compatible controller from SmarAct's CU series of controllers is used. These controllers consist of two units each. The first one is the main control unit and the second one is the driver. Fig. 4.36 (a) shows the main control unit of our controller. This unit has a USB port for a connection with a personal computer or a workstation for programming the actuation. Furthermore, it connects to a power supply as well as the driver unit. The driver unit is shown in Fig. 4.36 (b). It is a three channel driver which can drive up to 3 actuators with the same control unit. Therefore, for driving 4 actuators two controllers are required. Fig. 4.37 displays a photo of the controller units and an actuator connected together.

(a) (b)

FIGURE 4.36: The two units of the controller used to drive the actuator: (a) the main control unit (b) the three channel driver.

FIGURE 4.37: Connection of the controller unit and the actuator.

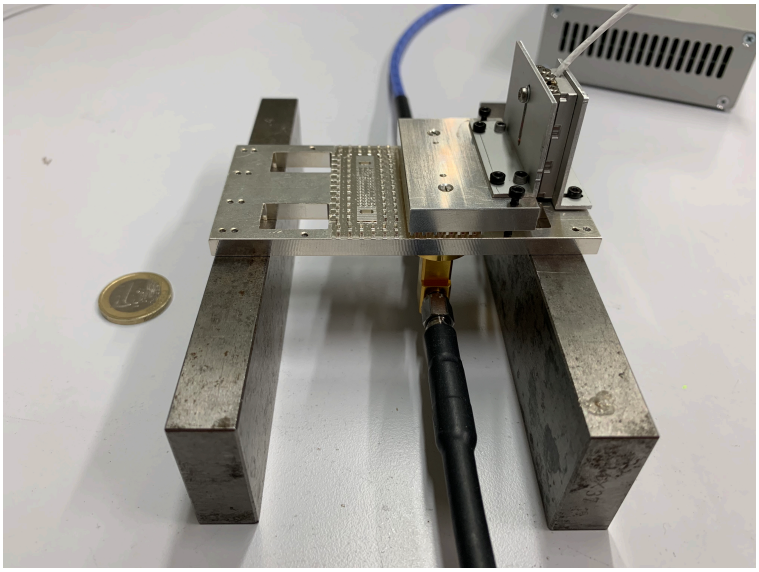

FIGURE 4.38: Photo of the assembled prototype.

Fig. 4.38 shows a photo of the assembled prototype for which the measurements are taken. Firstly, we note that the measurements are taken with only one of the two adjacent waveguides assembled. This can be recognized by observing only one top plate instead of two. Furthermore, it can be observed that only one actuator is used instead of two. This is due to our observation that a single actuator could carry the weight of the top plate without any problem in the actuation process. Therefore, there was no need to utilize two actuators for each waveguide. This also allows us to use only one controller instead of two for future measurements with the two waveguides since there would be two actuators instead of four.

Fig. 4.39 displays a photo of the setup used to make measurements on the prototype. In this setup, the controller is connected to a personal computer for receiving commands. To send these commands, we have developed a MATLAB code that moves the actuator to switch the waveguide between the "on" and "off"states. The S parameter measurements are carried out using a vector network analyzer which is also shown in the figure. Fig. 4.40 displays the vector network analyzer used for our measurements. It is the Rhode and Schawrz ZVA 67 model which covers the 10 MHz to 67 GHz frequency range.

Fig. 4.41 plots the measured S_{11} and S_{21} versus frequency for the "on" state. In the "on" state, the waveguide is letting the wave propagate from one port to the other. In fact, S_{21} has values higher than -0.9 dB from 56.2 GHz to 62.8 GHz. This corresponds to an insertion loss of 0.09 dB/wavelength of the structure, comparable with the insertion loss of 0.14 dB/wavelength of the structure in previous simulations from 57.4 GHz to 62.2 GHz. We remind the reader that the simulations and the prototype differ in the length of the guiding medium and the S parameters cannot be directly compared. Also, S_{11} shows a good matching at the input port of the waveguide. Notice that S_{21} has been correctly measured by calibrating the connections between the ports with the adapters used here so it is referred to the transmission inside the waveguide as expected. Instead S_{11} is calculated right before the coaxial

to rectangular waveguide adapter and therefore does not bypass the effect of these connectors.

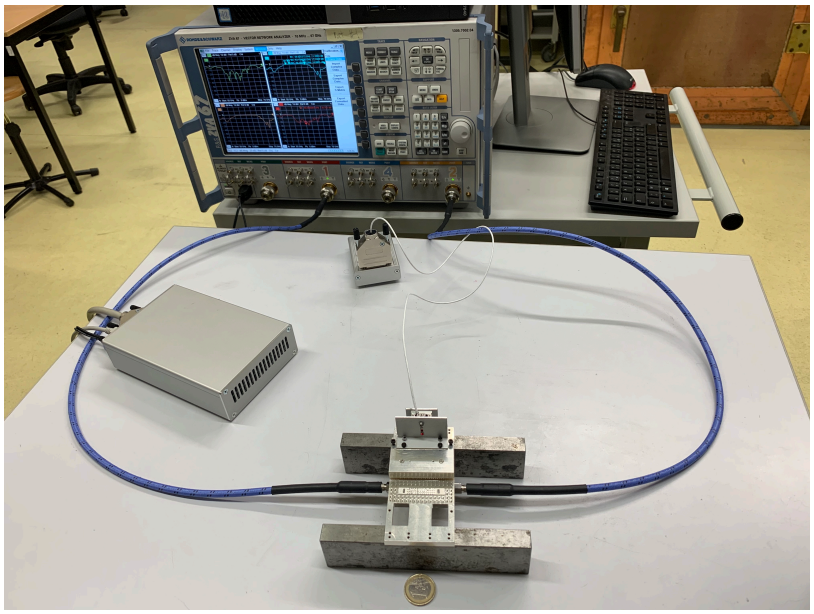

FIGURE 4.39: Photo of the measurement setup for the prototype.

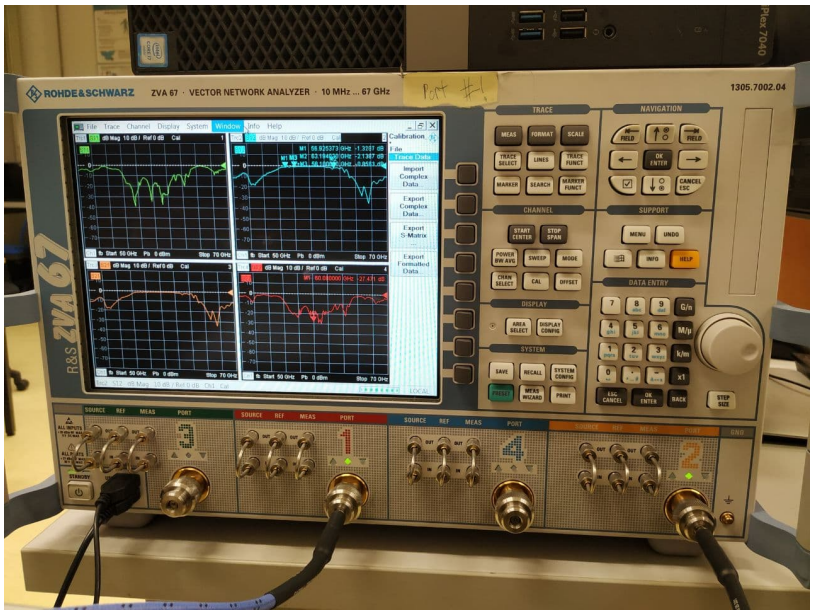

FIGURE 4.40: Photo of the vector network analyzer used for measurements.

Similarly, Fig. 4.42 plots the measured S_{11} and S_{21} versus frequency for the "off" state. Again in calculation of the S_{11} the effect of the adapters are not de-embedded. The figure clearly demonstrates the lack of wave propagation along the waveguide as the measured S_{21} is below -20 dB at all the frequencies. This result is higher than the simulated one (lower than -50 dB)

and depends on the difficulty to achieve a uniform gap of 0.005 mm between the surfaces avoiding any inclination between them.

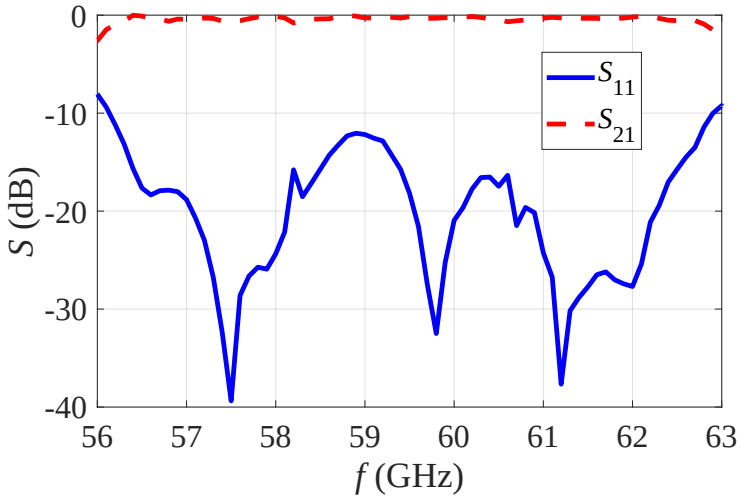

FIGURE 4.41: Plot of the measured S_{11} and S_{21} of the prototype versus frequency in the "on" state.

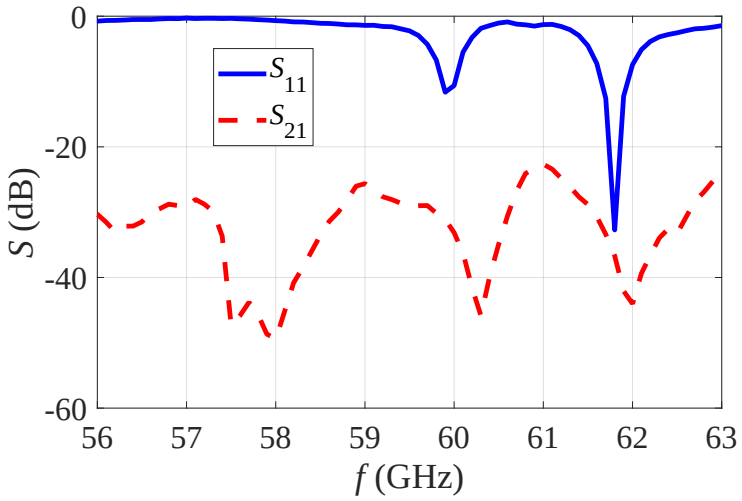

FIGURE 4.42: Plot of the measured S_{11} and S_{21} of the prototype versus frequency in the "off" state.

4.4 Conclusions

In summary, in this chapter we investigated the possibility of achieving reconfigurability in glide-symmetric structures. In fulfillment of this investigation, we introduced a reconfigurable artificial waveguide based on a parallel-plate waveguide technology where the propagation inside the waveguide is enabled or disabled in a two-state reconfiguration mechanism. We accomplished this goal by using a mechanical reconfiguration of the structure to

allow the guiding media to alternate between a passband and a stopband. Piezoelectric mechanical switches can reconfigure the displacement between the two metallic plates of the design. We designed our reconfigurable waveguide to operate in 57.4-62.2 GHz frequency range. We achieved a measured isolation higher than 20 dB in the off-state and a measured insertion loss of less than 0.9 dB corresponding to 0.09 dB/wavelength of the structure. We showed the low loss nature of the design due to the absence of dielectric material. We furthermore pointed out the possibility of this device to find application in design of low-loss RF switches that can be used in MMW multibeam antennas.

Chapter 5

Conclusion

Higher symmetric periodic structures have emerged as interesting topologies for different electromagnetic applications. Their different dispersive behavior compared to their non-symmetric counterparts has given them the edge in applications such as low dispersive propagation, filtering and electromagnetic bandgap material. Due to these special characteristics and applications, it is important to have accurate analysis tools to extract their exact behavior and to understand the physical phenomenon that leads to their unique characteristics. This understanding can result in a more efficient use of these structures in novel applications. To this aim, we introduced a multimodal approach based on the generalization of a single-mode Bloch analysis and used this method to study the difference between the higher symmetric and non-higher symmetric periodic unit cells. We then used this method in analysis and design of a mm-wave reconfigurable waveguide with the capability to enable or prevent the propagation of the wave. We achieved the reconfigurability through controlling a geometrical parameter of the structure using a piezoelectric actuator. This technology has potential applications for mm-wave switches feeding multibeam antennas for 5G communications.

5.1 Contributions

This body of research has made several contributions to the field of electromagnetics theory and design.

- Presented a specific formulation of the novel analysis method for higher-symmetric structures to analyze these structures more rapidly.

We reformulated the multimodal Bloch analysis method for glide-symmetric and twist-symmetric periodic structures by taking into account the higher symmetry of these structures. As a result, the novel formulation applies to a sub-region of the unit cell and therefore less resources are needed to calculate the transmission matrix of this smaller cell compared to the unit cell itself. This has improved the calculation time of the dispersion diagrams for these structures.

- Defined irreducible and reducible higher symmetry to describe the two different behavior of higher symmetric unit cells.

We observed that in some examples of higher symmetry, the dispersive results are the same as those with the same geometrical parameters but with no higher symmetry. We acknowledged the difference between these structures and those that demonstrate different dispersive behavior compared to their counterparts with no higher symmetry. We called the first group of higher symmetries reducible while we called the other group irreducible. This labeling may infer whether a higher symmetric structure may or may not be preferred to a periodic structure with no higher symmetry in a certain application.

- Explained the different behavior of irreducible higher symmetric unit cells with respect to their non-higher symmetric counterparts in terms of inter-cell interactions of higher order modes

We were able to utilize the multimodal Bloch analysis method that we developed to demonstrate how the higher order modes interact with each other differently in a periodic structure with and without higher symmetry in irreducible structures while the same modes become non-important in reducible structures which causes the higher symmetric structure to act similarly to its non-higher symmetric counterpart.

- Studied the feasibility of reconfigurable on/off waveguide structure with glide symmetric structures through reconfiguration of one geometric parameter.

We designed glide-symmetric unit cells for EBG and guiding media and showed that reconfiguration of the waveguide can be achieved by merely adjusting the distance between the two contact-less parts of the structure. We showed how by alternating between two different values of this distance, propagation of the wave could be enabled or prevented. This reconfiguration scheme may possibly be used for the design of different reconfigurable components.

- Designed two reconfigurable on/off waveguide using the aforementioned technology.

We completed the design by introducing a matching mechanism and a feeding section to realize two configurations of reconfigurable waveguides. We then explained why one of the two designs outperforms the other design in terms of its loss, matching bandwidth and size. We achieved a 57.4-62.2 GHz working frequency range for our design with isolation levels better than 65 dB and insertion loss lower than -0.7 dB. We finally investigated the feasibility of the same design with non-glide-symmetric unit cells instead of glide-symmetric ones.

5.2 Future Work

There are a variety of future research avenues stemming from this work. In particular, we see a few main areas of further research.

- Application of the developed analysis method to open structures for design and analysis of leaky waveguides.

As, we have already said multiple times, an advantage of the developed Bloch analysis method is its capability to solve for complex wave vectors. As a result, it provides the attenuation constant in addition to the phase constant. This means that this method can also be applied to open structures such as leaky-wave antennas to compute radiation losses. Thus, as a future work, this analysis method can be used to design and develop leaky wave antennas.

- Application of the developed analysis method to design EBG structure with strong attenuation.

We have shown that the strength of the attenuation in EBG materials would be different for different EBG unit cells regardless of their stopband frequency ranges. To find the exact value of the attenuation, a Bloch analysis like that developed in this work are required to accurately compute the values of the attenuation constant. This method can be used to compare different EBG unit cells and choose the best EBG material according to its application.

- Design of other reconfigurable microwave components based on the reconfigurable waveguide technology developed in this work.

We have developed a basic reconfigurable on/off waveguide that could possibly find its way in design of waveguide switches in higher frequencies. However, based on this reconfigurable waveguide technology, other reconfigurable components could be designed and developed. For instance, as a future work, it would be interesting to utilize this technology to design a reconfigurable phase shifter in which the adjustment of the geometrical distance between its two sections will reconfigure the phase shift provided by the component. Other reconfiguration strategies will aim at the design of beam scanning planar antennas, where the direction of the radiated beam is dependent on a geometrical parameter of the metasurfaces, which can be modified with the considered actuators. Finally, surfaces based on holes rather than on pins should also be explored in order to simplify the practical realization.

Bibliography

[1] J. D. Joannopoulos and S. G. Johnson, *Photonic Crystals: Molding the Flow of Light*. Princeton University Press, 2008.

[2] A. Hessel, M. H. Chen, R. C. M. Li, and A. A. Oliner, "Propagation in periodically loaded waveguides with higher symmetries," *Proceedings of the IEEE*, vol. 61, no. 2, pp. 183–195, Feb. 1973.

[3] P. J. Crepeau and P. R. McIsaac, "Consequences of symmetry in periodic structures," *Proceedings of the IEEE*, vol. 52, no. 1, pp. 33–43, Jan 1964.

[4] R. Mittra and S. Laxpati, "Propagation in a wave guide with glide reflection symmetry," *Canadian Journal of Physics*, vol. 43, no. 2, pp. 353–372, 1965. [Online]. Available: https://doi.org/10.1139/p65-032

[5] R. Kieburtz and J. Impagliazzo, "Multimode propagation on radiating traveling-wave structures with glide-symmetric excitation," *IEEE Transactions on Antennas and Propagation*, vol. 18, no. 1, pp. 3–7, Jan 1970.

[6] R. Quesada, D. Martín-Cano, F. J. García-Vidal, and J. Bravo-Abad, "Deep-subwavelength negative-index waveguiding enabled by coupled conformal surface plasmons," *Opt. Lett.*, vol. 39, no. 10, pp. 2990–2993, May 2014.

[7] J. J. Wu, C.-J. Wu, D. J. Hou, K. Liu, and T.-J. Yang, "Propagation of low-frequency spoof surface plasmon polaritons in a bilateral cross-metal diaphragm channel waveguide in the absence of bandgap," *IEEE Photonics Journal*, vol. 7, no. 1, pp. 1–8, 2015.

[8] D. Cavallo and C. Felita, "Analytical formulas for artificial dielectrics with non-aligned layers," *IEEE Transactions on Antennas and Propagation*, vol. PP, no. 99, pp. 1–1, 2017.

[9] T. Chang, J. U. Kim, S. K. Kang, H. Kim, D. K. Kim, Y.-H. Lee, and J. Shin, "Broadband giant-refractive-index material based on mesoscopic space-filling curves," *Nature Materials*, vol. 7, pp. 772–775, Aug 2016. [Online]. Available: https://www.nature.com/articles/ncomms12661

[10] D. Jia, Y. He, N. Ding, J. Zhou, B. Du, and W. Zhang, "Beam-steering flat lens antenna based on multilayer gradient index metamaterials," *IEEE Antennas and Wireless Propagation Letters*, vol. 17, no. 8, pp. 1510–1514, Aug 2018.

[11] O. Quevedo-Teruel, M. Ebrahimpouri, and M. N. M. Kehn, "Ultrawideband metasurface lenses based on off-shifted opposite layers," *IEEE Antennas and Wireless Propagation Letters*, vol. 15, pp. 484–487, Dec. 2016.

[12] A. A. Brazález, L. Manholm, M. Johansson, O. Quevedo-Teruel, and J. Miao, "Investigation of a ka-band luneburg lens made of a glide-symmetric holey structure," in *Antennas and Propagation (ISAP), 2017 International Symposium on*. IEEE, 2017, pp. 1–2.

[13] O. Quevedo-Teruel, J. Miao, M. Mattsson, A. Algaba-Brazalez, M. Johansson, and L. Manholm, "Glide-symmetric fully metallic Luneburg lens for 5G communications at Ka-band," *IEEE Antennas and Wireless Propagation Letters*, vol. 17, no. 9, pp. 1588–1592, Sept 2018.

[14] O. Quevedo-Teruel, M. Ebrahimpouri, and F. Ghasemifard, "Lens antennas for 5G communications systems," *IEEE Communications Magazine*, vol. 56, no. 7, pp. 36–41, JULY 2018.

[15] K. Liu, F. Ghasemifard, and O. Quevedo-Teruel, "Broadband metasurface luneburg lens antenna based on glide-symmetric bed of nails," in *2017 11th European Conference on Antennas and Propagation (EUCAP)*. IEEE, 2017, pp. 358–360.

[16] Q. Chen, O. Zetterstrom, F. Mesa, P. Padilla, A. Palomares-Caballero, E. Pucci, X. Yin, and O. Quevedo-Teruel, "Prism-based leaky-lens antennas at 60 ghz for 5g point-to-point communication links," in *2020 14th European Conference on Antennas and Propagation (EuCAP)*. IEEE, 2020, pp. 1–4.

[17] M. Ebrahimpouri, O. Quevedo-Teruel, and E. Rajo-Iglesias, "Design guidelines for gap waveguide technology based on glide-symmetric holey structures," *IEEE Microwave and Wireless Components Letters*, vol. 27, no. 6, pp. 542–544, 2017.

[18] M. Ebrahimpouri, E. Rajo-Iglesias, Z. Sipus, and O. Quevedo-Teruel, "Cost-effective gap waveguide technology based on glide-symmetric holey EBG structures," *IEEE Transactions on Microwave Theory and Techniques*, vol. 66, no. 2, pp. 927–934, Feb 2018.

[19] E. Rajo-Iglesias, M. Ebrahimpouri, and O. Quevedo-Teruel, "Wideband phase shifter in groove gap waveguide technology implemented with glide-symmetric holey EBG," *IEEE Microwave and Wireless Components Letters*, vol. 28, no. 6, pp. 476–478, June 2018.

[20] Q. Liao, E. Rajo-Iglesias, and O. Quevedo-Teruel, "*ka*-band fully metallic te 40 slot array antenna with glide-symmetric gap waveguide technology," *IEEE Transactions on Antennas and Propagation*, vol. 67, no. 10, pp. 6410–6418, 2019.

[21] P. Padilla, Á. Palomares-Caballero, A. Alex-Amor, J. Valenzuela-Valdés, J. M. Fernández-González, and O. Quevedo-Teruel, "Broken glide-symmetric holey structures for bandgap selection in gap-waveguide technology," *IEEE Microwave and Wireless Components Letters*, vol. 29, no. 5, pp. 327–329, 2019.

[22] A. Monje-Real, N. Fonseca, O. Zetterstrom, E. Pucci, and O. Quevedo-Teruel, "Holey glide-symmetric filters for 5g at millimeter-wave frequencies," *IEEE Microwave and Wireless Components Letters*, vol. 30, no. 1, pp. 31–34, 2019.

[23] E. D. Sharp, "A high-power wide-band waffle-iron filter," *IEEE Transactions on Microwave Theory and Techniques*, vol. 11, no. 2, pp. 111–116, 1963.

[24] M. Ebrahimpouri, A. A. Brazalez, L. Manholm, and O. Quevedo-Teruel, "Using glide-symmetric holes to reduce leakage between waveguide flanges," *IEEE Microwave and Wireless Components Letters*, vol. 28, no. 6, pp. 473–475, June 2018.

[25] S. Rahiminejad, E. Pucci, V. Vassilev, P.-S. Kildal, S. Haasl, and P. Enoksson, "Polymer gap adapter for contactless, robust, and fast measurements at 220–325 ghz," *Journal of Microelectromechanical Systems*, vol. 25, no. 1, pp. 160–169, 2015.

[26] M. Ebrahimpouri, L. Herran, and O. Quevedo-Teruel, "Wide-angle impedance matching using glide-symmetric metasurfaces," *IEEE Microwave and Wireless Components Letters*, vol. 30, no. 1, pp. 8–11, 2019.

[27] P. Padilla, L. F. Herrán, A. Tamayo-Domínguez, J. F. Valenzuela-Valdés, and O. Quevedo-Teruel, "Glide symmetry to prevent the lowest stopband of printed corrugated transmission lines," *IEEE Microwave and Wireless Components Letters*, vol. 28, no. 9, pp. 750–752, Sept 2018.

[28] B. A. Mouris, A. Fernández-Prieto, R. Thobaben, J. Martel, F. Mesa, and O. Quevedo-Teruel, "On the increment of the bandwidth of mushroom-type ebg structures with glide symmetry," *IEEE Transactions on Microwave Theory and Techniques*, vol. 68, no. 4, pp. 1365–1375, 2020.

[29] F. Ghasemifard, M. Norgren, and O. Quevedo-Teruel, "Twist and polar glide symmetries: an additional degree of freedom to control the propagation characteristics of periodic structures," *Scientific Reports*, vol. 8, no. 1, p. 11266, 2018. [Online]. Available: https://doi.org/10.1038/s41598-018-29565-6

[30] Q. Chen, F. Ghasemifard, G. Valerio, and O. Quevedo-Teruel, "Modeling and dispersion analysis of coaxial lines with higher symmetries," *IEEE Transactions on Microwave Theory and Techniques*, no. 99, pp. 1–8, 2018.

[31] O. Quevedo-Teruel, O. Dahlberg, and G. Valerio, "Propagation in waveguides with transversal twist-symmetric holey metallic plates," *IEEE Microwave and Wireless Components Letters*, 2018.

[32] O. Dahlberg, R. C. Mitchell-Thomas, and O. Quevedo-Teruel, "Reducing the dispersion of periodic structures with twist and polar glide symmetries," *Scientific Reports*, vol. 7, Art. no. 10136, 2017.

[33] G. Valerio, F. Ghasemifard, Z. Sipus, and O. Quevedo-Teruel, "Glide-symmetric all-metal holey metasurfaces for low-dispersive artificial materials: Modeling and properties," *IEEE Transactions on Microwave Theory and Techniques*, vol. 66, no. 7, pp. 3210–3223, July 2018.

[34] F. Ghasemifard, M. Norgren, and O. Quevedo-Teruel, "Dispersion analysis of 2-d glide-symmetric corrugated metasurfaces using mode-matching technique," *IEEE Microwave and Wireless Components Letters*, vol. 28, no. 1, pp. 1–3, Jan 2018.

[35] G. Valerio, Z. Sipus, A. Grbic, and O. Quevedo-Teruel, "Accurate equivalent-circuit descriptions of thin glide-symmetric corrugated metasurfaces," *IEEE Transactions on Antennas and Propagation*, vol. 65, no. 5, pp. 2695–2700, May 2017.

[36] N. Marcuvitz, *Waveguide Handbook*. Isha Books, 2013.

[37] F. Mesa, R. Rodríguez-Berral, and F. Medina, "On the computation of the dispersion diagram of symmetric one-dimensionally periodic structures," *Symmetry*, vol. 10, no. 8, 2018. [Online]. Available: http://www.mdpi.com/2073-8994/10/8/307

[38] M. A. Eberspächer and T. F. Eibert, "Dispersion analysis of complex periodic structures by full-wave solution of even-odd-mode excitation problems for single unit cells," *IEEE Transactions on Antennas and Propagation*, vol. 61, no. 12, pp. 6075–6083, Dec 2013.

[39] C. Chan, Q. Yu, and K. Ho, "Order-n spectral method for electromagnetic waves," *Physical Review B*, vol. 51, no. 23, p. 16635, 1995.

[40] C.-C. Chen, "Scattering by a two-dimensional periodic array of conducting plates," *IEEE Transactions on Antennas and Propagation*, vol. 18, no. 5, pp. 660–665, 1970.

[41] R. Florencio, R. R. Boix, and J. A. Encinar, "Enhanced mom analysis of the scattering by periodic strip gratings in multilayered substrates," *IEEE transactions on antennas and propagation*, vol. 61, no. 10, pp. 5088–5099, 2013.

[42] ——, "Fast and accurate mom analysis of periodic arrays of multilayered stacked rectangular patches with application to the design of reflectarray antennas," *IEEE Transactions on Antennas and Propagation*, vol. 63, no. 6, pp. 2558–2571, 2015.

[43] G. Pelosi, A. Freni, and R. Coccioli, "Hybrid technique for analysing scattering from periodic structures," in *IEE Proceedings H (Microwaves, Antennas and Propagation)*, vol. 140, no. 2. IET, 1993, pp. 65–70.

[44] R.-B. Hwang, *Periodic structures: mode-matching approach and applications in electromagnetic engineering*. John Wiley & Sons, 2012.

[45] D. M. Pozar, "Microwave engineering," *Fourth Editions, University of Massachusetts at Amherst, John Wiley & Sons, Inc*.

[46] M. Tsuji, S. Matsumoto, H. Shigesawa, and K. Takiyama, "Guided-wave experiments with dielectric waveguides having finite periodic corrugation," *IEEE Transactions on Microwave Theory and Techniques*, vol. 31, no. 4, pp. 337–344, 1983.

[47] H. K. Liu and T. L. Dong, "Propagation characteristics for periodic waveguide based on generalized conservation of complex power technique," *IEEE transactions on microwave theory and techniques*, vol. 54, no. 9, pp. 3479–3485, 2006.

[48] F. Bongard, J. Perruisseau-Carrier, and J. R. Mosig, "Enhanced periodic structure analysis based on a multiconductor transmission line model and application to metamaterials," *IEEE Transactions on Microwave Theory and Techniques*, vol. 57, no. 11, pp. 2715–2726, 2009.

[49] R. Islam, M. Zedler, and G. V. Eleftheriades, "Modal analysis and wave propagation in finite 2d transmission-line metamaterials," *IEEE transactions on antennas and propagation*, vol. 59, no. 5, pp. 1562–1570, 2011.

[50] P. Russer, 03 2006.

[51] MATLAB, *version 9.3.0 (R2017b)*. Natick, Massachusetts: The MathWorks Inc., 2017.

[52] V. Galdi and I. M. Pinto, "A simple algorithm for accurate location of leaky-wave poles for grounded inhomogeneous dielectric slabs," *Microwave and optical technology letters*, vol. 24, no. 2, pp. 135–140, 2000.

[53] "CST Microwave Studio," http://www.cst.com/, version: 2016.

[54] G. Valerio, S. Paulotto, P. Baccarelli, P. Burghignoli, and A. Galli, "Accurate Bloch analysis of 1-D periodic lines through the simulation of truncated structures," *IEEE Transactions on Antennas and Propagation*, vol. 59, no. 6, pp. 2188–2195, Jun. 2011.

[55] J. G. Andrews, S. Buzzi, W. Choi, S. V. Hanly, A. Lozano, A. C. Soong, and J. C. Zhang, "What will 5g be?" *IEEE Journal on selected areas in communications*, vol. 32, no. 6, pp. 1065–1082, 2014.

[56] F. Boccardi, R. W. Heath, A. Lozano, T. L. Marzetta, and P. Popovski, "Five disruptive technology directions for 5g," *IEEE Communications Magazine*, vol. 52, no. 2, pp. 74–80, 2014.

[57] W. Hong, Z. H. Jiang, C. Yu, J. Zhou, P. Chen, Z. Yu, H. Zhang, B. Yang, X. Pang, M. Jiang *et al.*, "Multibeam antenna technologies for 5g wireless communications," *IEEE Transactions on Antennas and Propagation*, vol. 65, no. 12, pp. 6231–6249, 2017.

[58] Z. Pi and F. Khan, "An introduction to millimeter-wave mobile broadband systems," *IEEE communications magazine*, vol. 49, no. 6, pp. 101–107, 2011.

[59] J. Qiao, X. S. Shen, J. W. Mark, Q. Shen, Y. He, and L. Lei, "Enabling device-to-device communications in millimeter-wave 5g cellular networks," *IEEE Communications Magazine*, vol. 53, no. 1, pp. 209–215, 2015.

[60] W. Roh, J.-Y. Seol, J. Park, B. Lee, J. Lee, Y. Kim, J. Cho, K. Cheun, and F. Aryanfar, "Millimeter-wave beamforming as an enabling technology for 5g cellular communications: Theoretical feasibility and prototype results," *IEEE communications magazine*, vol. 52, no. 2, pp. 106–113, 2014.

[61] T. S. Rappaport, S. Sun, R. Mayzus, H. Zhao, Y. Azar, K. Wang, G. N. Wong, J. K. Schulz, M. Samimi, and F. Gutierrez, "Millimeter wave mobile communications for 5g cellular: It will work!" *IEEE access*, vol. 1, pp. 335–349, 2013.

[62] B. Razavi, "Design of millimeter-wave cmos radios: A tutorial," *IEEE Transactions on Circuits and Systems I: Regular Papers*, vol. 56, no. 1, pp. 4–16, 2009.

[63] C. H. Doan, S. Emami, A. M. Niknejad, and R. W. Brodersen, "Millimeter-wave cmos design," *IEEE Journal of solid-state circuits*, vol. 40, no. 1, pp. 144–155, 2005.

[64] J. Chen, W. Hong, H. Tang, P. Yan, L. Zhang, G. Yang, D. Hou, and K. Wu, "Silicon based millimeter wave and thz ics," *IEICE transactions on electronics*, vol. 95, no. 7, pp. 1134–1140, 2012.

[65] 3GPP. (1999) Release 17. [Online]. Available: https://www.3gpp.org/release-17

[66] A. L. Swindlehurst, E. Ayanoglu, P. Heydari, and F. Capolino, "Millimeter-wave massive mimo: The next wireless revolution?" *IEEE Communications Magazine*, vol. 52, no. 9, pp. 56–62, 2014.

[67] E. G. Larsson, O. Edfors, F. Tufvesson, and T. L. Marzetta, "Massive mimo for next generation wireless systems," *IEEE communications magazine*, vol. 52, no. 2, pp. 186–195, 2014.

[68] T. E. Bogale and L. B. Le, "Massive mimo and mmwave for 5g wireless hetnet: Potential benefits and challenges," *IEEE Vehicular Technology Magazine*, vol. 11, no. 1, pp. 64–75, 2016.

[69] A. Alkhateeb, O. El Ayach, G. Leus, and R. W. Heath, "Hybrid precoding for millimeter wave cellular systems with partial channel knowledge," in *2013 Information Theory and Applications Workshop (ITA)*. IEEE, 2013, pp. 1–5.

[70] ——, "Channel estimation and hybrid precoding for millimeter wave cellular systems," *IEEE Journal of Selected Topics in Signal Processing*, vol. 8, no. 5, pp. 831–846, 2014.

[71] T. E. Bogale and L. B. Le, "Beamforming for multiuser massive mimo systems: Digital versus hybrid analog-digital," in *2014 IEEE Global Communications Conference*. IEEE, 2014, pp. 4066–4071.

[72] S. Han, I. Chih-Lin, Z. Xu, and C. Rowell, "Large-scale antenna systems with hybrid analog and digital beamforming for millimeter wave 5g," *IEEE Communications Magazine*, vol. 53, no. 1, pp. 186–194, 2015.

[73] M. Stanley, Y. Huang, T. Loh, Q. Xu, H. Wang, and H. Zhou, "A high gain steerable millimeter-wave antenna array for 5g smartphone applications," in *2017 11th European Conference on Antennas and Propagation (EUCAP)*. IEEE, 2017, pp. 1311–1314.

[74] X. Wang, X. Fang, M. Laabs, and D. Plettemeier, "Compact 2-d multibeam array antenna fed by planar cascaded butler matrix for millimeter-wave communication," *IEEE Antennas and Wireless Propagation Letters*, vol. 18, no. 10, pp. 2056–2060, 2019.

[75] J. Brady, N. Behdad, and A. M. Sayeed, "Beamspace mimo for millimeter-wave communications: System architecture, modeling, analysis, and measurements," *IEEE Transactions on Antennas and Propagation*, vol. 61, no. 7, pp. 3814–3827, 2013.

[76] R. Méndez-Rial, C. Rusu, N. González-Prelcic, A. Alkhateeb, and R. W. Heath, "Hybrid mimo architectures for millimeter wave communications: Phase shifters or switches?" *Ieee Access*, vol. 4, pp. 247–267, 2016.

[77] V. Varadan, K. Vinoy, and K. Jose, "Switches for rf and microwave applications," in *RF MEMS and Their Applications*. Wiley, 2003.

[78] B. Adelseck, H. Callsen, H. Meinel, W. Menzel, and K. Solbach, "A survey of planar integrated mm-wave components," *Radio and Electronic Engineer*, vol. 52, no. 1, pp. 46–50, 1982.

[79] Z. Baghchehsaraei and J. Oberhammer, "Parameter analysis of millimeter-wave waveguide switch based on a mems-reconfigurable surface," *IEEE transactions on microwave theory and techniques*, vol. 61, no. 12, pp. 4396–4406, 2013.

[80] N. Vahabisani and M. Daneshmand, "Monolithic millimeter-wave mems waveguide switch," *IEEE Transactions on Microwave Theory and Techniques*, vol. 63, no. 2, pp. 340–351, 2014.

[81] J. Rizk, G.-L. Tan, J. B. Muldavin, and G. M. Rebeiz, "High-isolation w-band mems switches," *IEEE Microwave and Wireless Components Letters*, vol. 11, no. 1, pp. 10–12, 2001.

[82] W. Tian, P. Li, and L. Yuan, "Research and analysis of mems switches in different frequency bands," *Micromachines*, vol. 9, no. 4, p. 185, 2018.

[83] P. S. Kildal, E. Alfonso, A. Valero-Nogueira, and E. Rajo-Iglesias, "Local metamaterial-based waveguides in gaps between parallel metal plates," *IEEE Antennas and Wireless Propagation Letters*, vol. 8, pp. 84–87, 2009.

[84] E. Rajo-Iglesias and P.-S. Kildal, "Numerical studies of bandwidth of parallel-plate cut-off realised by a bed of nails, corrugations and mushroom-type electromagnetic bandgap for use in gap waveguides," *IET microwaves, antennas & propagation*, vol. 5, no. 3, pp. 282–289, 2011.

[85] P.-S. Kildal, A. Zaman, E. Rajo-Iglesias, E. Alfonso, and A. Valero-Nogueira, "Design and experimental verification of ridge gap waveguide in bed of nails for parallel-plate mode suppression," *IET Microwaves, Antennas Propagation*, vol. 5, no. 3, pp. 262–270, Feb. 2011.

[86] A. Vosoogh and P.-S. Kildal, "Corporate-fed planar 60-ghz slot array made of three unconnected metal layers using amc pin surface for the gap waveguide," *IEEE Antennas and Wireless Propagation Letters*, vol. 15, pp. 1935–1938, 2015.

[87] M. G. Silveirinha, C. A. Fernandes, and J. R. Costa, "Electromagnetic characterization of textured surfaces formed by metallic pins," *IEEE Transactions on Antennas and Propagation*, vol. 56, no. 2, pp. 405–415, 2008.

[88] S. Maci, G. Minatti, M. Casaletti, and M. Bosiljevac, "Metasurfing: Addressing waves on impenetrable metasurfaces," *IEEE Antennas and Wireless Propagation Letters*, vol. 10, pp. 1499–1502, 2011.

[89] N. Memeletzoglou, C. Sanchez-Cabello, F. Pizarro-Torres, and E. Rajo-Iglesias, "Analysis of periodic structures made of pins inside a parallel plate waveguide," *Symmetry*, vol. 11, no. 4, p. 582, 2019.

[90] J. Tayebpour, B. Ahmadi, M. Fallahzadeh, O. Shekoofa, and A. Torabi, "A waveguide switch based on contactless gap waveguide technology," *IEEE Microwave and Wireless Components Letters*, vol. 29, no. 12, pp. 771–774, 2019.

List of Journal Papers

[1] M. Bagheriasl, J. Sarrazin, and G. Valerio, "Reconfigurable waveguides using glide-symmetric bed of nails: Design of an all-metal switch at millimetre-wave band," *arXiv preprint arXiv:2007.08021*, 2020.

[2] M. Bagheriasl, O. Quevedo-Teruel, and G. Valerio, "Bloch analysis of artificial lines and surfaces exhibiting glide symmetry," *IEEE Transactions on Microwave Theory and Techniques*, vol. 67, no. 7, pp. 2618–2628, 2019.

[3] M. Bagheriasl and G. Valerio, "Bloch analysis of electromagnetic waves in twist-symmetric lines," *Symmetry*, vol. 11, no. 5, p. 620, 2019 (one of the 2021 best paper awards of the Symmetry journal).

List of Conference Papers

[1] M. Bagheriasl, J. Sarrazin, and G. Valerio, "Reconfigurable microwave components using glide-symmetric pin-loaded parallel plates," in *2020 14th European Conference on Antennas and Propagation (EuCAP)*, 2020, pp. 1–4.

[2] M. Bagheriasl and G. Valerio, "Multimodal analysis of periodic structures with glide symmetries," in *International Conference on Electromagnetics in Advanced Applications (ICEAA)*, Granada, Spain, Accepted.

[3] ——, "Analyse de bloch des métasurfaces à symétrie glissée," in *21èmes Journées Nationales Micro-Ondes*, Caen, France, Accepted.

[4] ——, "Bloch analysis of glide-symmetric structures using a multimode transmission matrix," in *2019 13th European Conference on Antennas and Propagation (EUCAP)*, Krakow, Poland, 1 Apr. 2019.

[5] M. Fall, M. Bagheriasl, O. Quevedo-Teruel, and G. Valerio, "Periodic structures with higher symmetries: Analysis and design," in *Journée annuelle de l'AREMIF 2018*, Paris, France, 19 Jun. 2018.